NOTICE

AVIS

The quality of this microform is heavily dependent upon the quality of the original thesis submitted for microfilming. Every effort has been made to ensure the highest quality of reproduction possible.

If pages are missing, contact the university which granted the degree.

Some pages may have indistinct print especially if the original pages were typed with a poor typewriter ribbon or if the university sent us an inferior photocopy.

Reproduction in full or in part of this microform is governed by the Canadian Copyright Act, R.S.C. 1970, c. C-30, and subsequent amendments.

La qualité de cette microforme dépend grandement de la qualité de la thèse soumise au microfilmage. Nous avons tout fait pour assurer une qualité supérieure de reproduction.

S'il manque des pages, veuillez communiquer avec l'université qui a conféré le grade.

La qualité d'impression de certaines pages peut laisser à désirer, surtout si les pages originales ont été dactylogra phiées à l'aide d'un ruban usé ou si l'université nous a fait parvenir une photocopie de qualité inférieure.

La reproduction, même partielle, de cette microforme est soumise à la Loi canadienne sur le droit d'auteur, SRC 1970, c. C-30, et ses amendements subséquents.

Canada

UNIVERSITY OF ALBERTA

An ECR Ion Source for TISOL at TRIUMF

BY

Paul Charles M^CNeely

A thesis

submitted to the Faculty of Graduate Studies and Research in partial fulfillment of the

requirements for the degree of Master of Science

in

Nuclear Physics

Department of Physics

Edmonton, Alberta

Spring, 1990

NOTICE

AVIS

The quality of this microform is heavily dependent upon the quality of the original thesis submitted for microfilming. Every effort has been made to ensure the highest quality of reproduction possible.

If pages are missing, contact the university which granted the degree.

Some pages may have indistinct print especially if the original pages were typed with a poor typewriter ribbon or if the university sent us an inferior photocopy.

Reproduction in full or in part of this microform is governed by the Canadian Copyright Act, R.S.C. 1970, c. C-30, and subsequent amendments.

La qualité de cette microforme dépend grandement de la qualité de la thèse soumise au microfilmage. Nous avons tout fait pour assurer une qualité supérieure de reproduction.

S'il manque des pages, veuillez communiquer avec l'université qui a conféré le grade.

La qualité d'impression de certaines pages peut laisser à désirer, surtout si les pages originales ont été dactylographiées à l'aide d'un ruban usé ou si l'université nous a fait parvenir une photocopie de qualité inférieure.

La reproduction, même partielle, de cette microforme est soumise à la Loi canadienne sur le droit d'auteur, SRC 1970, c. C-30, et ses amendements subséquents.

Canada

UNIVERSITY OF ALBERTA
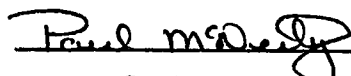
RELEASE FORM

NAME OF AUTHOR: Paul C. M^{C}Neely

TITLE OF THESIS: An ECR Ion Source for TISOL at TRIUMF

DEGREE: Master of Science

YEAR THIS DEGREE GRANTED: 1990

Permission is hereby granted to the UNIVERSITY OF ALBERTA LIBRARY to reproduce single copies of this thesis and to lend or sell such copies for private, scholarly or scientific research purposes only.

The author reserves other publication rights, and neither the thesis nor extensive extracts from it may be printed or otherwise reproduced without the author's written permission.

(Student's signature)

135 Anders Close

Red Deer, Alberta, Canada

T4R 1C2
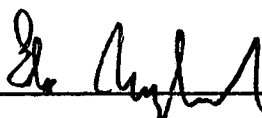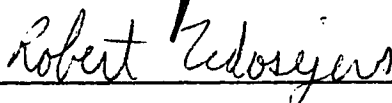
(Student's permanent address)

Date: Feb 14/90

THE UNIVERSITY OF ALBERTA

FACULTY OF GRADUATE STUDIES AND RESEARCH

The undersigned certify that they have read, and recommend to the Faculty of Graduate Studies and Research for acceptance, a thesis entitled *An ECR Ion Source for TISOL at TRIUMF* submitted by Paul Charles M^{C}Neely in partial fulfilment of the requirements for the degree of Master of Science in Experimental Nuclear Physics.

_____
Supervisor

_____

_____

_____
External Examiner

Date: __Feb 13/90__

This work is dedicated to my parents for all the love and support they have given me through the years.

Abstract

An Electron Cyclotron Resonance Ion Source was designed, built, and tested for the TISOL Facility at TRIUMF. The source is intended to be used for highly efficient production of singly charged radioactive isotopes when coupled to an on-line isotope production target. A brief description of the ion sources operating principles is included. This is intended to be used as an introduction to the topic of ECR Ion Sources for the non-specialist. Details on the design and all stages of the off-line testing are provided. The results for both the ionization efficiency and the emittance of stable argon and neon form the basis of the investigation. A variety of source parameters were investigated and the effects of these on source performance are provided. Finally, the first results after on-line installation are mentioned in an appendix.

Aknowledgement

As is standard with this kind of undertaking there were many people who worked behind the scenes as it were to yield the completed thesis and I would like to take this space to gratefully acknowledge the help and support. I would first of all like to begin by thanking Dr. Gerry Roy for his all his assistance towards getting everything done; the two trips were definite fringe benefits and way beyond the expected.

Dr. John D'Auria and the TISOL group also deserve a great deal of credit, for without them this project would not have existed. Their support during the off-line testing as well as during the on-line installation (where Merik Domsky and David Jones did the lions share of the work) was invaluable. Dr. Lothar Buchmann's advice about ECR's and ion sources in general was also much appreciated. Finally, I would like to thank Hart Springer for not only some interesting conversations but for doing such an incredible job of turning ideas into reality.

Dr. Paul Schmor and the ISIS group also contributed greatly. Providing not only testing facilities, equipment, and technical assistance but the RF Amplifier needed to operate the source. Mike McDonald deserves a great deal of credit for not only getting the project off on the right foot by designing the coil structure but also for answering my numerous questions on a broad spectrum of topics. I am deeply indebted to both Hans Wynngarden and Clint LaForge for the unstinting and invaluable technical assistance they provided during both the assembly of the off-line test bench and the testing that followed.

At the U of A, I would like to thank Jan Soukup for getting the inner RF cavity designed even though he had too much work for one person already. I would also like to thank Dr. Gordon Greeniaus for not only helping to tighten up my thesis grammatically but also in his incarnation as the *Mac Guru* for answering my numerous questions on the Mac's and most importantly for recovering my crashed thesis disk. The secretaries also deserve a big thank you for keeping track of where I was supposed to be and ensuring I had somewhere to stay where ever that was.

Finally, I would like to thank the other grad students, especially Phil Langill, Khalid Negm, Evan Hackett, and Mike Boyce for many interesting discussions on a wide variety of topics which helped keep me sane (sort of) through out this endeavor. I should not thank Kevin for the use of his computer games.

Table of Contents

Chapter Three The Source Design

Chapter Four The Off-Line Test Facility

Chapter Five Initial Operating Experience

Chapter Five Initial Operating Experience

Chapter Six Primary Source Testing

Chapter Seven Final Off-Line Test Results

Chapter Seven Final Off-Line Test Results

List of Tables

List of Figures

Chapter 1 Introduction

1.1 Chapter Introduction

This chapter will cover four topics which are intended to explain the purpose of the thesis as well as give some background information on the source's intended user, TISOL. The first section will be the statement of the purpose of the thesis. The second section will give a justification for conducting this type of research. The third section will detail the requirements for an on-line isotope separator. The final section will give a brief outline of the Test Ion Separator On Line (TISOL) facility at TRIUMF.

1.2 Purpose of the Thesis

The goal of this thesis was as a part of a joint University of Alberta, TRIUMF, and Simon Fraser University collaboration to design and construct an Electron Cyclotron Resonance Ion Source (ECRIS) for the TISOL facility at TRIUMF. After the source was constructed it was to be rigorously tested in an off-line test bench area. The purpose of this testing was to determine the source's suitability for on-line operation. The three major goals of this testing were: to determine the ionization efficiency of the source, to determine the effects of various support gases on the source's operation so as to determine which gas should be used in an on-line mode, and finally to find out what the effect is of various source parameters on the operation of the source.

1.3 Justification for Studying Radioactive Nuclides

This section will list the main reasons for studying radioactive nuclides in general terms and concentrate on one of the reasons which has recently generated much excitement. There are six major reasons for the study of radioactive nuclei (TIS 85, Cra 89).

The first is to re-examine basic nuclear properties such as: nuclear structure, mass or shape. A radioactive nuclei is a strong test of the shell model and by improving the understanding of the unusual then the theory can be further refined. As a side effect of this there is the possibility to improve the reliability of the semi-empirical atomic mass formula which is used to determine the mass of most of the radioactive nuclei known. Direct measurements of the masses of radioactive nuclei are also of interest since there are possible discrepancies between the experimentally determined values and the absolute nuclear mass due to the cumulative errors in the decay energy measurements used to determine the initial mass of the radioactive nuclide.

The second reason to study radioactive nuclei is to apply conventional nuclear spectroscopic techniques to areas of interest. One such area is the nuclear state where there are only a few valence nuclei outside a closed shell. It is especially interesting to examine magic number nuclei (cases where either the number of protons or total number of neutrons corresponds to one of the magic numbers 2, 8, 20, 28, 50, 82, or 126 (Fra 74)). The stable magic nuclei have all been extensively studied but apart from, ^{56}Ni, of the remaining magic number nuclei lie far from stability. For example ^{132}Sn. ^{132}Sn lies approximately 10 nucleons from the valley of stability. Another area of interest is the investigation of nuclear shape changes through studies of extended chains of isotopes.

A third reason is to study exotic decays of nuclei. There are two possible exotic decay conditions. The first is when the parent nucleus is proton rich. Involved in this are the standard β^+-decay, and β-delayed nucleon emission to name a few possibilities. The other possibility which seems to offer some even more novel possible decays occurs when the parent nucleus is neutron rich. In this case there are three possible β-delayed reactions: neutron emission, tritium emission, and fission. There is also the possibility of observing ground state double neutron emission. In any case these reactions can yield

valuable information on nuclear energy levels, structure, and even practical matters such as nuclear reactor heating dynamics.

The investigation of fundamental physics is the fourth reason to study radioactive nuclei. Parity violation has already been investigated with stable nuclei (Ade 84) but further information concerning relevant matrix elements could be gained by investigating, for example, certain first forbidden β-decays. It would also be possible to test predictions of quark models in nuclei. These tests would not be easy to carry out since nuclei with specific characteristics are required in general to do a particular experiment.

The fifth reason is to take the produced radioactive nuclei and to accelerate them to higher energy. These accelerated radioactive beams can then be used in the same way that protons are used now for standard experiments. The acceleration of stable ions is currently an exciting field of study so it takes little imagination to see that extending the field to radioactive ions should yield new and important information. There are currently proposals at both TRIUMF and the ISOLDE facility in CERN to build such a post-accelerator.

The final reason was the primary motivation for the project. In nuclear astrophysics reactions involving radioactive light nuclei are of primary importance to the various cycles or processes which occur during stellar evolution. A list of important reactions, the processes which they represent and the life time of the initial nucleus is presented in table 1-1(Buc 86). It is important to note that the longest life time is slightly more than eleven minutes requiring the use of an accelerated radioactive beam to fully explore these reactions. A facility to perform the first reaction has been set up in Louvain-la-Neuve, Belgium(Del 88) and has had its first run in the summer of 1989.

Table 1-1: A list of reactions, the life time of the parent nucleus, and the process they are a part of that are of primary interest to nuclear astrophysics.

Reaction	$\tau_{1/2}$ (s)	Process
$^{13}N(p,\gamma)^{14}O$	598	hot CNO cycle
$^{15}O(\alpha,\gamma)^{19}Ne$	122	rp process
$^{18}F(p,\alpha)^{15}O$	6582	hot CNO
$^{18}F(p,\gamma)^{19}Ne$	6582	hot CNO
$^{19}Ne(p,\gamma)^{20}Na$	17.2	hot CNO/rp process
$^{21}Na(p,\gamma)^{22}Mg$	22.5	NeNaMgAl cycles / rp process

The β-decay strength function for neutron rich decays is also of considerable interest to astrophysics not only as it applies to nucleo-synthesis but also for such topics as the age of the galaxy and helping to explain gravitational collapse.

These are only applications of radioactive nuclei in nuclear physics; for the uses of radioactive nuclei in other fields see ref. (Tis 85).

1.4 General Requirements of an On-Line Isotope Separator

The operation of an ISOL facility puts special demands on the ion source which are not required for off-line use or for injection into a cyclotron. A source which is to operate on-line must fulfill most of the following requirements.

Of primary importance is that the source have a high ionization efficiency since the amount of radioactive atoms produced is not large. The source must produce a good quality beam in terms of both its emittance and brightness. This allows for easy, efficient transport through the beam line and any analysing magnets. The source must be reliable and its maintenance characteristic should match both those of the cyclotron providing the primary beam for the target and the post-accelerator facility (if any). The source should also be durable, in other words, there must be few parts which are subject to frequent

replacement . The source should be easily portable so that it can be exchanged with another source for specialized runs. Finally, the source must be radiation resistant since it will be exposed to extremely high radiation fields. Two additional requirements that are not necessary but would be desirable are: capablility of ionizing many different species and simplicity operation so as not to further burden the control of the isotope separator / post-accelerator.

An ECRIS fulfills these requirements admirably. The emittance of an ECRIS is reasonably good and can be easily matched to the acceptance of an RFQ linac (the most commonly considered candidate for a post-accelerator). The source is both reliable and has a low maintenance requirement due to the fact that there are no parts in the source that can wear out. The source can be designed to be compact and easily mated to a variety of standard flanges for easy exchange. The source can be constructed with high radiation resistance samarium cobalt permanent magnet material since the hexapole is the only element which can be critically damaged by high radiation fields. The source is also able to ionize a wide range of species. The species produced by the LBL-ECR are listed in ref. (Lyn 87). They cover a good part of the periodic table encompassing both solid and gaseous materials. To put it crudely: if a species can be introduced as a gas into an ECRIS it can be ionized. The ECRIS is simple to operate as it has few operating parameters which can be varied during a run and all of these can be done remotely.

To be totally honest, the surface ion source and the plasma ion sources also fulfill these requirements. These two sources are the ones most commonly used for ISOL applications and perform quite well. The main advantage of an ECRIS is its efficiency. Shown in table 1-2 is a listing of the ionization efficiencies of an ECRIS (Bec 86) compared to other source types (Buc 86). It should be noted that the efficiencies quoted for the ECRIS are *off*-line only. Recent developments have begun to call the results

obtained by the Karlsruhe group (Bec 85,Bec 86) into question. The Louvain-la -Neuve

ECRIS recorded an 0.5% efficiency for the ionization of ^{13}N (Van 89) and there has been

concern that the efficiencies reported for nitrogen and oxygen might include errors from

vacuum leaks (Hof 89).

Table 1-2: A comparison between the ionization efficiencies of an off-line ECRIS and those achieved on-line by other source types.

Element	Ionization Efficiency (%)	
	On-line	ECRIS
Nitrogen	0.01	26
Oxygen	?	53
Neon	0.7	34
Sodium	50[1]	?
Chlorine	1	?
Argon	5	?
Potassium	100[1]	?
Xenon	?	58

[1]surface ionization source.

Only careful measurement of the ionization efficiency of an ECRIS operating in an

on-line mode can fully answer the questions raised. One possible reason for differences

between off-line and on-line results is thought to be that the operation with radioactive

atoms is different in terms of ion confinement than for stable ions. An example to

illustrate this is *wall capture*. Should a stable ion become attached to the wall for a time

and later be released, the effect of the overall efficiency would be slight since the current

lost while it was attached would be made up later. For a radioactive ion it is a different

story. If the capture time is sufficiently long the ion may decay and hence there will be a

lower observed efficiency for the radioactive ion compared to the stable ion. Even with

this and other possible unforeseen problems it still appears that an ECRIS offers an

advantage in ionization efficiency (as an example for nitrogen 0.5% from LLN compared to 0.01%).

1.5 The TISOL Facility

The TISOL facility is the intended end user of the source being constructed. As such it seems proper to devote some space to a brief description of the facility itself. In 1985 a proposal was submitted to build the T-ISOL (TRIUMF ISOL) facility which was to be a facility for the production and acceleration of radioactive ion beams. This facility failed to receive funding. In 1986, TRIUMF independently provided funding for a small prototype on-line isotope production facility (TISOL) which was installed on beamline 4A (see fig. 1-1) in the spring 1987 shutdown.
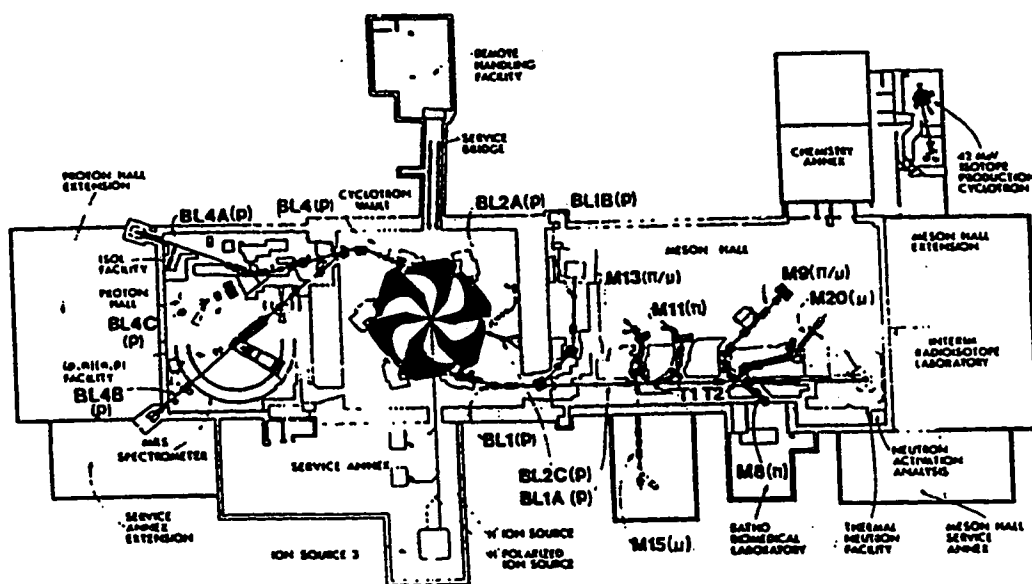
Fig. 1-1 The above diagram of the main accelerator building at TRIUMF shows the location of the TISOL Facility in the proton hall side on beamline 4A.

The TISOL facility has four main purposes. The first is to develop the expertise needed to construct and operate a full scale isotope separation and acceleration (ISAC) facility. Much of this experience can only be gained by hands-on solutions to everyday operational problems. The second purpose is to explore target chemistries to determine the best target for the production of a specific radioisotope. This is another area in which expertise can only be gained by experience. The problems associated with the target are quite complex. There is the radiation both from the scattered proton beam and the production target itself. Also for the radioisotopes to be released from the target it must be heated to >1500° C which means that even the choice of construction materials is not a trivial matter. The target material required, which depends on the isotope desired, is another consideration, as are the tricks required to obtain maximum performance from the target. Finally, there are the questions of the transport of the radioactive ions through the system, the problems of potentially hazardous radioactive waste disposal or leakage, and the handling and storage of highly radioactive materials when the target must be changed.

The third area of research involves the use of other ion sources for the production of radioisotopes. The initial ion source was a surface source based on the ISOLDE source. Two other ion source types have been explored to date. The first was a plasma ion source originally constructed by a collaboration from McGill / ISOCELE which has been modified for simpler construction and use. The second ion source is the topic of this thesis.

The final purpose is to make engineering studies of the support services of an ISOL to ensure that the proposed ISAC facility is indeed feasible. Part of this goal was the development of a micro-computer based control system by R. Keital which could be used in other locations around TRIUMF as well as at TISOL. Other considerations examined were: the amount of radiation produced by different targets, the amount of shielding

required to protect experiments from the high radiation fluxes, the most efficient pumping system to use, etc.

A schematic diagram of TISOL is shown in fig. 1-2. The facility consists of a target ion source (TIS 85) from which the ions are extracted at 20 kV. This beam is then focused by a set of focussing quadrupole magnets just before the entrance to the 90° vertical analysing magnet. This is followed by an electrostatic beamline which bends the ion beam to parallel to the surface of the shielding blocks. This electrostatic beamline consists of a set of electrostatic focussing quadrupoles followed by a 90° electrostatic bender and another set of quadrupoles. Finally there is the collection station which can be viewed by β and γ detectors. A tape drive collection system is expected to be installed soon to allow for high resolution low background counting. There are four faraday cups to assist the system operator in optimizing beam transport.
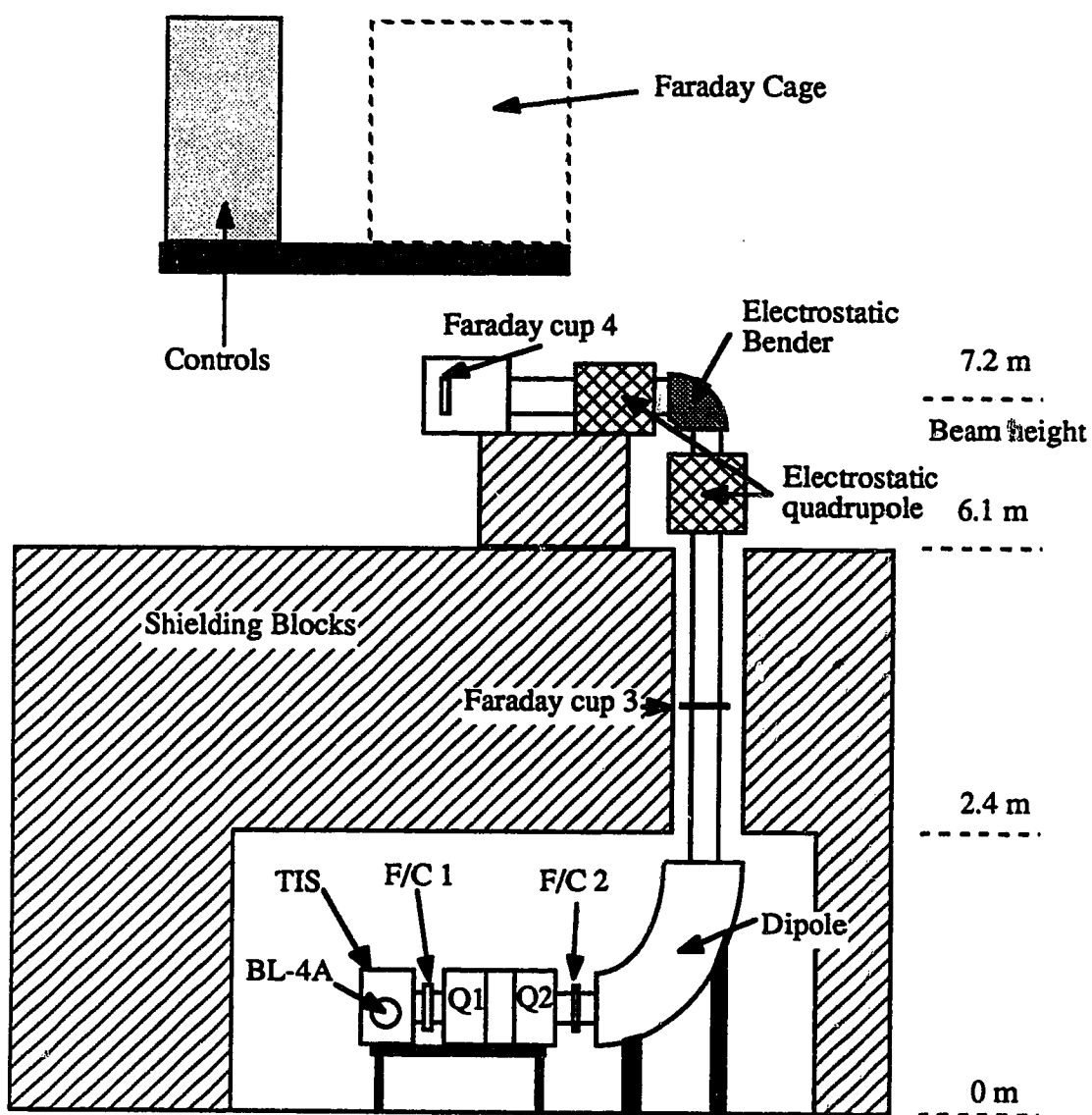
Fig. 1-2 The above schematic shows the primary components of the TISOL facility.

Chapter 2 About ECR Ion Sources

2.1 Introduction

The Electron Cyclotron Resonance Ion Source (ECRIS) was developed in 1973 by Dr. R Geller at Grenoble-CEN, France as an outgrowth of his work in fusion research. Since that time the number of operational sources has increased dramaticaly, until they now replace most Penning Ion Gauge (PIG) sources for the injection of highly charged ions into cyclotrons. They are also used to study atomic structure. Even more recently, an ECRIS was used in the CERN heavy-ion collision experiments into the nature of the quark-gluon plasma. It provided the initial beam current of O^{6+} ions which were used in the experiment (Gel 87, Has 89). Table 2-1 provides a listing of some of the major sources in use throughout the world(Lyn 87).

This chapter will explain how an ECR ion source operates. At this time there is not much theoretical input into many of the operating principles; most of the concepts which are used to construct and operate an ECRIS are *rules of thumb* developed by trial and error. In fact, this is one of the difficulties in breaking into the field since few of these rules are written anywhere as they are considered common knowledge by the community. This chapter will be divided into three sections. In the first a brief description of how an ECRIS works will be given. The second will develop more fully the various concepts introduced in the first. The final section will be devoted to some of the scaling laws that have been determined for ECR ion sources.

Table 2-1: A listing of some of the operating ECR sources and their purpose from (Lyn 87).

Country Laboratory Source	Frequency (GHz)	Comments	Application
France Grenoble-CEN Minimafios	10	Now at SARA,KVI,GANIL	Test, AP, cyc

11

Table 2-1: cont.

Country Laboratory Source	Frequency (GHz)	Comments	Application
Minimafios	10	CERN-SPS	synchrotron
Minimafios-16GHz	16	pulsed source	test
Caprice	10	iron yoke, very compact	test
Minimafios-18GHz	18	highest frequency ECR	test, synchrotron
Germany			
KFZ-Karlshruhe			
LISKA	7.5	Lithium ECR	cyc
High efficiency ECR	6.4	Isotope Separation	test
KFA-Julich			
Pre-ISIS II	5	two stage	test & cyc
ISIS	14.3,14.3	large s.c., high freq.	cyc
Belgium			
Louvain-la Neuve			
OCTUPUS	14.3,8.5	Iron yoke, open octupole	cyc & AP
high efficiency ECR	6.4	Isotope Separation and radioactive beam experiment	cyc& test
USA			
Lawrence Berkeley Lab			
LBL-ECR	9.2,6.4	Open SmCo hexapole	cyc & AP
NSCL-MSU			
RT-ECR	6.4,6.4	Iron yoke 1st stage, hexapole	cyc
Argonne National Lab			
PIIECR	10	On high voltage platform	linac
Switzerland			
CERN-ISOLDE			
high efficiency ECR	6.4	Isotope production	test
Canada			
TRIUMF			
I4	28	polarized H- source, s.c.	cyc
high efficiency ECR	10	on-line isotope production	test

cyc cyclotron, AP atomic physics, s.c. super conducting

2.2 An overview of ECR source operation

The various elements of an ECRIS can be seen in fig. 2-1.

RF input

Gas
Input

Plasma

Extraction
System
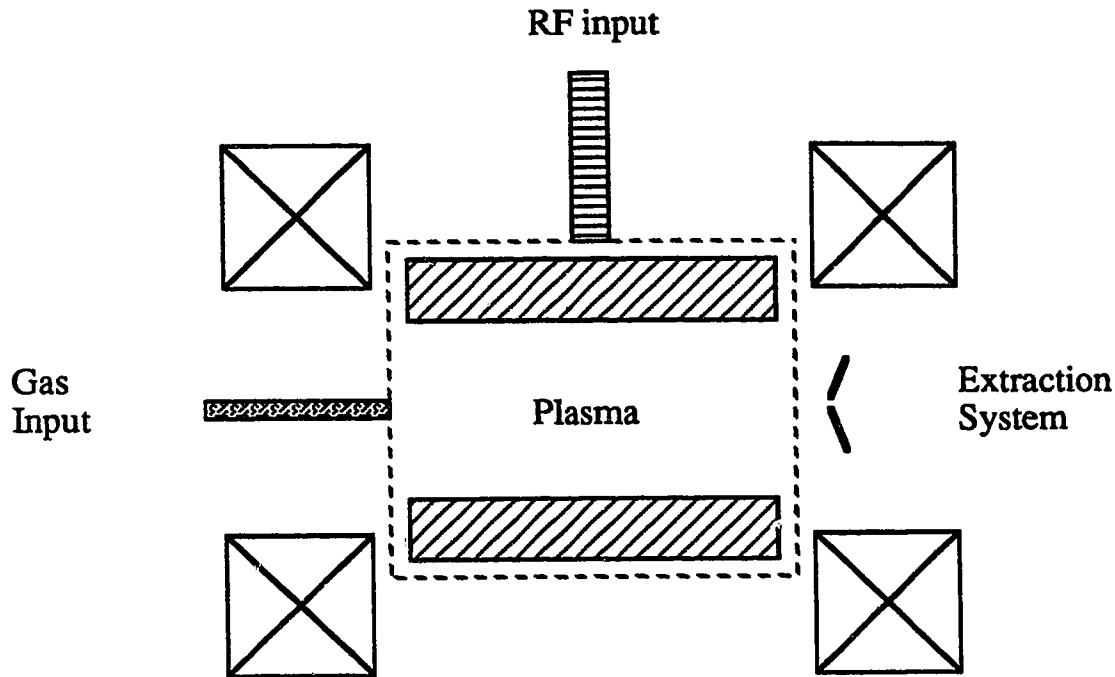
Fig. 2-1: A schematic diagram showing the principle elements of an ECR ion source.

The key to the operation of an ECRIS is its magnetic bottle. The bottle is made up by the superposition of an axial field produced by an set of solenoid coils and a radial field produced by a permanent magnet hexapole. The energy to create and maintain the plasma comes from the microwave power injected into the source. These microwaves will couple to the electrons along a cigar shaped boundary of what is known as the ECR region and thus transfer energy to the electrons. The electrons then produce the plasma by impact ionization of the neutral gases in the plasma volume. This reaction is maintained by electron confinement due to the magnetic field configuration. The RF cavity (the dashed line in fig. 2-1) contains the microwaves and allows for the

establishment of the standing wave required for the energy transfer to take place. The gas input system provides the mix of gases to be ionized. The final system is the extraction system which removes the ions from the plasma and forms them into a beam.

2.3 Detailed Description of Source Concepts

2.3.1 Introduction

This section will examine in much greater detail the various elements of the source mentioned above. For each element the goal will be to explain, when possible, both the theoretical and experimental aspects which are used by source designers and operators as well as any rules of thumb. This section is essentially a summary of articles in the literature. It should also be remembered that the amount of theoretical work done on the ECR plasma is quite limited as the subject is very complex.

2.3.2 The Magnetic Bottle

The magnetic bottle is the heart of any ECRIS. With almost no exceptions all ECRIS use the so called minimum field geometry. In this structure the ECR condition (see below) is fulfilled in the valley between the peaks of the magnetic field formed by the two solenoid coils (see fig. 3-10). This form of magnetic structure, however, does not stably confine the plasma since the field decreases in strength in the radial direction (Jon 84). To create the condition for stable confinement, a field which increases radially, a hexapole is added around the plasma region. It is not necessary to use a hexapole magnet, for example the OCTOPUS source at Louvain la Neuve uses an octupole, but probably due to cost considerations most sources are constructed with only a hexapole. Additionally the hexapole provides radial confinement since its field increases with distance from the axis because in the central region of the solenoid the radial component of it's magnetic field is quite small (<300 G). There is clear evidence that it is necessary

to have a hexapole for high charge state production. However, if the goal is only the production of singly charged ions, as in high efficiency machines, a hexapole might not be necessary since many of the early fusion machines produced intense beams of singly charged ions with only the solenoid field.

The second major duty of the solenoid coils is to provide the magnetic field required for an electron cyclotron resonance condition to form. The magnetic field required for a given microwave frequency is given by the following formula:

$$\omega_{ECR} = \frac{eB_{ECR}}{m_e c} \qquad (2\text{-}1)$$

where ω_{ECR} is the microwave frequency, e is the electron charge, B_{ECR} is the magnetic field required for resonance, m_e is the electron mass.

Although the superposition, of the solenoid and hexapole fields, is difficult to conceptualize, the shape of the plasma has been calculated and was found to agree with the observed plasma size (Jon 84).

2.3.3 The Microwave Cavity

The microwave cavity is what contains the energy necessary to drive the plasma. In this source, as in most others, instead of exciting a single mode for the microwaves in the region that contains the plasma the area is made over-large so that all possible modes are excited thus forming a multi-mode cavity. This ensures that along the ECR condition boundary there will always be an electric field component which is perpendicular to the magnetic field lines (Bec 85). This means that each time an electron passes through the ECR region it will be accelerated in the direction of the electric field although it is possible that the electron will have its velocity decreased rather than increased depending on the relative phase of the electric field.

One of the still outstanding and important questions about ECR plasmas is how the electron energy relates to the incident microwave power. Some attempts have been made

to explain how the process works (Jon 84, Lib 89); however, none were totally successful and the problem still remains. One fact known for certain is that the electron energy is not modeled by a Maxwell-Boltzmann distribution, thus making theoretical calculations much more difficult.

2.3.4 Gas Input System

This topic is very extensive in scope but only a few of the more important points will be mentioned. The gas input into the source determines more than the species extracted since for each gas the source operates differently. As an example, the RF power needed to produce a set ionic current varies from gas to gas due to a variety of parameters: molecular bonding strength, ionization energy, number of electrons per atom, etc. These effects are even more noticeable when gases are mixed either on purpose or accidentally due to a vacuum leak.

The effects of gas mixing were studied (Mac 86) in great detail and an attempts were made to explain the results obtained (Gel 87, Ant 89). The main result can be summed up in a simple rule of thumb: to improve either the maximum charge state obtained from an ECRIS or the maximum current obtained for a given charge state add a mixing gas which is ~1/3 the mass of the gas of interest. Another effect that has been noticed (Lyn 89, Gel 89a) at various laboratories is the performance increase obtained by running with SiO_2 in the source. A possible explanation for the effect of wall coatings can be found in (Gel 87).

When dealing with an on-line isotope production facility an important point to remember is that there will be insufficient radioactive atoms produced to sustain a plasma. Therefore, a carrier or support gas (the terms will be used interchangeably) must be added to form the plasma. Because of this, one of the goals of this project was to find out what effect the type of support gas used has on ionization efficiency. The results for

this question can be found in chapter 6 and 7.

However, just as critical as the type of support gas is the amount of it. ECRIS are very sensitive to pressure. Too much gas and the charge exchange process (described in section 2.3.5.3) will destroy the plasma. Too little gas and a plasma will not form. Between these two extremes are regions which favor a specific charge state or even a specific ion species over another, therefore, a fine control over the gas flow is necessary.

2.3.5 The Plasma

The ECR plasma is a tremendously important but far from understood topic. The plasma consists of three parts: the electrons, the ions, and the neutral gas. Before examining each of these constituents in detail a comment should be made about an important gross indicator of the plasma value. For any given source there is a specific figure of merit given by:

$$n_e \tau_i. \tag{2-2}$$

Here n_e is the electron density which is given by the cut-off frequency of the microwaves incident on the plasma. The other term, τ_i, is the time under which the ions are exposed to the ionizing electrons or the ion confinement time. Typical values of n_e and τ_i are 2.5 x 10^{11} cm^{-3} and 10^{-3}-10^{-2} s respectively, giving a $n_e \tau_i$ value that is on average ~10^9 cm^{-3}s (Jon 84).

Of what value is this? The charge state distribution of the plasma is directly related to the value of $n_e \tau_i$ (see fig. 2-2). As can be seen, for higher values of $n_e \tau_i$ the maximum charge state possible to produce increases. The next sections will examine in greater detail the properties of the plasma constituents.

Figure removed from microfilm copy due to copywrite restrictions.

Fig. 2-2 A graph of the the number of ions in a particular charge state versus the $n_e\tau_i$ value (Jon).

2.3.5.1 The Electrons

One of the advantages an ECRIS has over other ion sources is that the electrons execute multiple passes through the plasma enhancing the probability of ionizing the neutral gas component of the plasma. Since the motion of the electrons is so important, a large amount of theoretical effort has gone into predicting it. The electron motion can be handled in a non-numerical framework as well(Jon 84). This means that the motion of a charged particle in a magnetic mirror can be decomposed into three parts (see fig. 2-3).
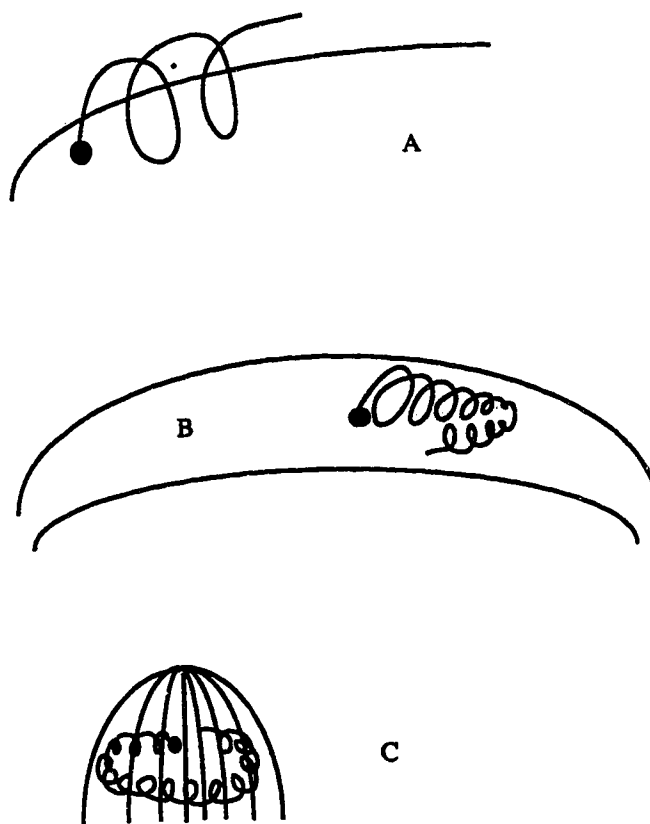
Fig. 2-3 The decomposed motion of a charged particle in a magnetic bottle.

The first of these (A) is the electron cyclotron rotation around a magnetic field line. The second motion (B) is the oscillation of the particle along a field line caused by reflection at the field maxima. The final motion (C) is azimuthal drift between field lines caused by the radial field gradient. Several computer codes have been developed recently (Jon 84, Ant 87, Par 86) to simulate the electron trajectory in an attempt to predict the charge state distribution observed in ECRIS. An example of the complexity of even the two dimensional motion is shown in fig. 2-4, which shows the result of one of these programs (Par 86) for the ATLAS PIIECR at the Argonne National Laboratory.

Figure removed from microfilm copy due to copywrite restrictions.

Fig. 2-4 A plot of the electron motion in the PIIECR at Argonne Laboratory from (Par 86).

To ensure that the electrons undergo multiple passes through the plasma good confinement is necessary. Escape is possible if the particle undergoes a sufficiently large angle scattering process and enters the loss cone. The period associated with this process scales with energy so for electrons the collision time is given by:

$$\tau_{coll} \sim E_e^{-1.5}. \qquad (2\text{-}3)$$

Each of the decomposed motions of the electrons has a period associated with it. The cyclotron rotation has a period which scales with the magnetic field strength.

$$\tau_{cyc} \sim B^{-1} \qquad (2\text{-}4)$$

The oscillatory motion between field maxima has a period which scales with the electron velocity.

$$\tau_{osc} \sim V_e^{-1} \qquad (2\text{-}5)$$

The azimuthal drift has a period which scales with the electron energy.

$$\tau_{azm} \sim E_e^{-1} \qquad (2\text{-}6)$$

Under normal values for these quantities the periods are related as shown:

$$\tau_{cyc} \ll \tau_{osc} \ll \tau_{azm} \qquad (2\text{-}7)$$

For the electrons to be confined, the confinement time τ_{conf} should equal the collision time and be greater than any of the other motion periods. As it happens for high energy electrons:

$$\tau_{cyc} < \tau_{osc} < \tau_{azm} < \tau_{coll} \cong \tau_{conf}, \qquad (2\text{-}8)$$

so the hot electrons are confined.

Although it would seem imperative to restrict the number of high energy electrons to improve the electron confinement times should one wish to produce high charge state ions (which is the goal of most ECRIS in operation) it is precisely those high energy electrons that are necessary.

This introduces the question of heating of the electrons by the microwaves. Unfortunately, this is another of the poorly understood parts of an ECR plasma. Two facts about the electron energy are known, however. The first is that the electrons can range in energy from 1 eV to about 10 keV. Unfortunately, the exact distribution is not known although it is known to be non-Maxwellian (Jon 84). The second fact is that an equilibrium condition is established which balances the energy lost due to direct RF heating of the plasma container and the hot electrons escaping with the energy supplied by the incident microwaves.

2.3.5.2 The Positive Ions

The part of the plasma of greatest interest to the physicist consists of the positive ions since their production is the purpose of the source. The ions are not confined by the magnetic bottle since in their case:

$$\tau_{coll} \sim \tau_{cyc} \ll \tau_{osc} \ll \tau_{azm} \qquad (2\text{-}9)$$

It should be noted that although there is no reflection and the azimuthal drift in the radial

field is very slow, the ions do follow and precess around field lines. This fact will be important when the extraction of ions from the plasma is considered.

It is generally accepted that the ions undergo stepwise ionization with a rate of ionization given by:

$$v^{i \to i+1}(E) = \sigma_{i \to i+1}(E)\, v(E)\, n(E) \qquad (2\text{-}10)$$

where: σ is the ionization cross section,
v is the electron velocity, and
n is the electron density.

The energy distribution of the ions is unknown although for simplicity the Maxwell-Boltzmann distribution is often assumed. The maximum ion energy is assumed to be <5eV. The life cycle of the ions produced is shown in fig. 2-5. It is important to note that only a small number of the ions are extracted at one time. Most are neutralized by collisions with the wall of the plasma volume.

Although the ions are not confined magnetically they are confined by a potential well created by the electrons (Pet 87, Pet 89). The plasma is overall electrically neutral as there is the same amount of both positive and negative charge. However, the electrons fall into two different energy categories: cold electrons, and hot electrons. The regimes are spatially separated since the the hot electrons populate the inner regions of the plasma while the cold electrons since they are poorly confined are found in the outer plasma regions. The cold electrons define a potential which decreases outward from the center of the source to the mirror field peak according to the following formula:

$$n_m = n_o \exp\left[\left(\phi_m - \phi_o\right)/T_{ec}\right], \qquad (2\text{-}11)$$

where: n is the electron density,
ϕ is the potential,
T_{ec} is the electron temperature, and
m, o refer to the mirror and central value respectively.

The hot electrons modify this by causing a potential dip in the central region. Because these electrons have long life times, they force electrostatic confinement of the ions since the only way to balance their contribution to the over all charge is by ion-electron neutralization.
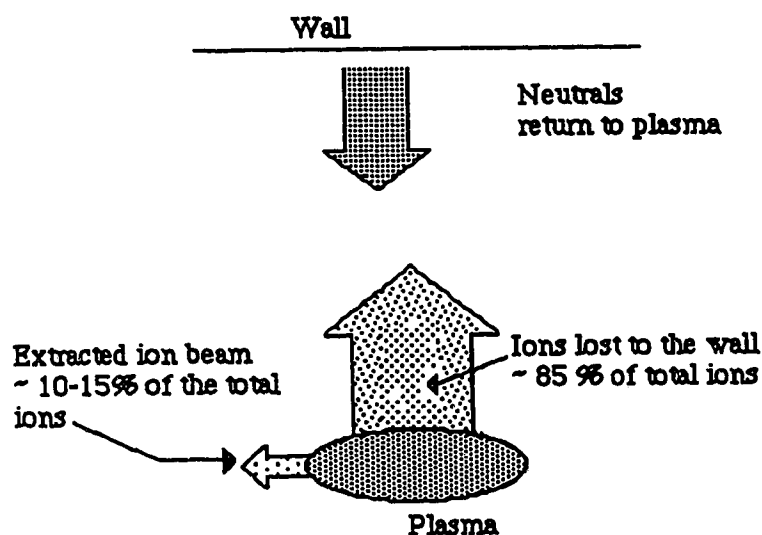
Fig. 2-5 In the diagram above is shown the life cycle of positive ions produced by the plasma.

2.3.5.3 The Neutrals

The neutrals compose the final elements of the plasma. Their sole importance other than as a source of atoms to be ionized is that they can bring about charge exchange by collision with the positive ions. For high efficiency ECRIS, since the extraction of singly charged ions is the goal, this is not so much of a problem. The highest ionization efficiency is obtained if all ions of a particular species are in the same charge state which in most cases for a high efficiency source is the singly charged state. Where the goal is a high charge state a great deal of effort goes into minimizing the effects of charge exchange. The exchange cross section is given by:

$$\sigma_{\text{EXCH } i \to i-1} = 1.5 \times 10^{-12} \, I^{1.17276} P_{0 \to 1}^{} \, cm^2 \qquad (2\text{-}12)$$

where: I is the ionization state, and

P is the ionization potential for the +1 ion.

On average it has been found that the charge exchange cross section is three to four times as large as the ionization cross section; it is fortunate, however, that the rate of charge exchange is given by:

$$v^{i \to i-1} \alpha \, \sigma_{\text{EXCH}}^{i \to i-1} v_{ion}(E) \qquad (2\text{-}13)$$

where: $v_{ion}(E)$ is the ion velocity.

It has already been noted that $v_{ion}(E) \ll V_e(E)$ so the rate of ionization is much higher than the charge exchange rate.

2.3.6 The Extraction System

The extraction system is the single most critical element in the source as it is the interface between the source and the real world. It is relatively unimportant how well a source ionizes compared to how well the extraction system works since any measurements done on the extracted beam, say for example the ionization efficiency, are really a measure of the product of the source efficiency and the efficiency of the extraction system. Therefore, a careful design of the extraction system is essential. For ECRIS there are three factors which affect the extraction system. These are: the bias voltage and extraction electrode/plasma electrode gap, the extraction geometry, and the axial magnetic field.

Together the bias voltage and gap width define the current that can be extracted from any source. For any source there are two possible currents which can be drawn from it. The first type of current is the plasma-limited current (Kra 86):

$$J_{PL} \sim n_i \left[\frac{Z}{A} \right]^{1/2} T_i \qquad (2\text{-}14)$$

where: n_i is the ion density, and

T_i is the ion temperature.

This is the ultimate current which can be drawn from the source and it is dependent only on internal source parameters.

The second type of current is the space-charge limited current (Kra 86):

$$J_{SPC} \sim \left[\frac{Z}{A}\right]^{1/2} \frac{1}{d^2} V^{3/2} \tag{2-15}$$

where: d is the electrode separation, and
V is the extraction voltage.

This relationship is known as the Child-Langmuir law. Notice that both the electrode separation and the extraction voltage appear. It is obvious that with respect to ion current versus extraction voltage (if the gap is kept fixed) there are two regions (see fig. 2-6). The first is where the current increases with voltage or where $J_{SPC} < J_{PL}$ and the second is where there is no effect due to increasing the extraction voltage, $J_{SPC} > J_{PL}$. The best condition to run a source is obviously in the plasma-limited current regime as this means the extraction current is the maximum possible.

The extraction geometry affects mainly the initial beam formation. The topics cover a wide spectrum of areas. The first consideration is the use of a Pierce extraction geometry. This means that both the plasma and the puller electrodes (for these definitions see sections 3.4 and 3.6) should have their faces at an angle of 67.5° to the beam axis. It has been found that using a non-Pierce geometry produces beams that are worse then those obtained simply using two flat plates (Rav 88).

The second consideration is whether or not to include a negatively biased electrode. This can either mean an additional electrode or having the puller itself biased. The purpose of this is to suppress secondary electron emission. Another, similar method is to make the puller electrode out of a high work function material such as molybdenum (Sch

89).
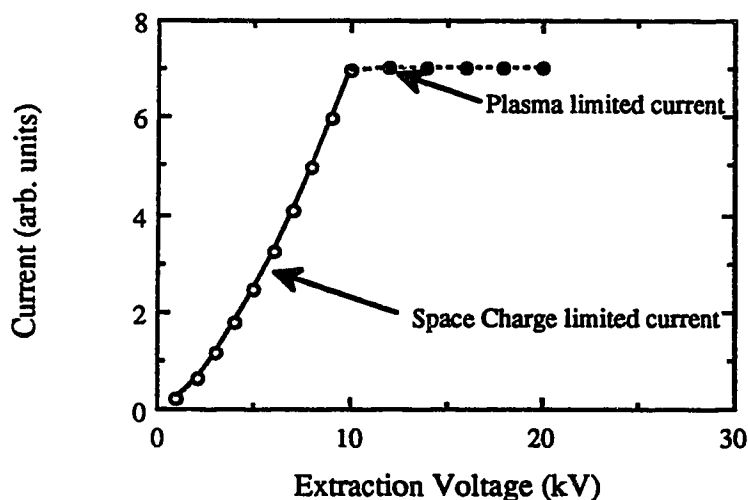
Fig 2-6 The above graph shows the two extraction current regimes.

The third consideration is the diameter of the apertures in the two electrodes. The diameter of the aperture in the plasma electrode determines the maximum current that can be extracted in the the plasma current region since the current drawn from the source , I, increases with the area of the hole:

$$I = \pi \left(\frac{d}{2}\right)^2 J \qquad (2\text{-}16)$$

where: d is the aperture diameter, and J is the measured current density.

The size of the aperture in the puller electrode determines the initial beam focusing. If it is too large then the electric field lines will extend through it causing a highly divergent beam. If, on the other hand, it is too small the beam will strike the electrode thus limiting the current. Another problem is the emission of secondary electrons which could neutralize ions in the beam. The exact ratio of the puller electrode hole diameter to the plasma electrode diameter, R, varies from source to source but convention indicates

that the ratio should be something like: $1 < R < 5$ with an average around 2 or 3. The exact number depends on the size of the plasma electrode aperture.

The final consideration is the inclusion of an electrostatic focusing element. The Einzel lens gives the beam an initial *squeeze* to ensure maximum transmission and can later be adjusted to maximize the transmission of a specific ion species. This is possible because the effect of the lens depends on both the mass and the charge of the affected species. The changes undergone by the source's extraction system will be detailed in later chapters.

The extraction of the ion beam through the decreasing gradient of the axial magnetic field is the final extraction effect. The plasma electrode should be placed on the peak of the mirror field to ensure a relatively uniform magnetic field during the initial extraction.

The major effect of extraction through a large, changing, axial magnetic field gradient is beam emittance increase. The emittance of the beam is composed of two parts. The first is the plasma emittance and the second is the emittance due to traveling through the fringe field. The plasma emittance is due to the temperature or velocity spread of the ions (Cla 87). Since all ions will have some velocity components perpendicular to the extraction axis the beam will tend to spread. The emittance for this effect is proportional to:

$$\varepsilon_{Plasma} \alpha \ \sqrt{T_{ion}} \qquad (2\text{-}17)$$

where T_{ion} is the ion temperature. This effect is quite small since $T_{ion} < 5$ eV on average.

Unfortunately the fringe field effects are not small. Keep in mind that although the ions are not confined by the magnetic mirror they do follow field lines. This situation, after the extraction region, leads to a problem. The magnetic field lines are curving outward at this point as they are looping back towards the coils. The ion depending on its initial off-axis position, gets a reinforcing kick in the outward direction causing an

enhancement in the any initial divergence of the beam. The effect is given by (Kra 86):

$$\varepsilon_{Fringe} \propto \frac{Br^2}{(B\rho)} \qquad (2\text{-}18)$$

where: r is the plasma electrode aperture radius,
B is the magnetic field at extraction, and
Bρ is the ion rigidity.

Unfortunately, there is nothing that can be done to remove this effect so it remains a fact which the outside focusing elements must deal with.

2.4 Scaling Laws

It is of primary importance to a designer to have some sort of framework on which to base the decisions on the source size, shape, etc. In the best of circumstances these decisions would be based on the theory of the operation of the source, however; there exists no clear theoretical description of an ECR so the trend over the last ten years or so led by Dr. Geller and his co-workers has been to find empirical "laws" based on observable quantities of the operating sources (Gel 87).

However, having just said that the first scaling law comes from classical electromagnetism. The electron density in the plasma, n_e, is given by:

$$n_e \propto \omega_{ECR}^2 \qquad (2\text{-}19)$$

as the plasma density is defined by the cutoff frequency ω_{ECR}. For n_e values greater than those of 2-19 the microwaves can not penetrate the plasma sheath so no further heating occurs. The partner of n_e in the figure of merit, τ_i ,(eq. 2-2) can not be derived from first principles and the following scaling law has been proposed:

$$\tau_i \propto B^{1.5} \qquad (2\text{-}20)$$

where B is the axial magnetic field strength. Still on the topic of the figure of merit the mean charge state produced by the source, q_{eff}, also is dependent on the above factors:

$$q_{eff} \propto \log n_e \tau_i \qquad (2\text{-}21)$$

$$q_{eff} \propto \log \omega_{ECR}^2 B^{1.5} \qquad (2\text{-}22)$$

Another factor of interest is the charge state which gives the highest current, q_{opt}. In this case there are three equations defining the scaling law depending on what source parameters are varied. If only the magnetic field is varied then:

$$q_{opt} \propto \log B^{1.5} \qquad (2\text{-}23)$$

If both the microwave frequency, ω, and the magnetic field are changed which is the normal state of affairs then:

$$q_{opt} \propto \log \omega^{3.5} \qquad (2\text{-}24)$$

Finally, if ω and B are not changed but the incident power, P, is then:

$$q_{opt} \propto P^{1/3} \qquad (2\text{-}25)$$

This scaling law is, however; considered to be naive (Gel 89b) since it does not take into account the stochastic heating part of ECR heating which limits the maximum electron energy.

The final scaling law is for the maximum ion current extractable for a specific ionization state, I_{q^+}:

$$I_{q^+} \propto \omega^2 M^{-1} \qquad (2\text{-}26)$$

where M is the species mass. This scaling law holds quite well when compared to the experimental results for the laboratories around the world (Gel 89b).

Chapter 3 The Source Design

3.1 Introduction

In this chapter will be described the initial design work which was involved in finalizing the actual construction plans. At this time, no mention will be made of any of the changes made after the first beam was extracted. First will be described the initial conceptual design, then the changes made to that design, and finally the design of the inner RF cavity.

3.2 Conceptual Design

When this thesis began in the summer of 1987 a conceptual design, the mirror coils, and the hexapole magnet were already in existence. T.M. Mattman, a co-op student at Simon Fraser University, had at this time looked into the hexapole design (Mat 86). The result of which was the existing hexapole magnet.

Dr. L. Buchmann, based on a talk given by Dr. W. Bechthold (Bec 85), had proposed a conceptual design of an ECRIS to be used on TISOL(Buc 86). Table 3-1 contains the constraints under which the source must perform and fig. 3-1 shows the design itself. This design was used as a basis for all later modifications.

Table 3-1: Specifications of the the TISOL On-Line ECRIS (Buc 86).

Part/Function	Description	Value
Solenoid	2 pieces, water cooled, iron yoke	B= 0.5 T at center of ≥ 15cm bore hole, length/coil =7 cm, I = 500 A
RF	power variable amplifier, about 10 m waveguide	$v = 10\,GHz, P \leq 2\,kW$
SmCo hexapole	alloy to be chosen, stand to designed	inner dia. >52 mm (to be designed). Surface field = 0.5T

31

Vacuum	two pumps, two chambers, support gas to be inserted,	both 350 l/s, gas flow: 10^{-2} /10^{-1}scc/s H_2
Body	stainless steel cylinder to be opened at both sides, air cooled, coupling to target box	Diam.: 14 cm Leng.: 23 cm 9" fast coupling
HV	source body and target body	20 kV
Extraction Electrode	movable cone/replaceable Einzel lens desirable	20 mm range

Figure removed from microfilm copy due to copywrite restrictions.

Fig. 3-1 Initial conceptual design of the ECRIS by Dr. L. Buchmann (Buc 86).

3.3 The Magnetic Confinement System

3.3.1 The Permanent Magnet Hexapole

The hexapole magnet was produced in West Germany by Krupp according to a TRIUMF design which was created with the assistance of Dr. Bechthold at Karlshruhe. An aluminum housing was designed to hold the permanent magnet material and to create the main multi-mode Rf cavity. Because of its good performance under hard radiation, see fig. 3-2, Koremax 200 (Sm_2Co_{17}) (refered to as Krupp (2:17) in fig. 3-2)was chosen as the magnet material. The housing has six slots milled in it to allow the passage of microwaves into the enclosed plasma volume. The housing also has channels in it to permit cooling of the magnet by either air or water.
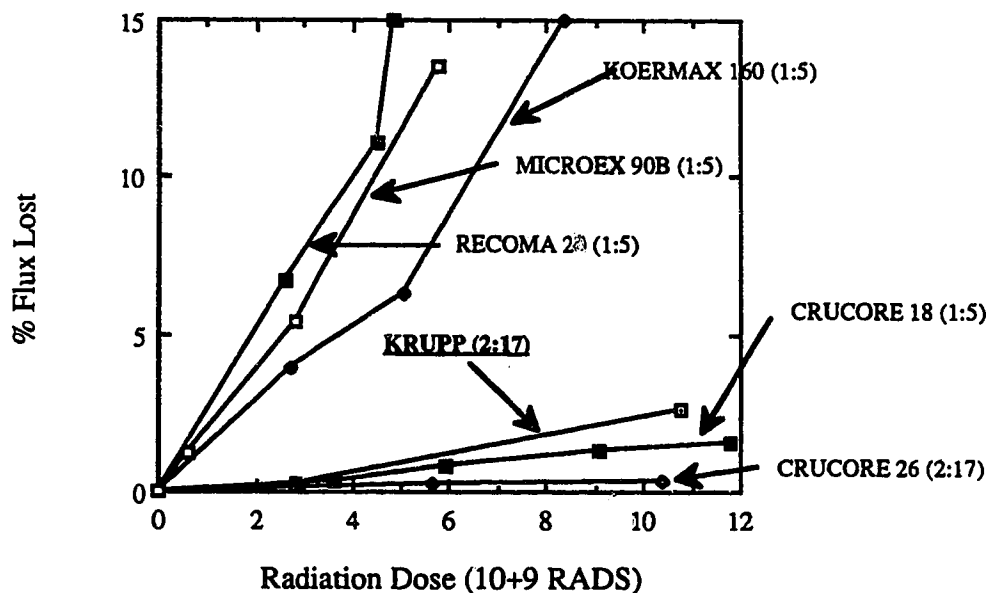
Fig. 3-2 The percentage of magnetic flux lost versus radiation dose for various permanent magnet materials.

Before construction the field was predicted using the HEXQR program supplied by

KRUPP. After construction, the field was mapped by the TRIUMF magnet survey group. A comparison between the total predicted field and the mapped axial field is shown in fig. 3-3. Only the axial part of the field could be measured as the bore of the hexapole was too small to insert the radial component measuring probe.
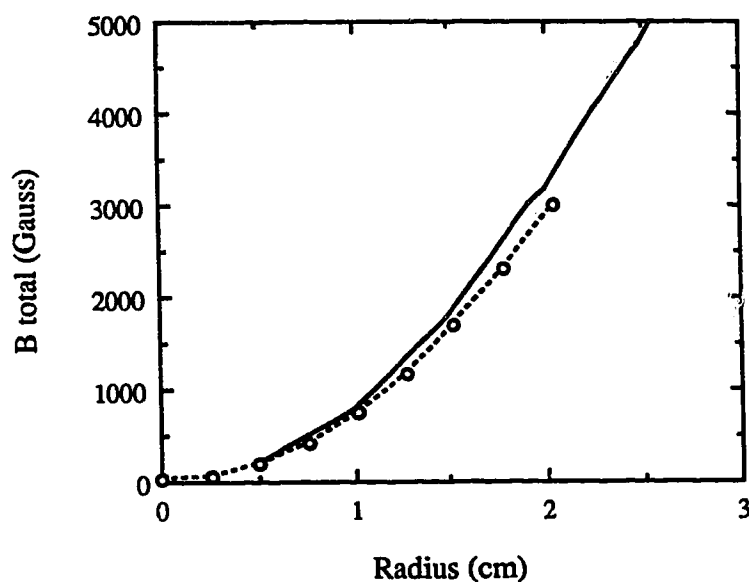
Fig. 3-3 A comparison of the predicted total magnetic field (—) to the measured axial magnetic field (o) for the hexapole magnet.

The axial component of the field as compared to the position on the axis is shown in Fig. 3-4. This figure demonstrates the uniformity of the field and the fact that it falls off quite dramatically outside the magnet itself; this means that the hexapole adds little to the fringe field of the source.
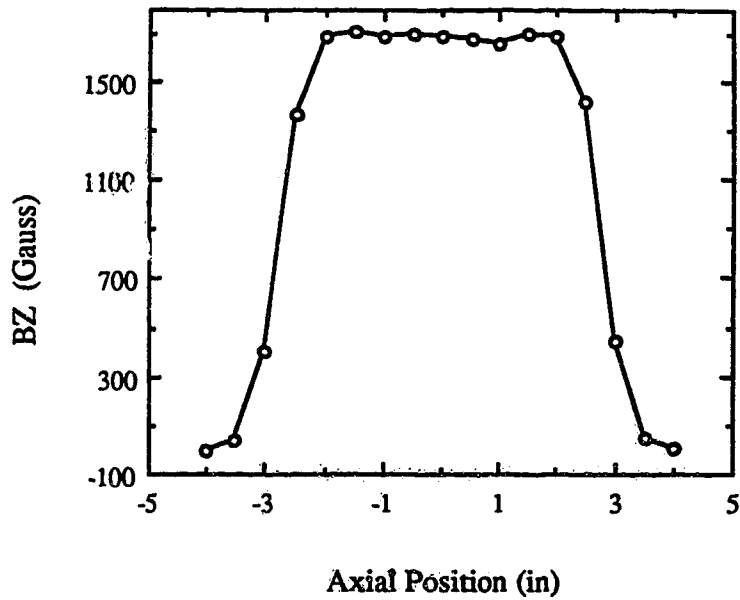
Fig. 3-4 A graph showing the axial magnetic field at R=0.60" compared to the axial position.
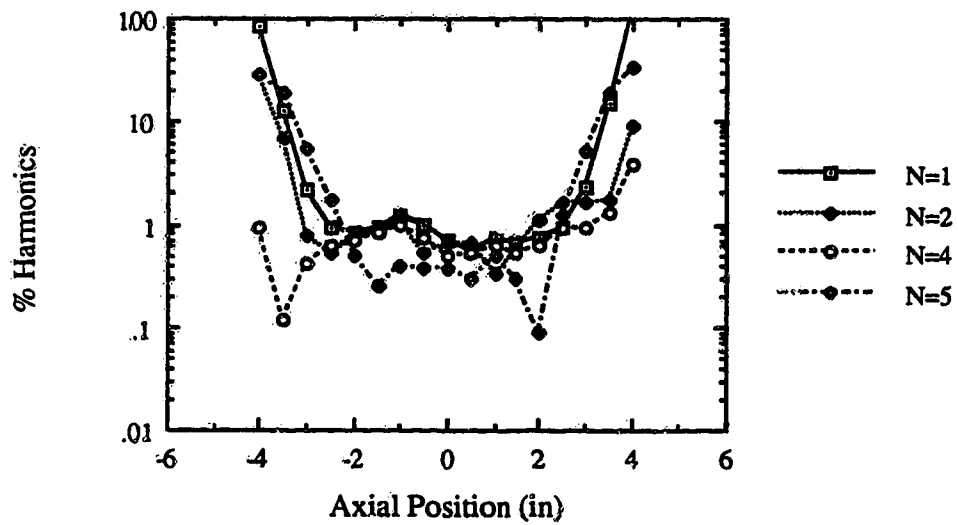
Fig. 3-5
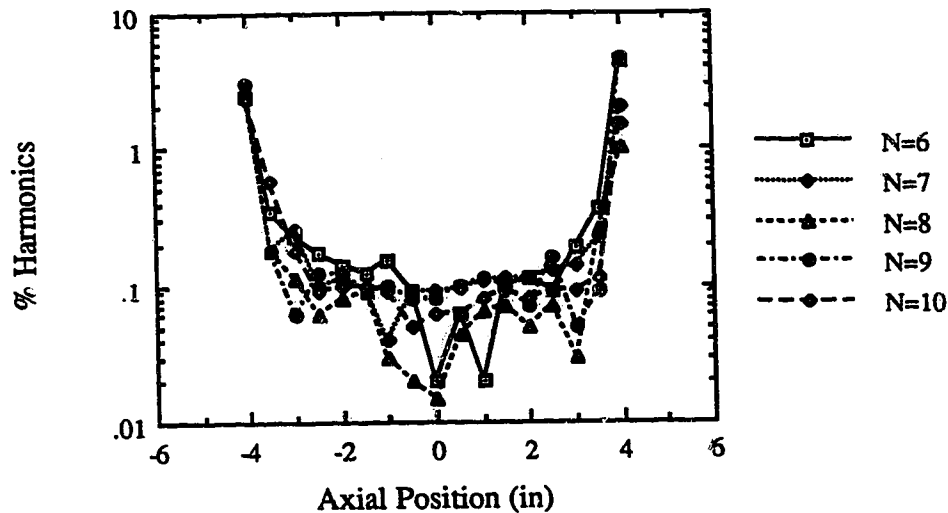
Fig. 3-5 The above two graphs show the % harmonics of the hexapole magnet versus the axial position.

3.3.2 The Mirror Coils

Dr. H. Schneider from Chalk River Nuclear Laboratories had provided the mirror coils, which consist of eight pancake coils arranged in two groups of four. These coils were used in both the conceptual design of the TISOL ECRIS and in the actual constructed source. Starting with T. Mattman's work which gave the magnetic field for the conceptual design a number of simulations using the POISSON program were done to see if it was possible to reduce the amount of steel in the magnetic yoke. The first fruit of this endeavor was the finding that the thickness of the yoke's cylindrical wall could be reduced to 2 cm from 3.5 cm without unduly changing the magnetic field strength or shape.

At this point M. McDonald began to design the actual yoke. Working to reduce the total weight it was attempted to reduce the thickness of the center portion which was

intended to produce the required dip in the field. The results were again encouraging and it was suggested to remove the connecting steel and replace it with a ring around the hexapole. This modification also proved successful. In fig. 3-8 the evolution of the magnetic yoke is shown as well as the field predicted for that configuration. In addition to the changes to the center region of the yoke the ends were also modified. The inner bore of the steel end caps was reduced from 12 cm radius to 5 cm radius. A pleasant side effect of these changes was the that the current required was reduced by 27% from 605.2 A/turn cm to 439.4 A/turn cm. A final modification to the inner steel section was suggested by Dr. J. Soukup in an effort to improve the transmission of microwaves throughout the RF cavity. He suggested that the inner ring have a triangular cross section. This was checked by computer simulation and was found to have little effect on the field. Based on these results a set of construction drawing were made and put into the TRIUMF machine shop. A final run of POISSON was done based on these drawings. After assembly of the steel yoke a magnet field map was made. In fig. 3-6 the mapped axial magnetic field is shown. An additional plot of the field is shown in Fig. 3-7.
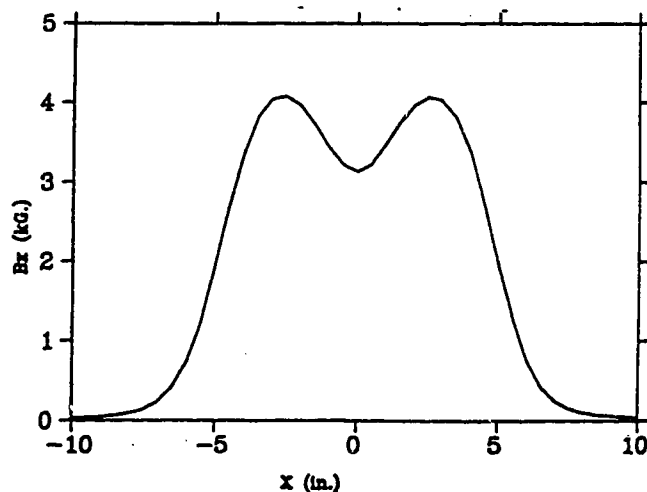
Fig. 3-6 The graph shows the measured axial magnetic field at R=0.0 cm for a current of 360 A. Note: "x" is the same as "z" used previously.
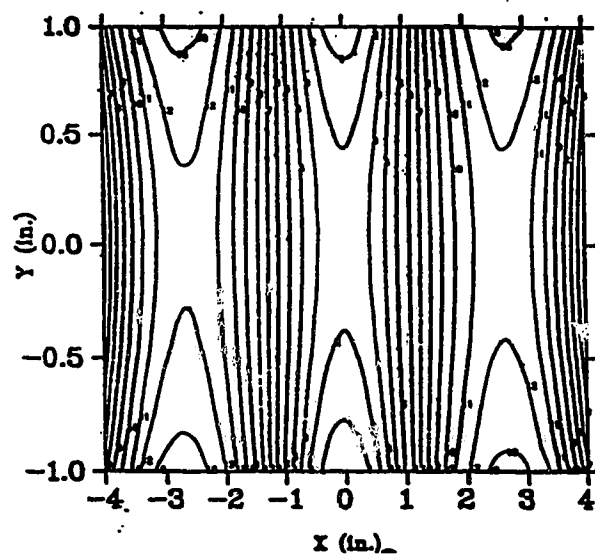
Fig. 3-7 The magnetic field contours compared to position in the horizontal plane with the value of 1 being 3 kG.
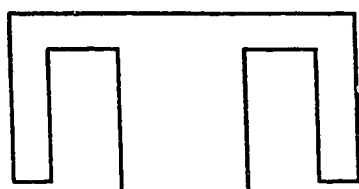
Initial conceptual design of the magnetic yoke
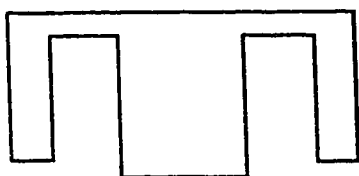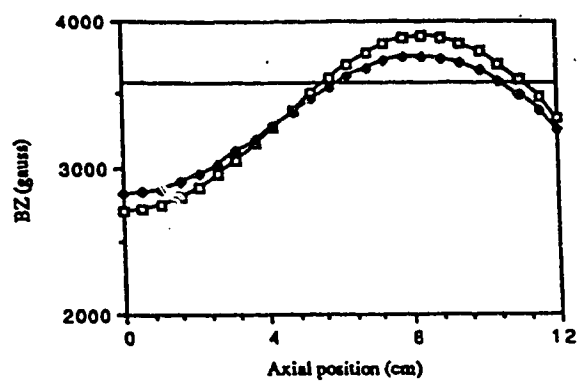
Modification to conceptual design: reduce cylinder thickness to 2 cm from 3.5.

Fig. 3.8

Modification to conceptual design: reduction of center plug size.

Modification to conceptual design: remove center piece and leave ring around hexapole

Actual design based on construction drawings
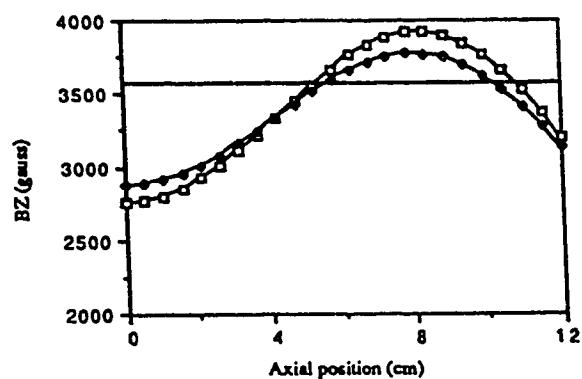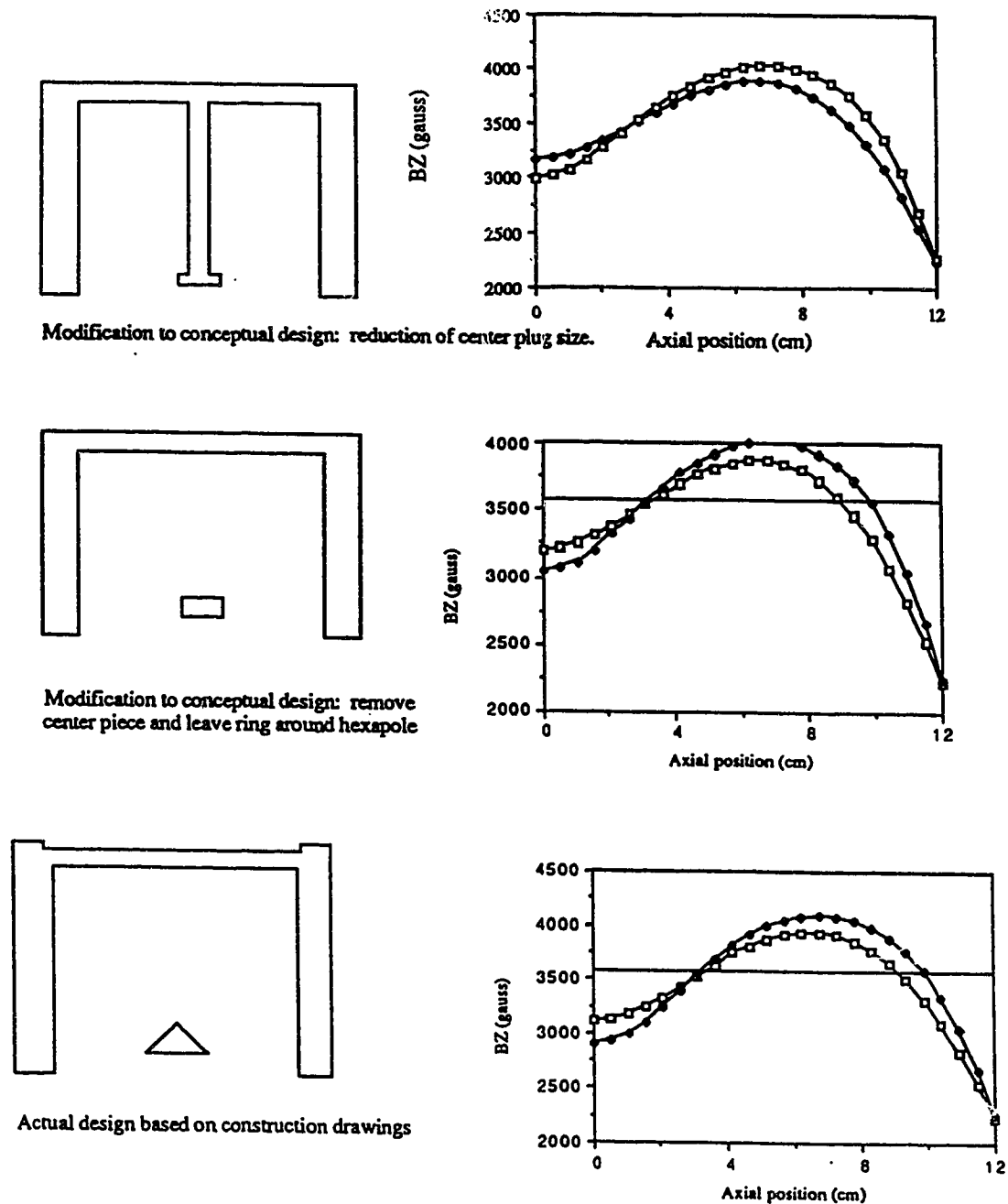
Fig. 3-8 The effect of changing the magnetic yoke geometry on the magnetic field predictions from POISSON. The magnetic yoke shown is half of a section view. The squares are the magnetic field at R = 2.5 cm while the diamonds are the magnetic field at R = 0.0 cm.

3.4 Inner RF Cavity

The problem now was how to produce the required multi-mode cavity without a great loss in microwave power. To contain the microwaves an aluminum *can* was to surround the hexapole. Since the entire RF cavity would be sitting at high voltage Delrin insulating flanges were mounted on each end. Great care had to be taken to shield the Viton O-rings on the inside from the RF field as the Viton would be slowly eroded by the field. Since the hexapole magnet coolant (in our case air) had to enter and leave the magnet from the rear the design of the mounting flanges was quite complex. An exploded view of the whole assembly is shown in fig. 3-9. As an additional feature air was blown through the cavity and up the wave guide to directly cool the inside of the cavity. A window was included to allow direct viewing of the the plasma.

The plasma electrode, the electrode through which the plasma is extracted, was mounted on the downstream aluminum flange in such a way that it could be removed from the inner RF cavity without disassembling the source. The plate which faced the plasma was made of tantalum and was mounted on the removable electrode insert so that the plasma aperture size could be varied by a simple exchange of plates. This design suffered from two faults: it was not a Pierce geometry, and the walls of the cone did not begin at the aperture.

The final modifications in the RF cavity were to replace the existing stainless steel screws with counter sunk brass screws and to copper plate the steel ring. In both cases the goal was to decrease the amount of RF power absorbed by the cavity. The final changes made to the body of the source were to bore channels through the rear steel center piece to allow air cooling lines to be attached, and to bore of a hole at the top of the source for the waveguide to go through. The waveguide was surrounded by a Delrin spacer to prevent arcing from the waveguide to the body of the source.
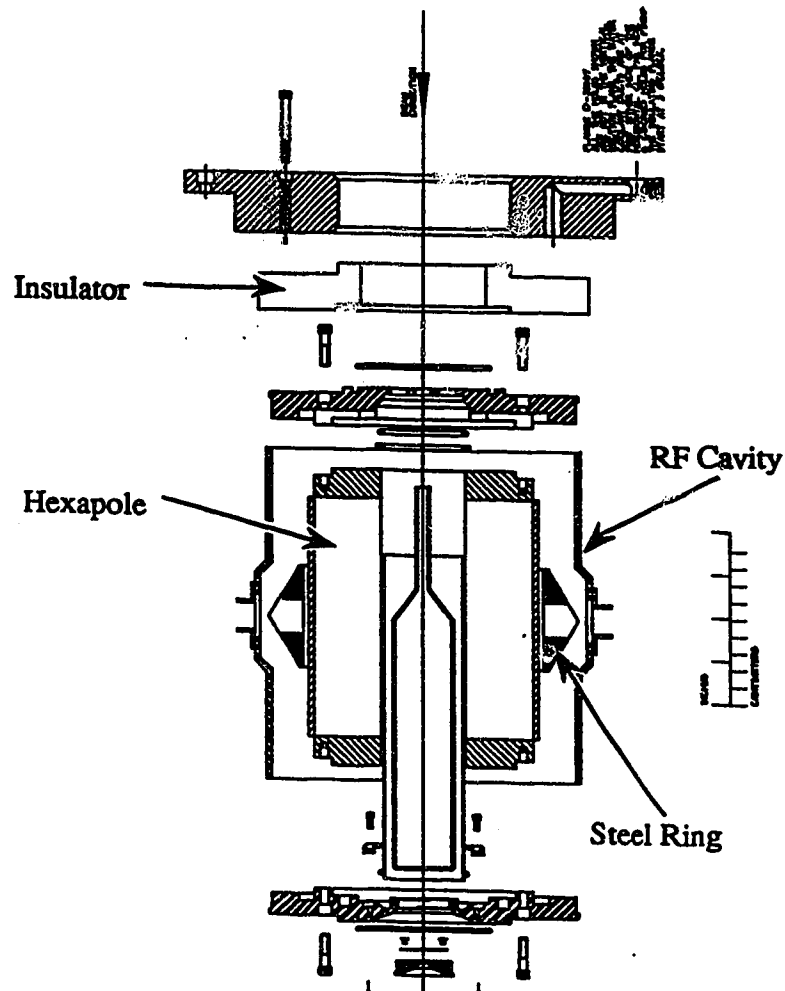
Fig. 3-9 The components of the inner RF cavity.

The final part of the upstream vacuum seal was made by an aluminum end plate. Included on this plate were a seal around the stem of the inner quartz tube and a vacuum pumping port. The original plan had been to pass a vacuum line around the outside body of the source to allow for simultaneous pumping from both the up and down stream sides of the space between the inner and outer quartz tubes.

3.5 Field Map of the Magnetic Field

The inner cavity without the quartz tubes was installed on the source and another field map of the axial field was made to see what effect the hexapole would have. See fig. 3-10 for a comparison of the predicted field to the mapped field with the hexapole in place.
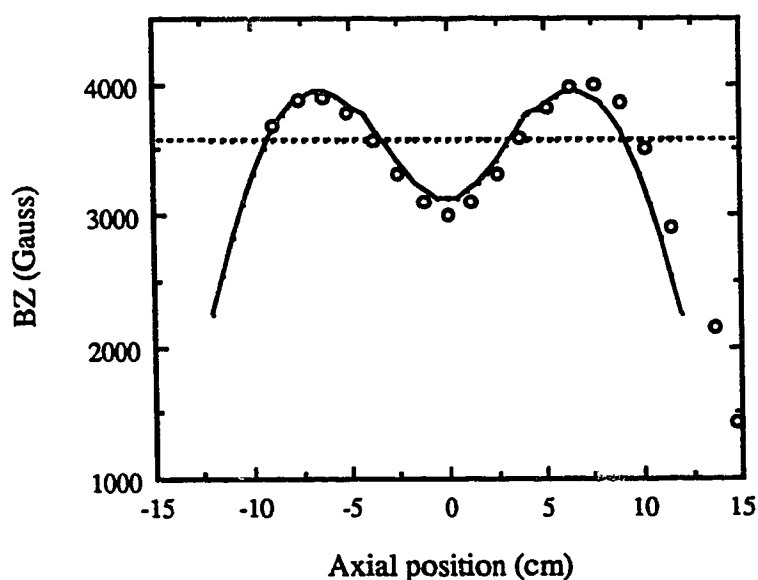
Fig. 3-10 A comparison between the predicted field (solid line) and the measured field (o).

3.6 The Extraction Electrode/ Einzel Lens Assembly

The final and most important (although its significance was not appreciated at the time) system remaining was the movable extraction electrode and einzel lens assembly. The design used was done by R. Kokke based on Dr. L. Buchmann's conceptual design. The puller electrode, the electrode which causes the ion extraction and provides the initial

beam focusing, had a hole diameter of 1 cm as it was intended to test the effect of hole size by the use of inserts of various hole diameters. The einzel lens consisted of three aluminum rings, the center one (which was at high voltage) mounted on a block of boron nitride insulator. The rings were 0.25" thick and were separated by ~1 cm. The rings each had an inner bore of 1.5".

By using a cannibalized part of the TISOL Extraction Electrode system the whole Extraction Electrode / Einzel lens assembly could be moved along the beam axis. There was, however; a problem. The alignment could not be checked in *situ*. This required that the alignment be done in a separate box with the aligned system transferred back to the test bench. All alignment was done without the aid of proper instruments and there was no way to test the source - puller electrode alignment.

To determine the position of the puller electrode in the box a ruler was placed on the outside of the extraction system mounting plate to read the amount by which the shaft moved in or out. The conversion of that horizontal motion to that along the beam axis was that 1 cm horizontal was 0.6 cm on the axis.

An assembly drawing of the completed source is shown in fig. 3-11. This drawing shows the the choke stack assembly which was not added until after the initial runs were complete.
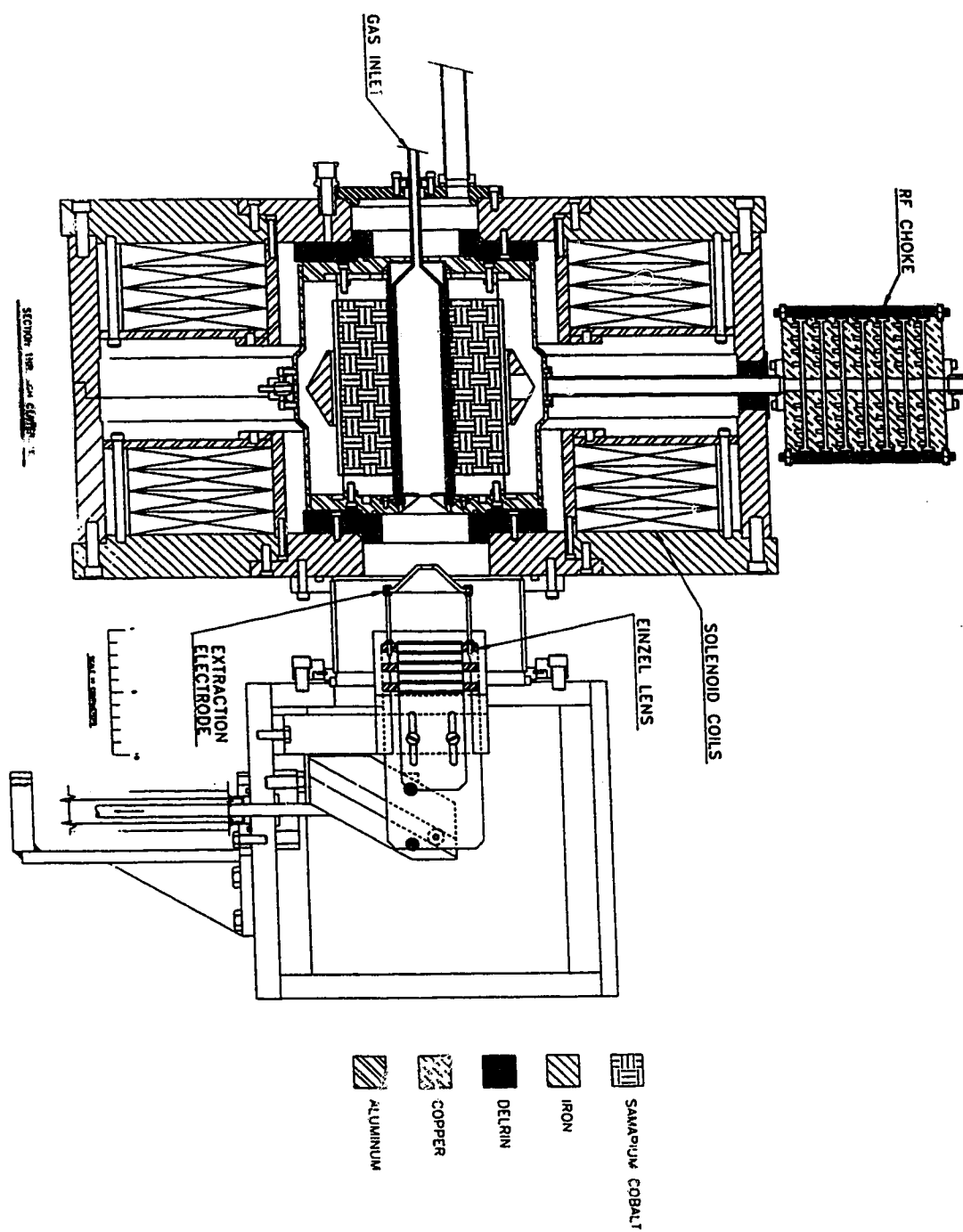
Fig. 3-11 Diagram of the source as it was initially constructed.

Chapter 4 The Off-line Test Facility

4.1 Introduction

Since the purpose was to test the source under a variety of operating conditions the test bench had to be versatile enough to give the options necessary. The data obtained from the bench would also have to provide a sufficient amount of information for an accurate analysis to be undertaken. The testing facilities were provided by Dr. P. W. Schmor in the CRM at TRIUMF. This chapter will describe the various elements of the test bench and how they evolved. The first section will be the microwave system, then the vacuum system, next will be the analysis system, and finally the control system.

4.2 The Microwave System

The microwave system was the single most important element of the test bench for the simple reason that most of its components were effectively irreplaceable. The microwaves were generated in a 10 GHz Gunn oscillator and then fed into a Varian TWT Model VZX-6983G1 200W power amplifier. Part of the equipment in the amplifier consisted of a internal cross guide coupler (with an attenuation of 42.4 dB) to measure the forward power exiting the amplifier. After the amplifier there was a 10GHz filter and a circulator which would direct any reflected waves into a dissipative load. Next was a cross guide coupler which was oriented to measure the reflected power. It has an attenuation of 30 dB. Before entering the source the microwaves passed through a choke stack whose purpose was to break the high voltage bias of the source so that the waveguide could be at ground. Finally, since the internal wave guide of the source was a 6.6 GHz guide there was a horn which converted the guide from 10 GHz to 6.6 GHz. This was done since it is intended to purchase a more powerful RF amplifier for the on-

line operation of the source and a 6.6 GHz source is more cost effective. A schematic of

the microwave feed system can be seen in fig. 4-1.
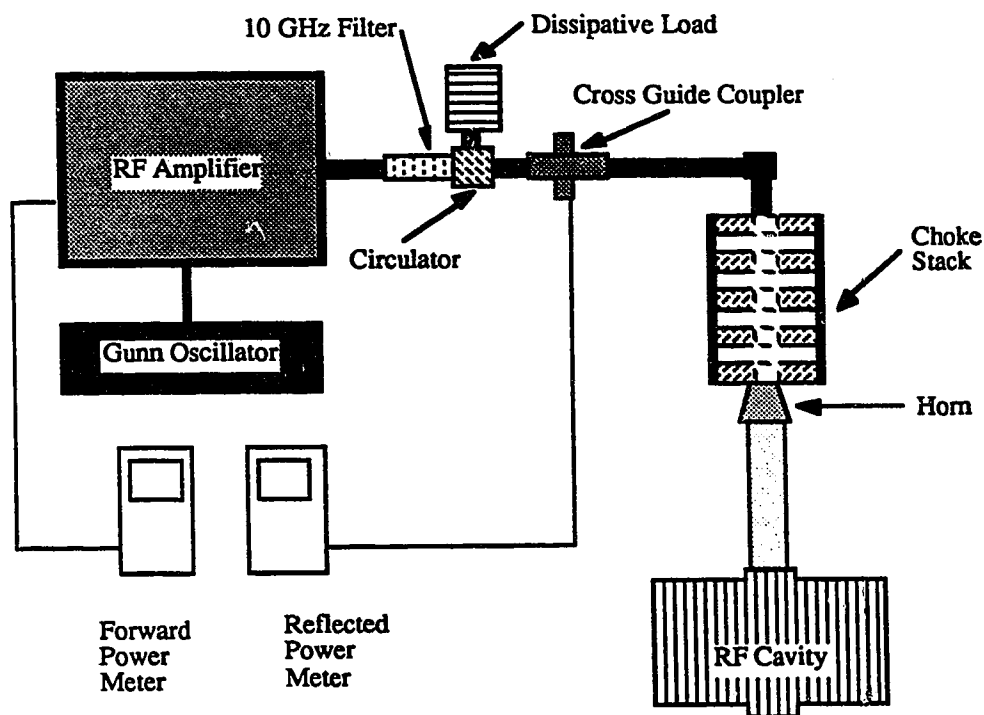
Fig. 4-1 A schematic of the RF power system for the ECRIS.

4.3 The Vacuum System

The vacuum system was, unfortunately, the most poorly designed of any of the

support systems. The entire test bench system is shown schematically in fig. 4-2, and a

close look at the vacuum components will quickly reveal that Box 1 cannot be easily

roughed out except by using the turbo pump which means that you have to pump down

the beam line as well as the source before you can open up the gate valve isolating the

diffusion pump. Other than this problem, however, the system worked fine with a base

pressure of ~5x10^{-7} Torr. With gas flowing into the source a pressure of 2x10^{-6} Torr

could be obtained routinely.

At the beginning it was intended to run a vacuum line from Box 1 to the back of the source to allow for pumping from both ends on the vacuum between the quartz tubes. There was a problem in getting a KF-50 to a KF-40 adaptor flange and so this was never accomplished. But at the end during the high tension runs (see chapter 7) a 2" diffusion pump was connected to the port on the rear flange and pressures of ~10^{-6} Torr were obtained in the upstream end of the source.
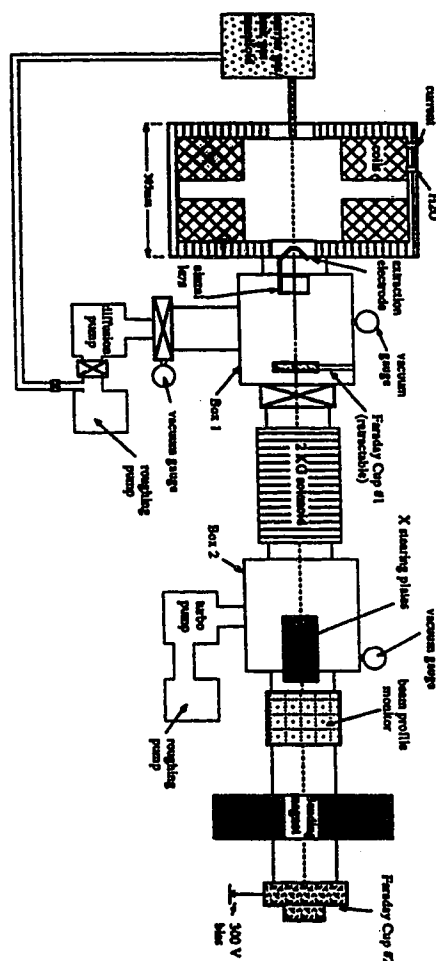
Fig. 4-2 Schematic layout of the off-line test facilities beamline showing both the vacuum and analysis systems.

4.4 The Gas Handling System

The gas feed system underwent perhaps the most changes of any of the auxiliary systems. Initially the system consisted of a single calibrated leak attached via a "T" to the hydrogen gas line. The mixed gas was brought to the inner quartz tube by a tygon tube. The flow of H_2 was controlled by an electronic flow controller. The flow controller operated by detecting the temperature induced change in the resistance of a metal strip which the gas flowed by; this information was then turned into a flow reading. Tygon tubing was chosen because the diffusion rate for outside gases to penetrate the walls of the tube is smaller than from polyflow tubing. This system had a number of problems, the main one being that it was leaky and the leaks were hard to cure due to the large number of swagelock fittings. Next, the tygon did allow some gas to diffuse through it so the runs with the N_2 calibrated leak were nearly impossible. Additionally it collapsed under vacuum slowing the pumping speed. Finally there was only one carrier gas-leak gas combination available at any one time and to change these meant the source had to be brought up to atmospheric pressure and then pumped down overnight. The reason for this was that when the leak bottle was detached the inner quartz tubes were exposed to air.

To correct these problems a manifold was assembled which mounted all three of the calibrated gas leaks available (Nitrogen, Neon, and Argon). Attached to this was a copper transfer line which via a stainless steel bellows and a stainless steel swagelock connector coupled to the inner quartz tube. Two additional carrier gas bottles (Nitrogen, and Helium) were connected in between the Hydrogen shut off-valve and the flow controller. Since the flow controller was insufficiently accurate to produce the low flow required a needle valve was installed between it and the leak gas manifold. As this valve

effectively isolated the gas line insofar as pumping was concerned, another roughing line just downstream side of the needle valve was added. A schematic of the final system is shown is fig. 4-3.
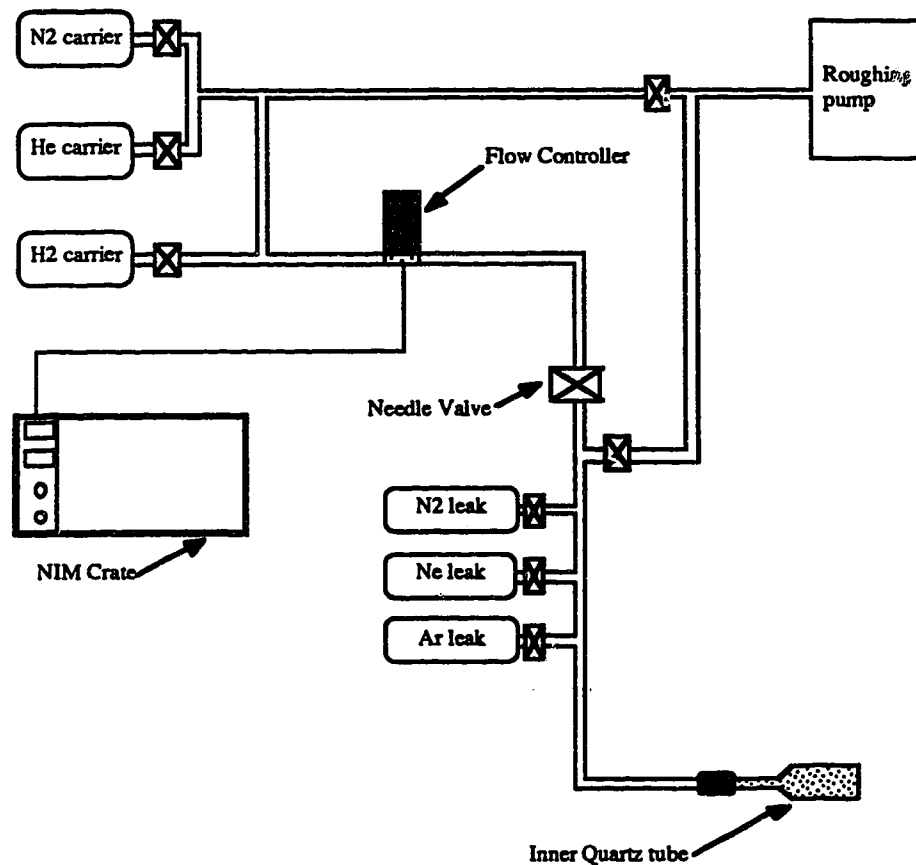
Fig. 4-3 This is a schematic of the gas handling system.

4.5 The Analysis System

4.5.1 The Particle Focusing and Steering System

The analysis system consisted of a set of focusing/steering elements and some simple beam measurement apparatus. There were three focusing elements on the beam line. The closest to the source was an Einzel lens operating in accel-decel mode. The initial lens design can be seen in fig. 3-11. This lens did not work very well. It had hardly any effect

on the beam. As a result a new design was tried (see fig.4-4) and there was substantial improvement. The first lens design was operated at a voltage of about -100V while the second design was operated at -(5-10) kV.
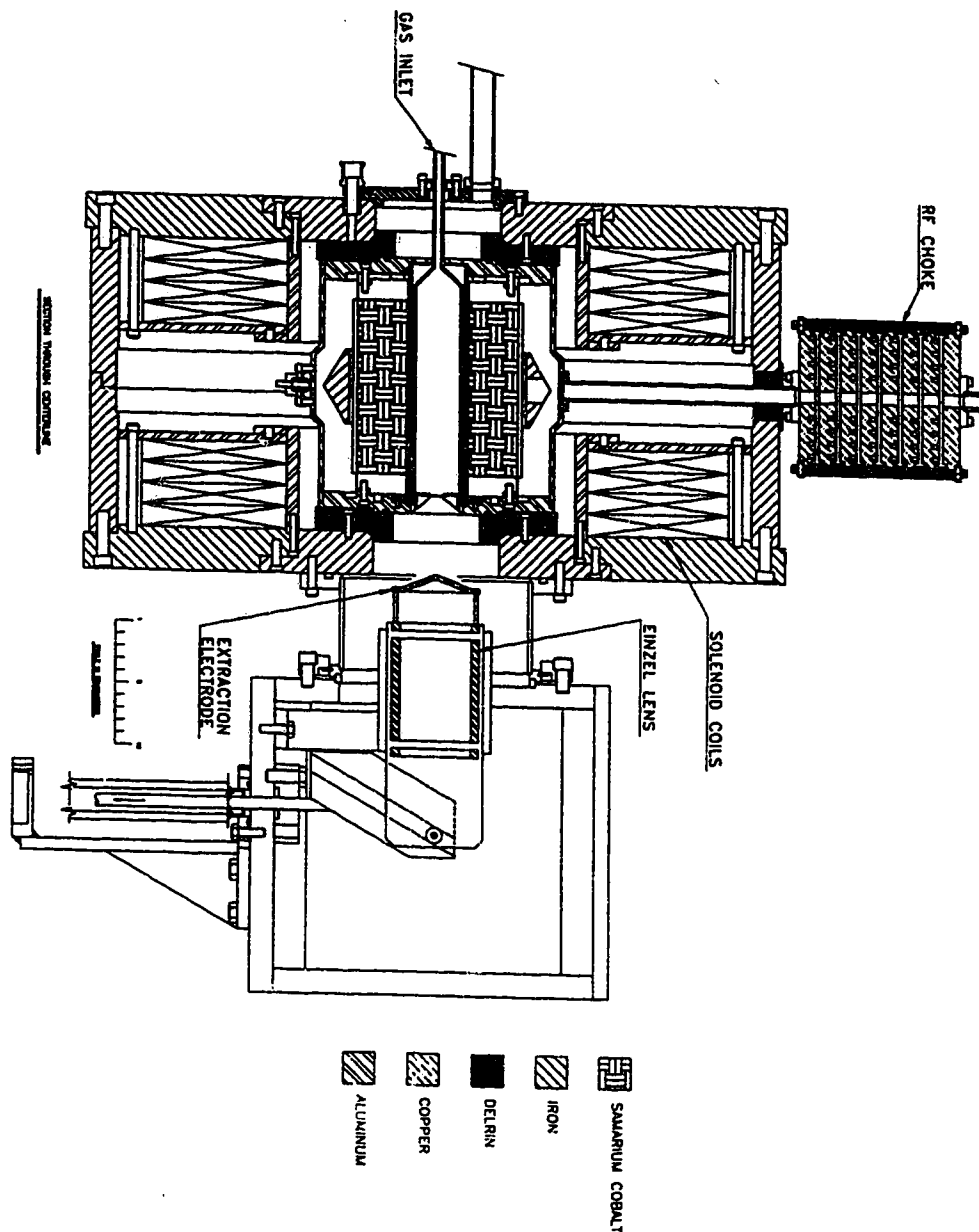
Fig. 4-4 A diagram of the source after changes were made to the extraction system.

The second focusing element was a solenoid whose field was variable up to 2 kG. In the initial runs before the einzel lens was rebuilt, almost all of the beam focusing was done with the solenoid; with the new design the roles were reversed. No attempt was made to accurately record the solenoid current values which gave a specific solenoid field, as adjustment was an on-going process depending on the source parameters and the species of interest.

The final beam focusing element was a set of X-steering plates. These plates could be charged with either a negative or positive voltage to bend the beam left or right. As long as the beam profile monitor was operational this set of plates was quite useful, allowing the beam to be easily centered on axis. Due to a lack of foresight a set of Y-steering plates were not installed at the same time as the X plates. Fig. 4-2 shows the location of these three focusing elements in the beam line.

4.5.2 The Particle Identification System

Particle identification was accomplished by the use of a dipole magnet acting as a mass spectrometer. The magnet was a modified steering dipole with a 2" gap width. The magnet had already been mapped and its field can be seen in fig. 4-5. The vacuum box had an entry and exit beam pipe diameter of 1.5" which had to be coupled to the 4" diameter beam pipe mounting the beam profile monitor. The radius of curvature that a particle has to follow to go from one beam pipe to the other is 28.3±1.3 cm. After this had been measured plots were then done to determine the magnetic field required to bend the appropriate ion, depending on the extraction energy. The results for 5 kV extraction voltage are shown in table 4-1.

Table 4-1: The magnetic field required to bend ion species at 5 kV extraction voltage.

Species	Magnetic Field (kG)
H^+	0.36
He^+	0.72
He^{2+}	0.36
N^+	1.35
N^{2+}	0.68
Ne^+	1.67
Ne^{2+}	0.79
Ar^+	2.25
Ar^{2+}	1.15

Luckily the magnet was highly linear with the B vs I curve having a slope of 0.474 kG/A. In practice, the method of identifying ions used was to take the square of the ratio of the current setting for the species of interest to the current setting for hydrogen. This procedure would give the m/q value for the ion.
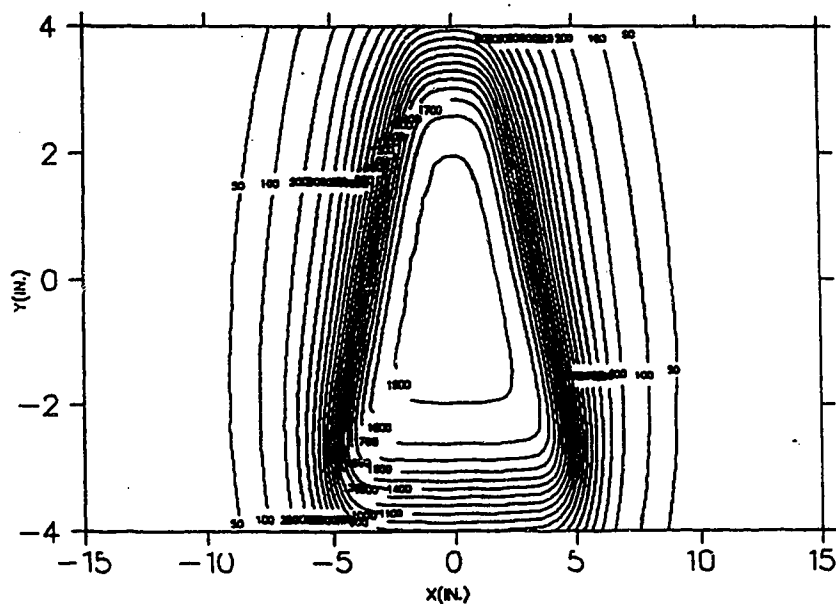
Fig. 4-5 Contour plot of the bending magnet's magnetic field.

4.5.3 Current Measuring System

The main task for analysis fell onto two Faraday Cups. Faraday Cup #1 (F/C #1) was located in Box #1 and could be retracted out of the beam. Its purpose was to measure the total beam extracted from the source. There was no bias on the plate since it was found that a bias made only a small (~10%) difference in the current observed. Faraday Cup #2 (F/C #2) was mounted after the analysing magnet. This faraday cup had a 1 cm diameter hole in a biased (to -300 V) plate mounted just before it and was used to measure the current of a specific ion species.

The current from F/C #1 was measured either by a Keithley electrometer or else by a Fluke pocket multimeter which could read down to the microampere region. F/C #2 was always read out by a Keithly electrometer. A current integrator consisting of a clock, current digitizer, and counter was also available but rarely used since it was simpler just to read the value from the Keithly electrometer. If an X-Y plotter had been available this could have been connected to both the Keithly electrometer and the analysing magnet power supply to give a plot of the current versus the magnetic field, thereby enhancing the speed of data collection.

4.6 The Control System

The test bench consisted of many pieces of equipment some of which had to be protected against an accidental failure of other parts of the system. This task was accomplished by the use a Gould Modcon Micro 84 Programmable controller. The Modcon would simulate a hard-wired relay network and thus allow the symbolic construction of easily modifiable interlocks to control the various elements of the test bench. The system also had the advantage of allowing the user to over-ride an interlock and activate a device "manually."

The interlocks could be divided into two basic groups: the vacuum interlocks and the protection interlocks. The vacuum interlocks ensured that the vacuum pumps were not exposed to the incorrect pressure for operation and also protected the pumps from vacuum failure. These types of protections were mainly on the diffusion pump as either the turbo or roughing pumps have less stringent safe operation requirements.

The protective interlocks on the other hand were intended to protect the source from failures of the support services. As an example, the RF Power Amplifier was interlocked to air pressure, water flow through the solenoid coils, and to proper vacuum in the beam line. Thus a failure in any of these systems would result in the RF Amplifier being shut down. The other main protective interlocks were: the Brentford power supply, which provided power for the solenoid coils, shared the same interlock as the RF Amplifier to water flow through the solenoid . The high voltage power supplies (the bias supply, and the einzel lens supply) were interlocked to the vacuum quality in the beamline.

There were only two problems with this arrangement. The first was that as the amount of time the source was operating increased so did a number of mysterious water pressure failures which would trip the Brentford power supply and the RF amplifier. H. Wyngarden discovered the cause after exhaustive experimentation. The water line which fed the source was also connected to the washroom across the hall and so when the toilet was flushed the water pressure would sometimes drop below the critical mark, thereby shutting down the source. This was solved by switching to an independent water main. The other problem had to do with the air pressure for the gate valves. Since the air used by the hexapole magnet for cooling came from the same regulator that provided pressure to keep the valves open (or closed) after a while the pressure would drop as the compressor could not supply enough air (note: one compressor supplied air for the whole

building). This was finally solved by using only a small amount of air for cooling. Compressed air is not the best choice for a coolant as a high flow rate but low pressure air supply would do a better job. The reason being that the cooling is provided by the volume of air flowing through the cooling chanels rather than the pressure the air is at.

Chapter 5 Initial Operating Experience

5.1 Introduction

This initial data was collected in the main during the week before leaving to attend the International Workshop on ECRIS at Grenoble, France. It represents the first actual experiences with an operating ion source. It should be stressed, especially with regard to the second section, section 5.3, that there was a rush to get *some* kind of reportable data. The chapter is divided into two sections. The first will deal with the initial plasma formation and events leading up to the actual extraction of beam. The second will deal with the data collected in the first six rather chaotic days of running.

5.2 Initial Plasma Formation

This part of the chapter will concentrate on the data collected on the two days of the plasma run. However, before describing that data there were a few tests done on the source are worthy of note.

Chapter three showed the magnetic field maps of the mirror coils. These measurements were done at basically only one current with a different power supply than the Brentford power supply. Therefore a few simple measurements were performed on the coils after mounting the coils on the test bench. A portable Hall probe was used to measure the magnetic field. The first test was to find the maximum possible current through the coils. This was determined by observing the water temperature in the poly flow tubes: it was found that at 560 A (corresponding to a value of 0.5 on the remote control potentiometer) the polyflow tube was beginning to soften. In view of this a warning was attached to the remote control box for the Brentford power supply advising against turning the potentiometer below 1.5. Additionally the linearity of the magnetic field and the remote control were tested, the results can be seen in fig. 5-1. The formula to convert a potentiometer dial number (or R/C setting) to a current is given below:

$$I = -58 \bullet (\text{Pot \#}) + 589 \qquad\qquad (5\text{-}1)$$

Finally, the voltage at the coils was found to be 34.1 V at 320 A whereas the Brentford power supply showed 35 V indicating a low loss situation.
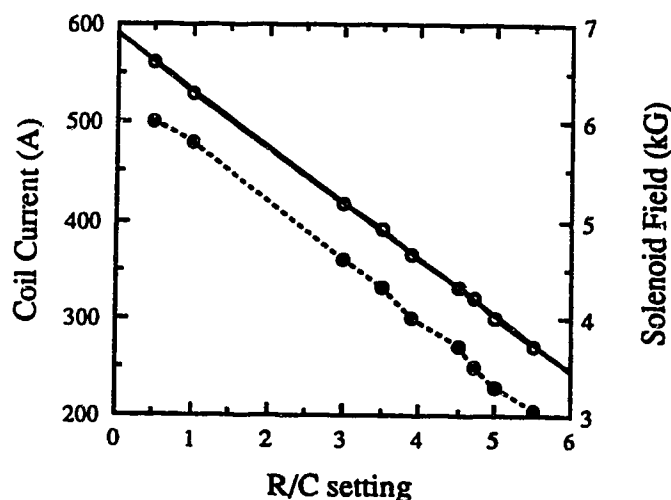
Fig. 5-1 The dependence of the solenoid coil current (○) and the observed magnetic field (●) on the setting on the Brentford remote control potential meter.

Several problems were evident during the first assembly of the inner RF cavity. First the whole assembly was too tall by 4.3 mm. This required that the upstream steel end flange have 3.8 mm skimmed off it. Second, the inner quartz tube was too long and was crushed when the aluminum end flanges were tightened together. As a result a new set of inner quartz tubes had to be made with the main tube length shortened from 170 mm to 150 mm. As the original quartz tubing was unavailable these new tubes has a slightly smaller diameter.

While this was going on the design of the Extraction Electrode / Einzel Lens assembly was finalized (see chapter three for details on this assembly) and put into the shop. The first piece completed was the connector between Box 1 and the source itself. There was some trepidation at this point since three different designers had worked

independently on the plans and there was no guarantee everything would fit together--but it did and the plasma test could be carried out. It should be mentioned that not everything was ready for the test. Of primary importance was the fact that neither the choke stack nor the horn had been assembled so it was impossible to bias the source and the RF feed came from the 10 GHz waveguide being simply clamped onto the 6.6 GHz waveguide flange. M. McDonald and Dr. P. Schmor were present with me when the first plasma was generated on August 9, 1988. We were pleased that the source worked although how well it worked we had no way of knowing. Some of the results obtained on that first day are shown in table 5-1.

Table 5-1: Plasma test results from the initial plasma generation.

Forward RF Power (W)	Reflected RF Power (W)	Gas Flow H_2 (sccm)	Pressure Box 1 (10^{-6} Torr)	Brentford R/C Setting (Arb. Units)
17.4	1.8	0.22	??	4.0
17.4	1.8	0.15	3.0	4.0
17.4	1.8	0.09	2.6	4.0
17.4	1.8	0.05	1.85	4.0
17.4	1.9	0.17	3.2	4.0
34.8	3.6	0.17	3.2	4.0
52.1	4.6	0.17	3.2	4.0
69.5	5.2	0.17	3.2	4.0
86.9	5.8	0.17	3.2	4.0
86.9	5.4	0.20	3.5	4.0
86.9	5.6	0.25	4.2	4.0
86.9	5.5	0.25	4.2	4.5
86.9	4.3	0.25	4.2	4.4
86.9	4.2	0.25	4.2	4.3
86.9	5.8	0.25	4.2	4.2
86.9	5.8	0.25	4.2	4.1

In addition to the above data the effect of various parameters on the reflected RF
power was investigated. In fig. 5-2 the effect of the coil current and hence the magnetic
field is shown for a forward power of 121.6 W and 34.8 W. Both curves show a
pronounced dip at a potentiometer setting of 4.4 corresponding to a current of 336 A.
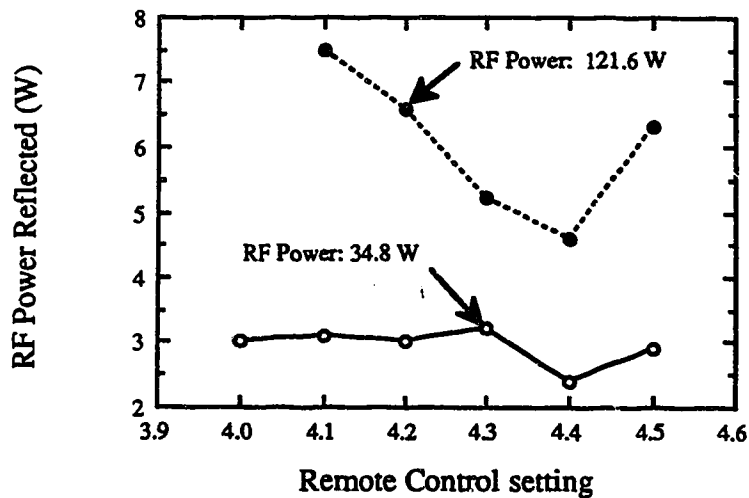
Fig. 5-2 The amount of RF power reflected for two different RF power levels incident
on the source as a function of the Brentford remote control setting.

The final test was to see how the reflected power varied with the forward power. In
fig. 5-3 the reflected power curve is shown. Identical results were obtained on the two
different days of running.
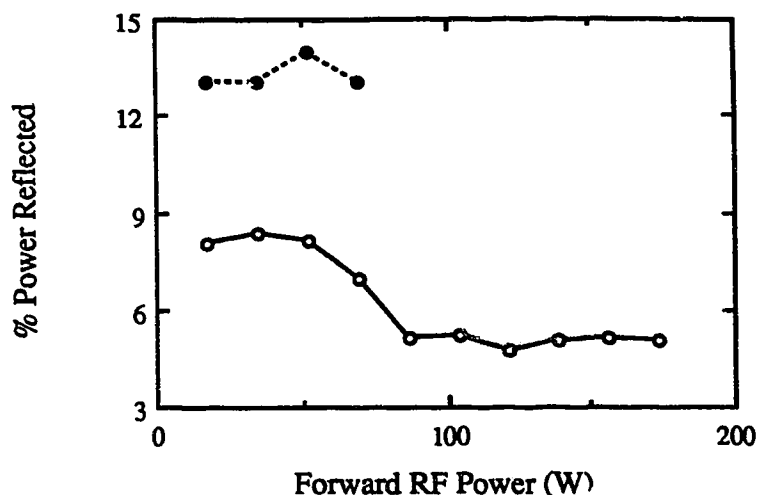
Fig. 5-3 The percentage of the incident power reflected as a function of the incident power for the initial plasma run (o) and with extraction occurring (●).

5.3 Initial Beam Extraction Runs

5.3.1 Preparations for the Run

This section will present the data collected during the first operational run, which lasted from August 24 to August 30, 1988. The gas mix that was available was hydrogen as a carrier gas and nitrogen as the leak gas. The horn was missing from the microwave system. This meant that the choke stack sat directly above the source's internal waveguide and was held in place by a C-clamp. The X steering plates and the bias on F/C #2 were also missing from the test bench at this time.

First some of the data collected will be presented and afterward some conclusions based on what was observed will be drawn. The main object here was to learn how the source operated rather than to collect precise data. A major difference between these runs and the plasma runs, which had preceded them, was the fact that the amount of reflected RF power had increased dramaticaly (see fig. 5-3). This limited the usable forward power to ≤ 70 W in order to avoid damage to the power head on the crossguide

coupler. A possible cause for this was that the choke stack, now included, by its design or method of operation caused more reflection to occur. It also could have been that the direct coupling of the choke stack to the internal waveguide caused the problem. To allow the reflected power to be measured an additional piece of coaxial cable was attached between the crossguide coupler and the powerhead. The cable attenuation was determined by a simple experiment. The reflected power observed both with and without the cable in place for selected forward RF powers was recorded and the data is shown below in table 5-2.

Table 5-2: The data collected to determine the attenuation value for the coaxial cable added between the crossguide coupler and the power head.

Forward Power (W)	Reflected Power without Cable (W)	Reflected Power with Cable[1] (mW)	dB of Cable and Coupler
17.4	2.2	0.5	36.4
34.8	4.5	1.3	35.4
52.1	7.9	1.5	37.2
69.5	9.7	1.85	37.2

[1]shows the raw data observed on the power meter; has not been converted yet.

This data gives a mean and standard deviation of 36.55 ± 0.74 dB for the coupler and cable combination. The value of the cable and coupler's attenuation was determined by the following formula:

$$dB = 30 - 10 \log \frac{P_{ob \, (cable)}}{P_{ob \, (without)}} \qquad (5-2)$$

5.3.2 Mass Spectrum Data

The beam data was initially collected in a series of "identification" runs where the

magnetic field of the analysing magnet was first increased and then decreased. The purpose of this was to ensure that the species identification assigned to a particular m/q value was correct and to ensure that any current observed was in fact there. There were unfortunately two problems associated with this procedure. The first is the obvious hysteresis of the magnetic field which will shift the current values and since this shift is not constant the m/q values from one direction do not correspond exactly to the other thus increasing the difficulty of assigning a species name. The second problem was that often peaks would show up in one scan direction but not in the other. It was most common that a "new" peak would be found while decreasing the magnetic field. The reason for this is that it was much easier to see an increase from 0, a peak, a small decrease, and then an increase to a large peak then the reverse which looked like a decay to 0. An example of both of these problems is shown in fig. 5-4.
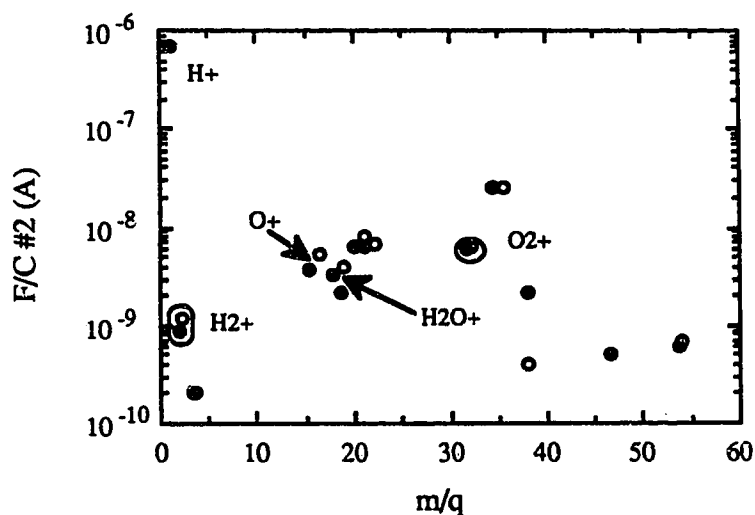
Fig. 5-4 An example of the problems caused by runs where the magnetic field of the analysing magnet was increased (o)and then decreased(•).

The best spectrum data was collected on the last two days of running. In the first three spectra (see figs. 5-5a, 5-5b, 5-5c) shown all external conditions are the same (see table 5-3) but a different gas and hence a different RF power absorbed (see table 5-4) was used in each.

Table 5-3: The common external settings for the data collected on Aug. 29 / 88.

RF forward Power:	104.4 W
Extraction Voltage:	5 kV
Extraction Gap:	0.55 cm
Solenoid Coil Setting:	3.82

Table 5-4: The individual parameters for the three runs on Aug. 29 / 88.

Gas Type	Flow (atm-cc/s)	Net RF Absorbed[1] (W)
leaked atmosphere	3.2×10^{-3}	90.2
Nitrogen gas leak	6.22×10^{-8}	82.5
Hydrogen and	6.7×10^{-4}	83.4
Nitrogen gas leak	6.22×10^{-8}	

[1] calculated by subtracting the reflected power from the forward power.

There are some trends which are common to all three graphs. The first is that the disagreement between the m/q values obtained increases with increasing m/q values. This might be caused by non-linearities in the magnet as it is operating at close to its maximum rating. Another possibility is that the fringe field effects are no longer negligible.
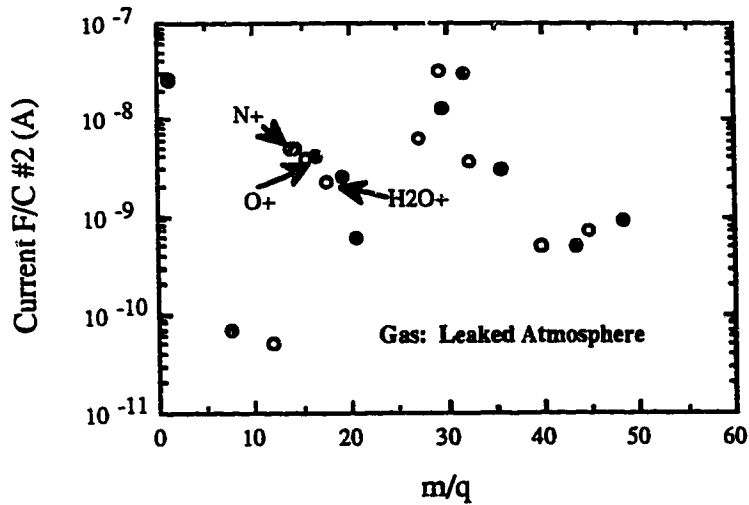
Fig. 5-5a Shown above is the observed current at F/C #2 for each m/q value as the analysing magnet current was increased (o) and then decreased(•).
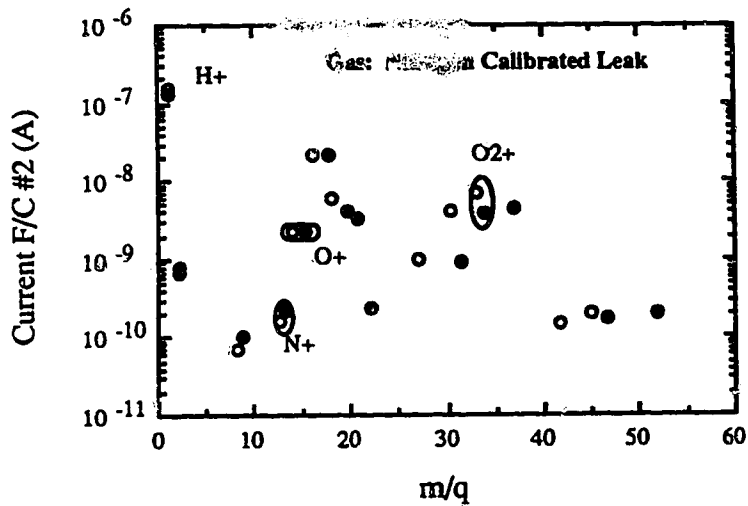
Fig. 5-5b Shown above is the observed current at F/C #2 for each m/q value as the analysing magnet current was increased (o) and then decreased(•).
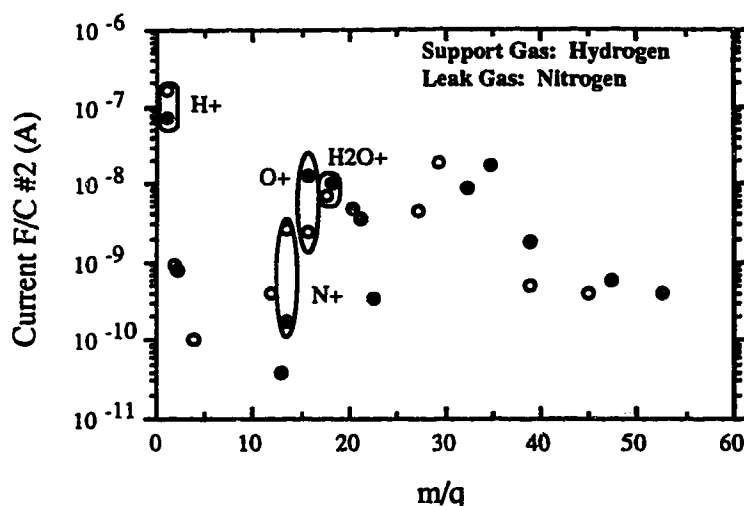
Fig. 5-5c Shown above is the observed current at F/C #2 for each m/q value as the analysing magnet current was increased (o) and then decreased(●).

By observing all three spectra it becomes obvious that there is a vacuum leak which brings the outside atmosphere into the inner quartz tube. By looking only at the increasing magnetic field case and ignoring the current values you can see that all graphs have some of the peaks in nearly the same location. Another factor of interest is the general uniformity of the current extracted. Even though the plasma is formed by three different gas mixtures the currents observed at F/C #2 are all relatively similar as can be see from fig. 5-6. It is also interesting that even if the three values are spread out no one gas mixture is consistently lower than the others.

A final point to be made on the current values is their magnitude. Most of the ion currents are in the nanoampere range. While this is not necessarily bad in itself, when the amount of gas leaking in is considered it becomes apparent that there is a problem. This problem will only get worse as the amount of initial gas decreases ie. in an on-line situation. The most likely cause of this problem is bad transmission.
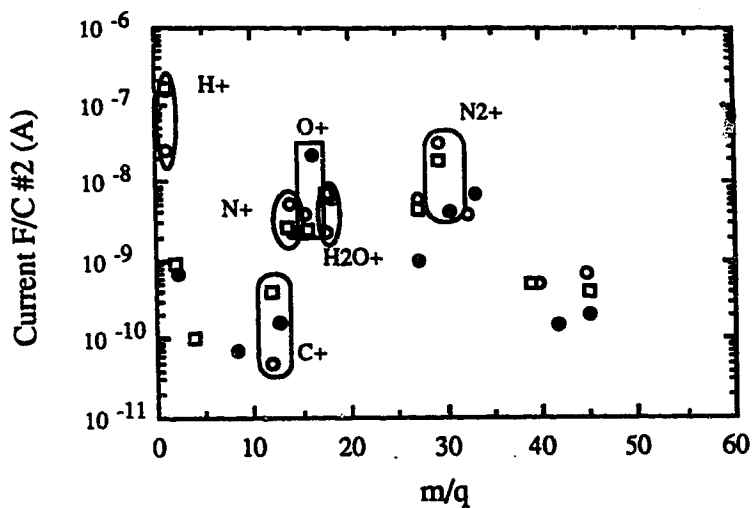
Fig. 5-6 A comparison of the currents in F/C #2 for the three runs on Aug. 29. The data
for leaked atmosphere is shown by (o), for the nitrogen leak alone by (●), and
for the mixture of the nitrogen leak and a hydrogen carrier gas by (□).

After observing the results obtained it was decided that there was no longer any need
to increase and then decrease the magnetic field of the analysing magnet.
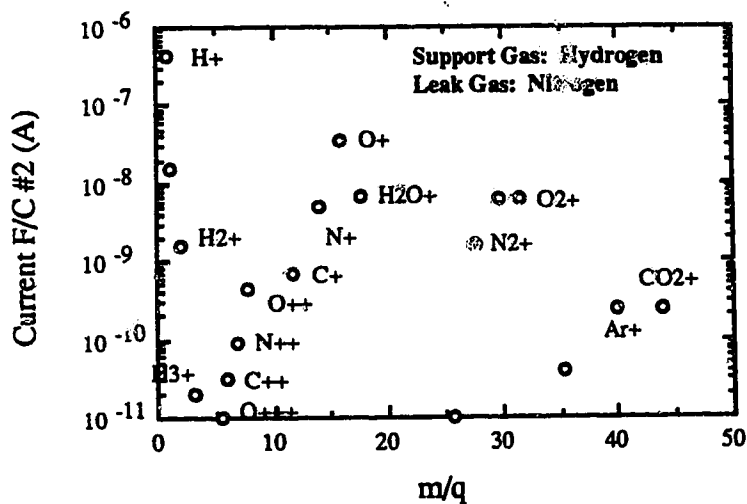
Fig. 5-7 The data collected for the nitrogen leak/hydrogen gas run carried out on Aug.
30, 1988. The current at F/C #2 is shown for the various ion species observed.

The data collected on the final day of running (see fig. 5-7) are the best seen in the run. This test had the same parameters as the third test on the 29th but with the maximum RF power absorbed increased to 113.3 W.

This test shows the first clear indication of multiple charge state production although the currents for these species are very low. The relative intensity of the currents for the +2 ion to the +1 ion unfortunately is not constant and depends on the ion species as shown in table 5-5.

Table 5-5: The relative intensity of the +2 ion beam to the +1 ion beam from the Aug.30 data.

Species	Ratio I^{+2} / I^{+1} (%)
O	0.08
N	1.8
C	4.3

The carbon result is so high simply because the +1 ion beam current is not large. These results mean that the goal of the production of ions predominantly in the +1 state is being accomplished as obviously most (>90%) of the beam exists in the +1 state.

By using the relative abundances of the various ion species in the analysed spectrum (see fig. 5-8) and the current data collected a number of comments can be made.
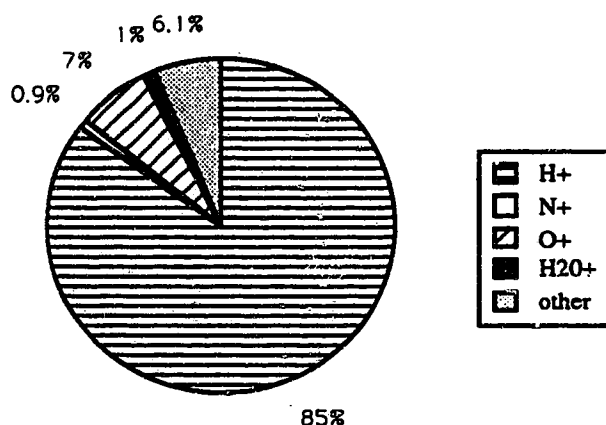
Fig. 5-8 This figure shows the percentage of the total analysed beam for the various ion species observed during the Aug. 30 run.

The first is that the total current comes to only 5.3×10^{-7} A which supports the statement made before that the transmission is very poor as this is only 0.6% of the total extracted beam as measured at F/C #1. As one would expect, the majority of the beam is hydrogen, but strangely enough the next largest constituent is not nitrogen but oxygen. The presence of oxygen clearly indicates a vacuum leak. It, however, still doesn't explain why the amount of nitrogen is so low since air is ~80% nitrogen and air leak should increase the amount of nitrogen in the beam. There are three possibilities to explain this: the first is that the source was not ionizing nitrogen very well, the second that the presence of nitrogen in the plasma enhances the production of oxygen ions at the expense of nitrogen, and the third that the oxygen was not coming from a vacuum leak but from pump oil that had worked its way into the plasma and had been broken up and the products ionized. There is no way to at this time differentiate between explanations.

5.3.3 Data on the Total Current Extracted

The final topic in this chapter is the total current extracted from the source. After each identification run the total current being extracted by the source would be measured with F/C #1. On August 26th, however, it was noticed that even when F/C #1 was retracted a sizable current could still be measured on it. This means that even close to the extraction point (~46 cm from the plasma electrode) the beam had dispersed significantly. Shown in table 5-6 is data which shows the effect of both gas flow and absorbed RF power on the total extracted current.

Table 5-6: A comparison of the extracted current at F/C #1 to gas type, gas flow, and absorbed RF power.

Gas Type	Gas Flow (atm-cc/s)	Net RF Power (W)	Extended Current (μA)	Retracted Current (μA)
hydrogen	1.8×10^{-3}	55.9	42	4.3
leaked atmosphere	3.2×10^{-3}	90.2	48	0.1
nitrogen leak	6.22×10^{-8}	82.5	58	8.4
nitrogen leak and hydrogen	6.22×10^{-8} 6.7×10^{-4}	83.4	44	18
nitrogen leak and hydrogen	6.22×10^{-8} 6.7×10^{-4}	113.3	93	32

Unfortunately, this data is not very illuminating. There does not seem to be any form of predictable dependance of the extracted current to any of the parameters listed. A somewhat more useful test was performed to check the effect of just the RF power on the total current extracted. The results of which can be seen in fig. 5-9. This graph shows surprisingly that the optimum power for maximum extracted beam is quite low, around 30 W.
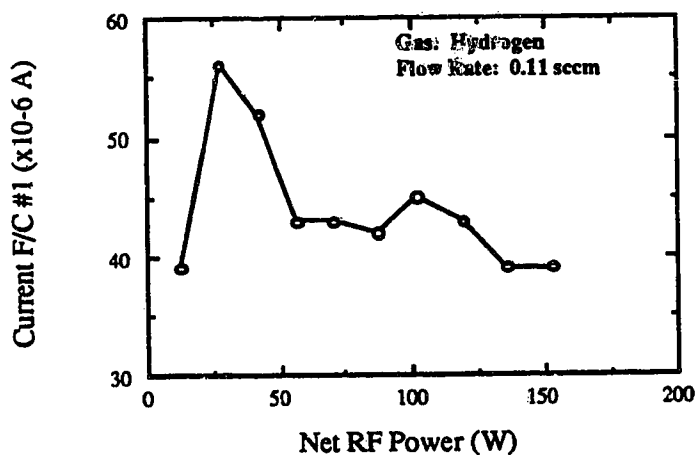
Fig. 5-9 This graph shows the current measured at F/C #1 as a function of the net RF power available at the source.

Even more surprising is the fact that the current goes down with increasing RF power. These two results are contrary to what common sense would predict as well as the results obtained by Bechthold (Bec 85).

5.4 Summary

To summarize what had been accomplished up to this point. The project was well on its way to accomplishing the goals set out for it. A source had been successfully designed, manufactured, and assembled; in record time-- about one year to accomplish all that. The early tests of the source showed promise: firstly, and most importantly it worked. A stable plasma had been formed and could be easily maintained. Secondly, extraction and analysis of an ion beam had been demonstrated. Thirdly, the test bench had been assembled and the main diagnostic elements tested through actual use. Finally, from the data collected it was obvious that most of the ions were produced in the +1 charge state.

One of the main goals was to measure the ionization efficiency of the source but this was not done. The beam transmission was so bad that any kind of accurate determination of the amount of a ion species being extracted was difficult and it was not at all clear what assumptions could be realistically assumed. Since there was a leak somewhere there was no way to know how much nitrogen was leaking into the source, making nitrogen efficiency measurements impossible.

Chapter 6 Primary Source Testing

6.1 Introduction

This chapter will contain the results of the tests done on the source between October, 1988 and January, 1989. The data collected here was used as a basis for the design changes made on the source (see chapter 7) and was additionally intended to be used to evaluate the source's possible performance on-line.

The data will be presented in sections dealing with specific topics rather than in any chronological order. The majority of the data presented will be on neon and argon since it had become apparent that data collected on nitrogen was not easy to separate from the large background. The chapter will begin with a discussion of the total current extracted from the source. The next two sections will deal with the effects of various source parameters on the observed neon and argon currents. Then there will be a discussion on the ionization efficiency of the source. Finally, the results obtained will be summarized and compared to other operating sources.

Before beginning the first section a brief note on the changes in the source is necessary. The changes made to the off-line test system as a whole were explained in chapter 4. In the source the puller electrode was changed from a 30° cone to the Pierce geometry 67.5° cone. In addition, the puller hole diameter was reduced from 10 mm to 3 mm (compare fig. 3-11 to 4-4 to see changes). The changes had the immediate effect of reducing the beam size. This could be verified by looking at the current on F/C #1 when it was extended and then when it had been retracted (see table 6-1). This reduction in initial beam size contributes to an increased transmission in the rest of the off-line system.

Table 6-1: Comparison of the current on F/C #1 extended and retracted for both puller electrode configurations.

Puller Electrode configuration	F/C #1 (extended) (μA)	F/C #1 (retracted) (μA)
old	93	32
new	50	0.007

6.2 Total Beam Extracted from the Source

The total extracted current from the source measured at F/C #1 is useful in a number of ways. It is by far the easiest current to measure although it yields little information directly about the efficiency of the source. In the case where only a single gas is being leaked into the source it can at least give a first approximation of the efficiency. Another value in these measurements is that by examining the effects of source parameters on the total extracted current one might also get a clue as to what conditions would be best to optimize the source for a specific ionic species. It turns out, however; that this assumption is very naive.

The first major test on the source was to determine if the source was operating in the space charge limited region or else in the plasma current limited region. If one is plasma limited and the extracted species current is too small there is little that can be done as the current extracted is everything that the source will produce. If one is space charge limited an increase in the electric field in the extraction region will increase the yield. Ideally, the best operating electric field point would be the extraction voltage and electrode separation settings where the space charge current intersects the plasma current.

Data dealing with the variation of the total current with extraction voltage was

collected several times. Fig. 6-1 shows the results for a mixture of argon and hydrogen. At first glance this data seems to follow the Child-Langmuir Law, however; when the current is plotted versus the (extraction voltage)$^{3/2}$ (see fig. 6-2) the curve is not linear.
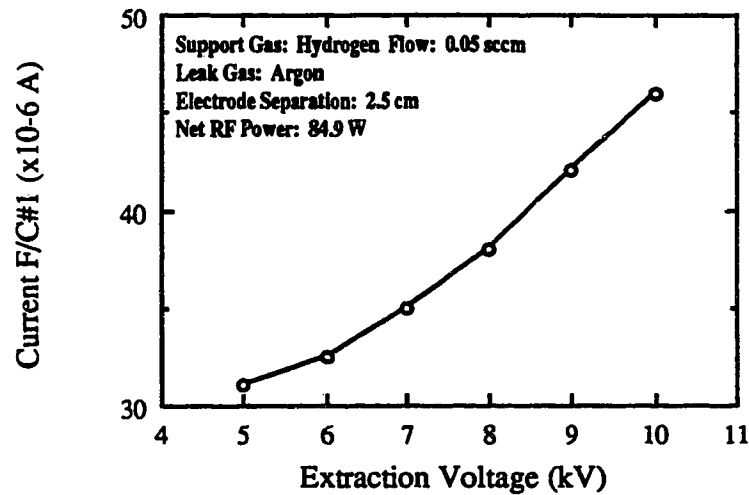
Fig. 6-1 This graph shows the effect of the extraction voltage on the current at F/C #1.
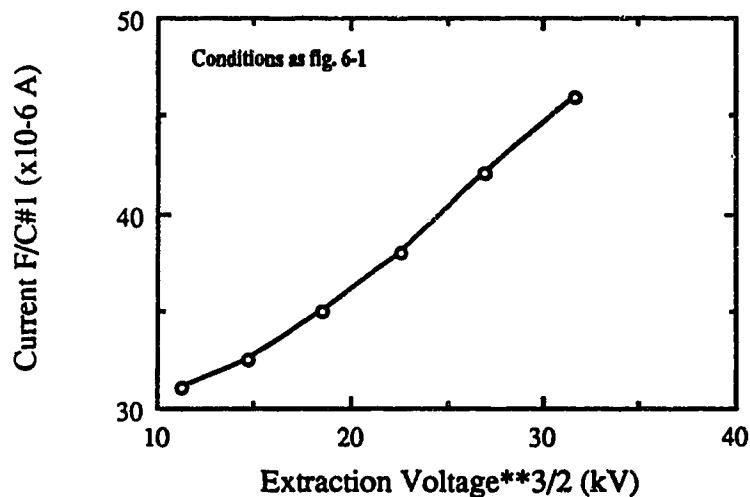
Fig. 6-2 This graph shows the effect of the extraction voltage to the power 3/2 on the current at F/C #1.

If the constant of proportionality, k, in the formula:

$$J = \frac{k}{d^2}\left(\frac{Z}{A}\right)^{1/2} V^{3/2} \qquad (6\text{-}1)$$

where: d is the extraction electrode/plasma electrode gap,

V is the extraction voltage,

Z is the ion charge, and

A is the ion mass,

is calculated it is found that k decreases with increasing extraction voltage. This indicates that even though the source does not operate in the plasma current limited region (the extraction voltage does affect the extracted ion current) neither does it operate in the space charge limited region where the Child-Langmuir Law holds.

These results could be caused by too high a pressure in the source so after the needle valve was added the measurements were repeated in greater detail (see fig. 6-3, 6-4, 6-5). Again the results do not follow the $V^{3/2}$ law. Neither is there a clear indication that the current follows a $1/d^2$ relationship. The constant of proportionality k is varied with V fixed.
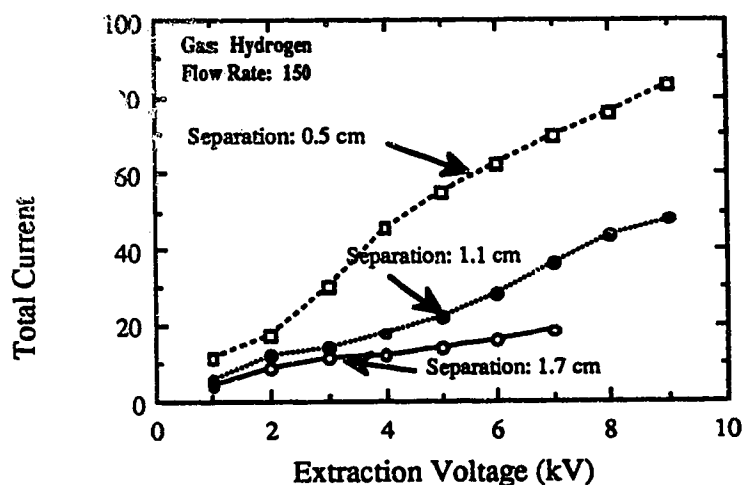
Fig. 6-3 The effect of the extraction voltage and the electrode separation on the current at F/C #1 for hydrogen.
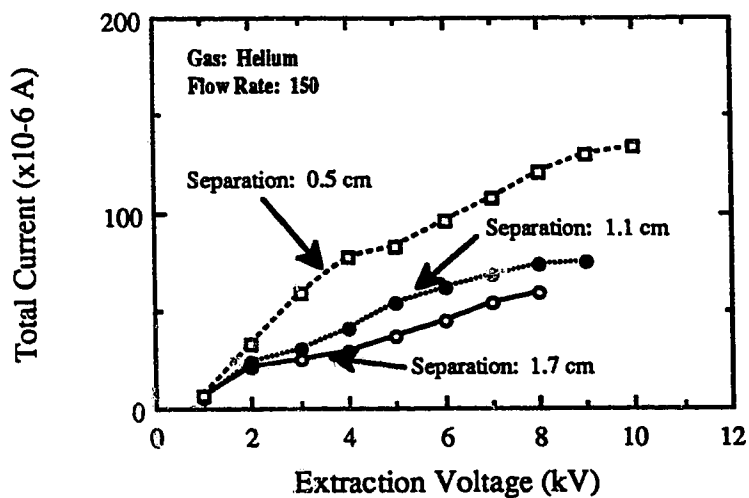
Fig. 6-4 The effect of the extraction voltage and the electrode separation on the current at F/C #1 for helium.
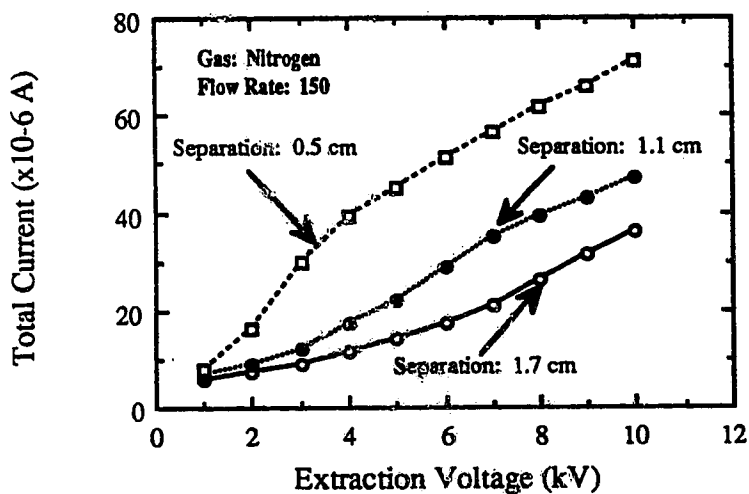
Fig. 6-5 The effect of the extraction voltage and the electrode separation on the current at F/C #1 for nitrogen.

The Child-Langmuir Law also contains a mass term: $(Z/A)^{1/2}$. From this term it is obvious that the current decreases with increasing mass so hydrogen should produce

the largest current and nitrogen the least. The data reveals Helium produces nearly two times the current than hydrogen. Second, the hydrogen was only slightly greater than that for nitrogen.

The situation is not as simple as it seems, however; for although only one gas type is being introduced, the plasma consists of many different types on ions. This obviously has a dramatic effect, especially in the case of nitrogen where there was always a strong N_2^+ current in the analysed beam. Another factor to be considered is that the lighter masses have a larger emittance on exit and more current may be lost on the puller electrode. Another factor which will contribute to the variance from the ideal is the relative ionization efficiency. These numbers would affect the amount of the specific ion available to be extracted. As an example consider the data that has been collected and analysed in this section (see table 6-2).

Table 6-2: The expected current ratios for nitrogen and helium compared to hydrogen taking into account the Child-Langmuir Law and ionization efficiency.

Species	J_{Theory}	Ionization Efficiency $_{(exp)}$	Adjusted Current	Ratio to H^+
H^+	$K(1)^{1/2}$	0.02	0.02 K	1
He^+	$K(1/4)^{1/2}$	0.05	0.025 K	1.25
N^+	$K(1/14)^{1/2}$	0.1	0.027 K	1.35
$N^+ + N_2^+$	$K\{[(1/14)^{1/2} + (1/28)^{1/2}]/2\}$	0.1	0.023 K	1.15

These results do not fit the experimental data well either but it is possible that the constants of proportionality should be K_H, K_{He}, etc. which might improve the agreement. A final explanation for the missing high electric field current is that there could be extraction of the plasma through the pumping ports for the vacuum between the inner and outer quartz tubes which would then be lost to neutralization on the puller electrode. It was noticed during the high voltage tests carried out on the source that

plasma could be pulled out through these holes. This was demonstrated by beam burns on the puller electrode. This additional extraction was possible because the inner quartz tube was not sealed to the plasma electrode.

In all the graphs shown above the maximum voltage shown is the voltage after which breakdown did occur. The strange observation is that at larger gap separation the breakdown occurs at a lower voltage. This would seem to indicate that the problem is caused by secondary electrons emitted from the puller electrode impacting on the Delrin insulator creating a plasma discharge. There was clear evidence of burn marks on the Delrin to support this but they could have been due to heating from the plasma electrode.

In order to examine more fully the effects of various source parameters on the total
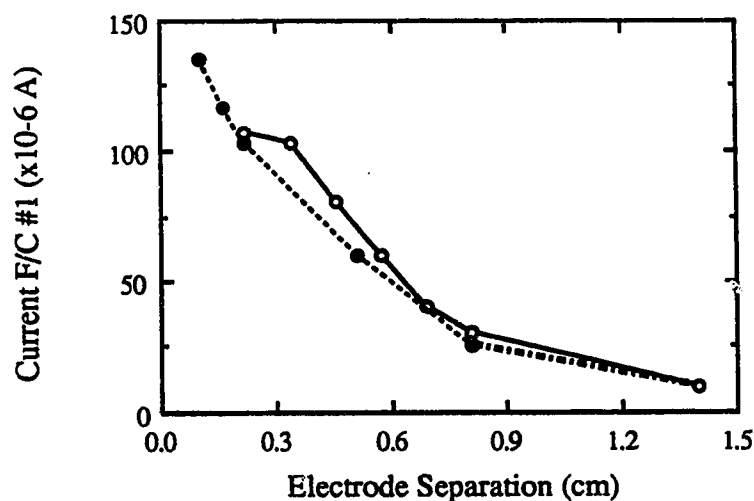
Fig. 6-6 The effect on the current at F/C #1 of the electrode separation for 5 kV extraction voltage. (○) indicates observations made while increasing the separation, (●) indicates observations made while decreasing the separation.

current at voltages of 5 and 10 kV the effect of the position of the Extraction Electrode,

the electronic flow controller setting, and the net RF power were measured. Fig. 6-6 and 6-7 show the effect of moving the extraction electrode for 5 and 10 kV respectively. The graphs show a clear $1/d^2$ variation with the 5 kV results being somewhat more pronounced.
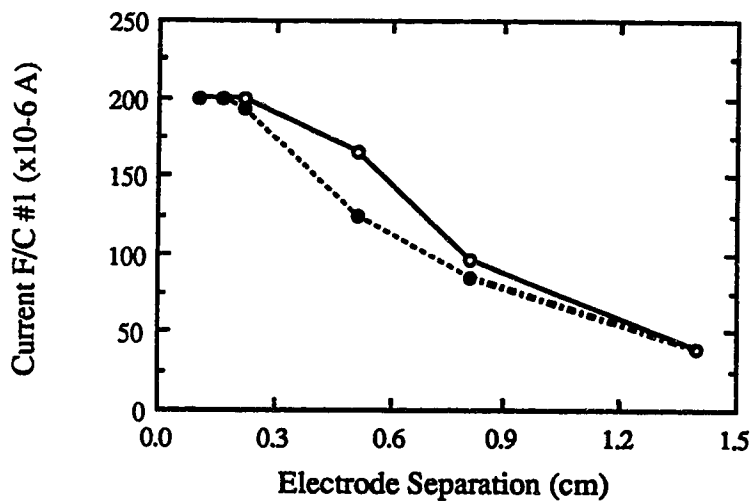
Fig. 6-7 The effect on the current at F/C #1 of the electrode separation for 10 kV extraction voltage. (o) indicates observations made while increasing the separation, (•) indicates observations made while decreasing the separation.

The results for the gas flow were unfortunately not as clear. Fig. 6-8 shows the data for 5 kV. A remarkable discontinuity between increasing and decreasing the gas flow is seen. There is also the abrupt current change in the case of decreasing gas flow. This is due to the *memory* of the source. As the gas flow into the source decreases it takes some time for this to reduce the pressure in the source which is what is being indirectly measured. The jump discontinuity is probably due to the pressure in the source finally catching up with setting on the flow controller.
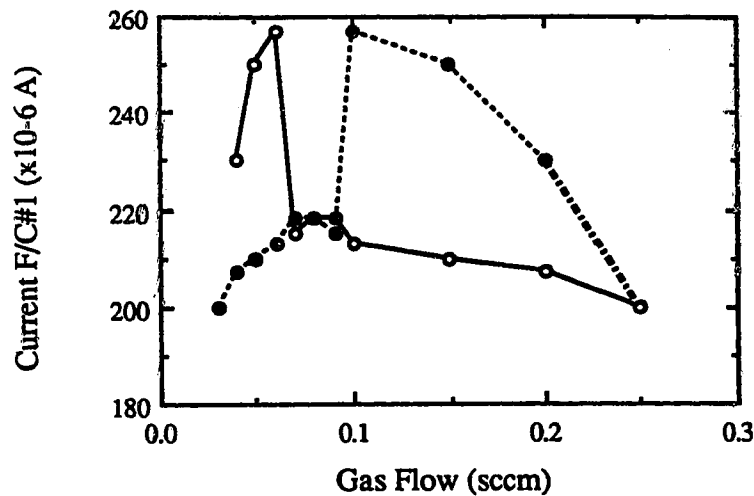
Fig. 6-8 The effect on the current at F/C #1 of the gas flow rate for 5 kV extraction voltage. (○) indicates observations made while increasing the gas flow, (●) indicates observations made while decreasing the gas flow.

Fig. 6-9 shows the data for 10 kV. Here is seen a somewhat different picture. Although, the current decreases as the gas flow increases as it did in the 5 kV case there is a definite hysteresis in the current as the gas flow is then decreased. There is a question about whether this increased current is temporary or permanent. Since each measurement was taken at approximately five minute intervals insufficient time might have been given to allow the source to achieve steady state operation after each change in the gas flow setting. If this was in fact a permanent increase then it should be possible to get improved results by increasing and then decreasing the gas flow.
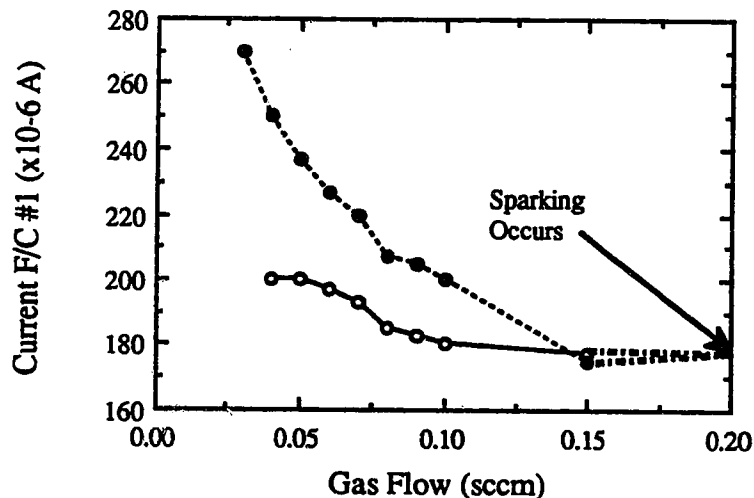
Fig. 6-9 The effect on the current at F/C #1 of the gas flow rate for 10 kV extraction voltage. (o) indicates observations made while increasing the gas flow, (●) indicates observations made while decreasing the gas flow.

The final results obtained had to do with the effect of the net RF power applied to the source. In both cases the data show saturation of the current at low RF power. This is more pronounced in the 5 kV case (fig. 6-10) as at 10 kV (fig. 6-11) it is still possible that the current might continue to increase. However, even in the 10 kV case it is obvious that the current in curving towards a plateau. These results are dramatically different from what was found by the Karlsruhe (Bec 85) group which had seen the current increasing with RF power until a maximum was reached at ~1500 Watts.
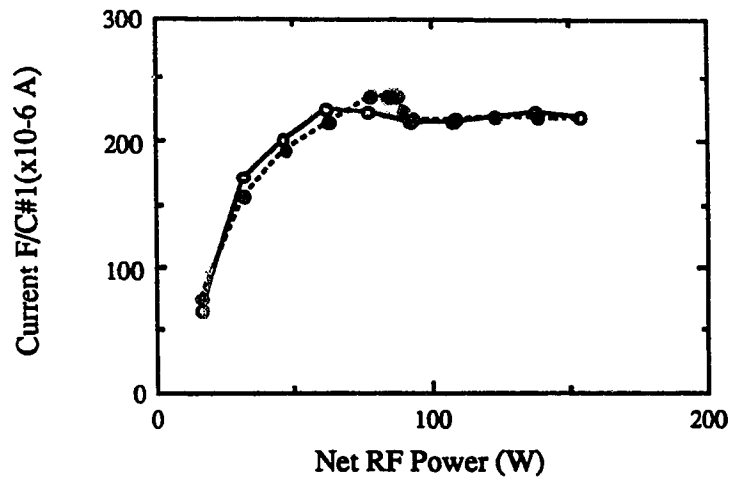
Fig. 6-10   The effect on the current at F/C #1 of the net RF power for 5 kV extraction voltage. (○) indicates observations made while increasing the RF power, (●) indicates observations made while decreasing the RF power.
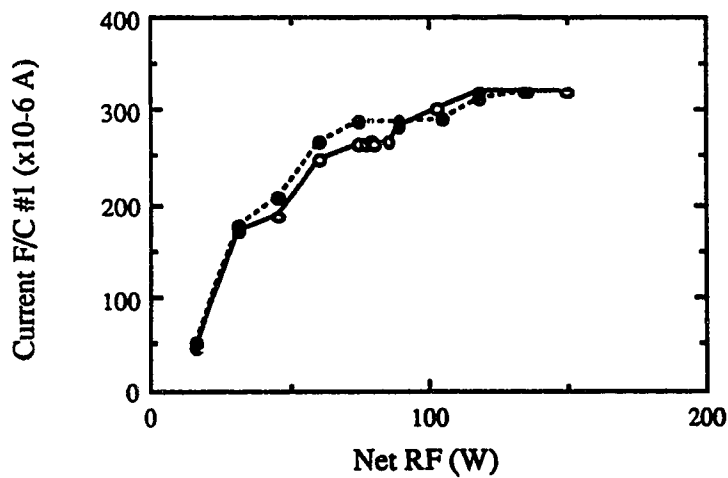
Fig. 6-11   The effect on the current at F/C #1 of the net RF power for 10 kV extraction voltage. (○) indicates observations made while increasing the RF power, (●) indicates observations made while decreasing the RF power.

6.3 Ion Current Measurements

This section will examine the data collected on specific ion currents as measured at F/C #2 instead of looking at the total current extracted from the source. In this section the data collected before the needle valve was installed will be presented. Only the results for neon and argon will be presented since it proved impossible to collect data for nitrogen due to the residual gas in the inner quartz tube. The effect of RF power and extraction electrode position for 5 kV extraction voltage and each of the three possible carrier gases (H_2, He, N_2) will be examined for each of the leak gases of interest.

Let us begin by examining the results for neon. The data for the effect of the position of the Extraction Electrode shows tha: there remains no evidence of the $1/d^2$ effect; indeed all three support gases (fig. 6-12 for H_2, fig. 6-13 for He, and fig. 6-14 for N_2) reveal a marked peak which is not at the smallest gap but in general at some particular separation. At this time the rather large effect of the support gas becomes apparent. Helium yields the best
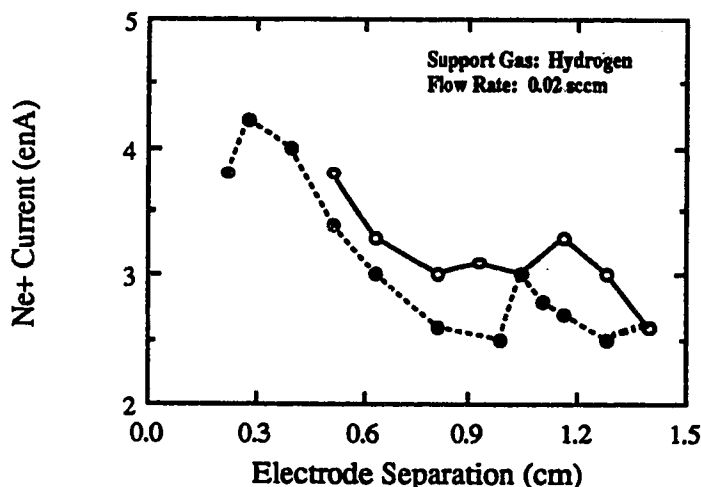
Fig. 6-12 The effect on the Neon current of the electrode separation for hydrogen support gas. (○) indicates observations made while increasing the separation, (●) indicates observations made while decreasing separation.
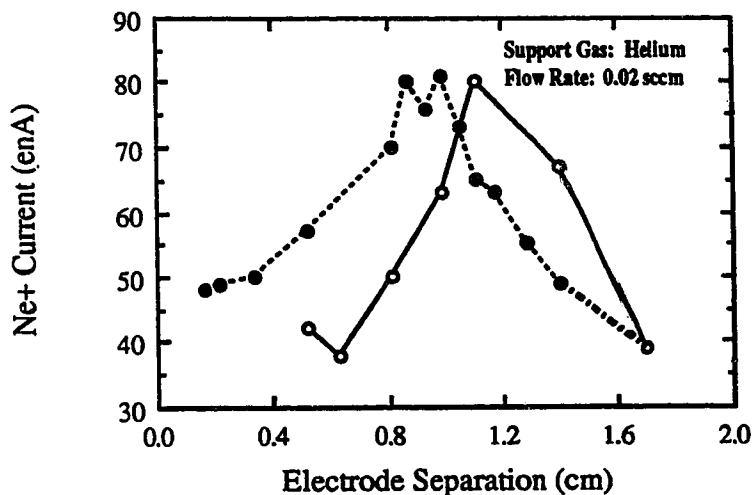
Fig. 6-13 The effect on the Neon current of the electrode separation for helium support gas. (○) indicates observations made while increasing the separation, (●) indicates observations made while decreasing separation.

results giving about ten times the current of hydrogen and about fifty times that of nitrogen.
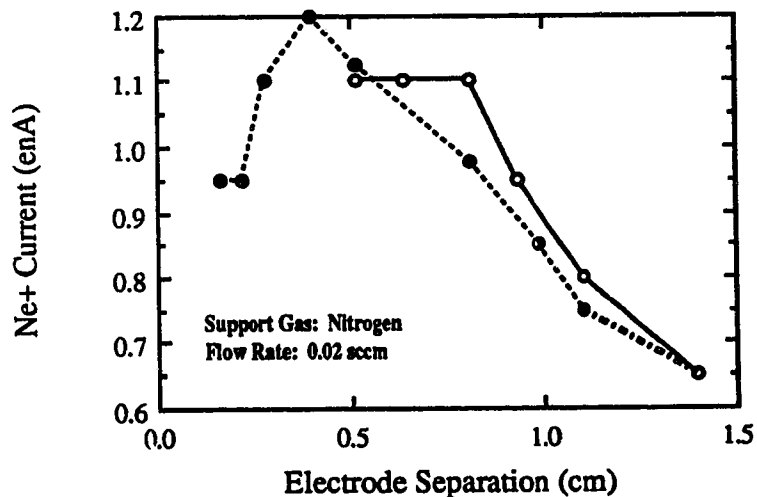
Fig. 6-14 The effect on the Neon current of the electrode separation for nitrogen support gas. (○) indicates observations made while increasing the separation, (●) indicates observations made while decreasing separation.

The data for the effect of the net RF power supplied to the source is also interesting (see fig. 6-15, 6-16, 6-17). The Karlsruhe results indicated that the highest ion current should occur at a high RF power. There was no evidence of this effect in the source data collected. All three support gases give similarly shaped curves which although increasing at the high~ ~~wer levels show clear indications of leveling off. This then looks like the resul'   ~ total current which showed a saturation effect at the mid-range RF power lev~.   In the case of neon, however; the saturation begins at near the maximum power available from the amplifier.
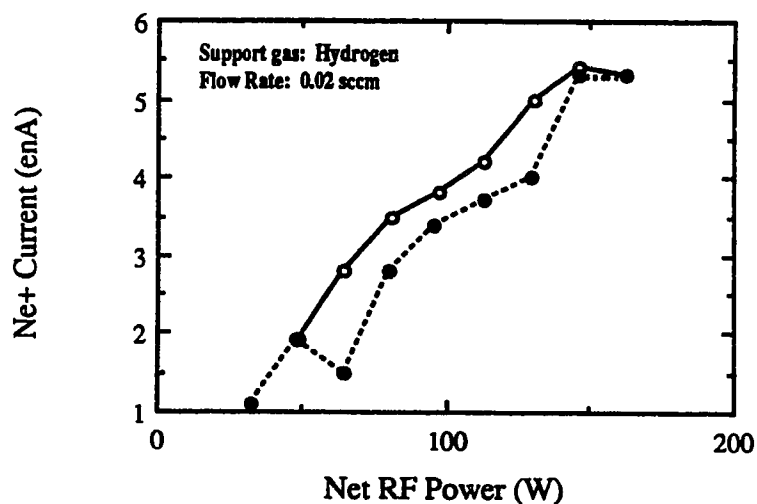
Fig. 6-15 The effect on the Neon current of the net RF power for hydrogen
support gas. (o) indicates observations made while increasing the RF
power, (●) indicates observations made while decreasing the RF power.
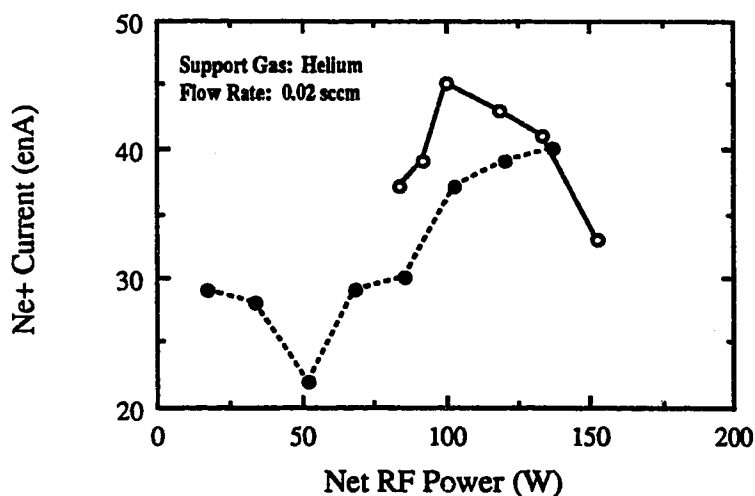
Fig. 6-16 The effect on the Neon current of the net RF power for helium support gas. (○) indicates observations made while increasing the RF power, (●) indicates observations made while decreasing the RF power.
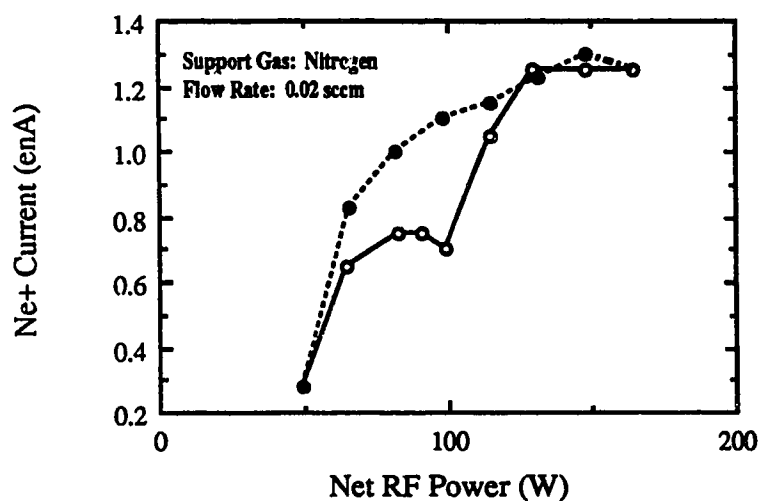
Fig. 6-17 The effect on the Neon current of the net RF power for nitrogen support gas. (○) indicates observations made while increasing the RF power, (●) indicates observations made while decreasing the RF power.

We now turn our attention to the data for argon and begin by examining the effect of the position of the extraction electrode on the current (see figs. 6-18, 6-19, 6-20). Again there is no evidence for the existence of a $1/d^2$ effect in the current which has its peak located at an intermediate point. The effect of the type of support gas used with argon is not nearly so dramatic but the order is the same as for neon. Helium produces the most current, hydrogen the next most, and nitrogen the least.
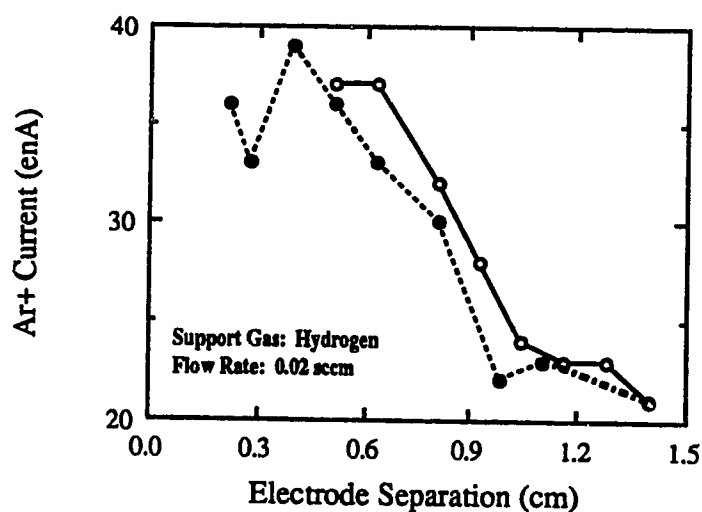
Fig. 6-18 The effect on the Argon current of the electrode separation for hydrogen support gas. (o) indicates observations made while increasing the separation, (●) indicates observations made while decreasing the separation.
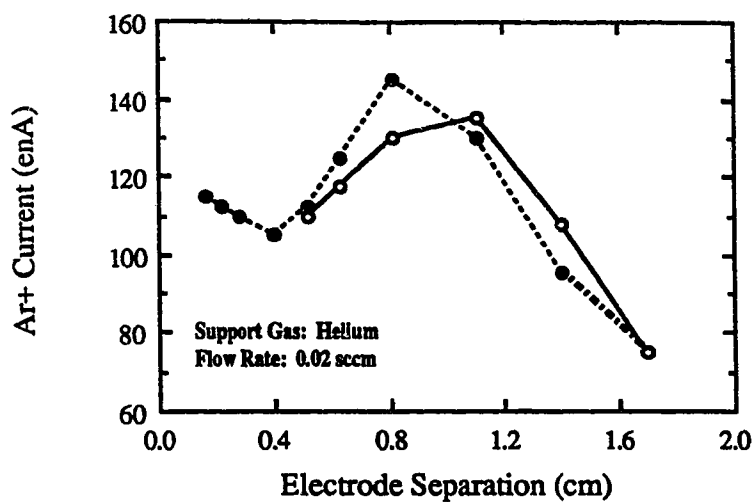
Fig. 6-19 The effect on the Argon current of the electrode separation for helium
support gas. (o) indicates observations made while increasing the
separation, (•) indicates observations made while decreasing the separation.
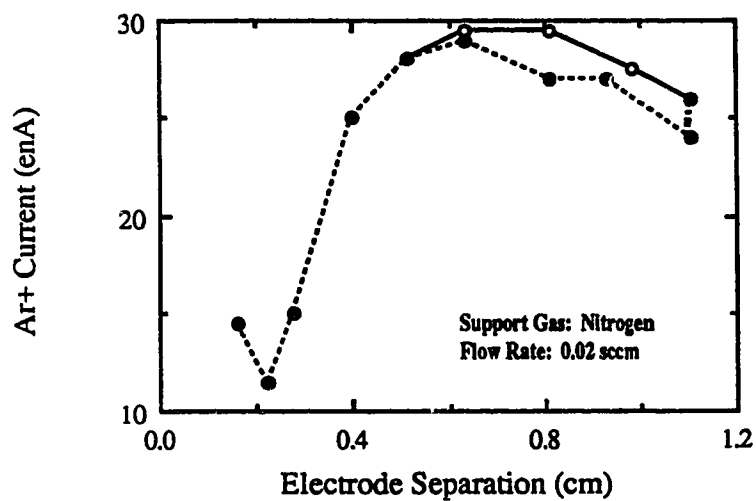
Fig. 6-20 The effect on the Argon current of the electrode separation for nitrogen
support gas. (o) indicates observations made while increasing the
separation, (•) indicates observations made while decreasing the separation.

The RF power data is interesting (see figs. 6-21, 6-22, 6-23). These graphs show

even more clearly that the current saturated at some intermediate (~100 W) level. The

oscillation visible for the nitrogen carrier gas data in fig. 6-23 is probably due to

improper tuning of the magnetic field.
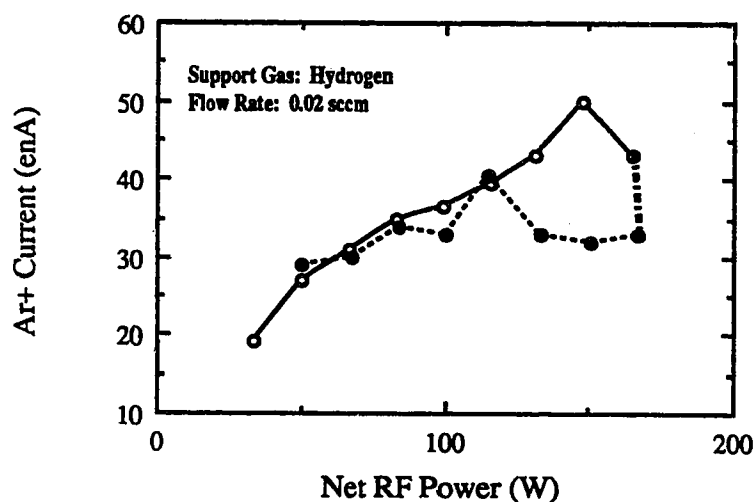
Fig. 6-21 The effect on the Argon current of the net RF power for hydrogen support
gas. (o) indicates observations made while increasing the RF power, (●)
indicates observations made while decreasing the RF power.
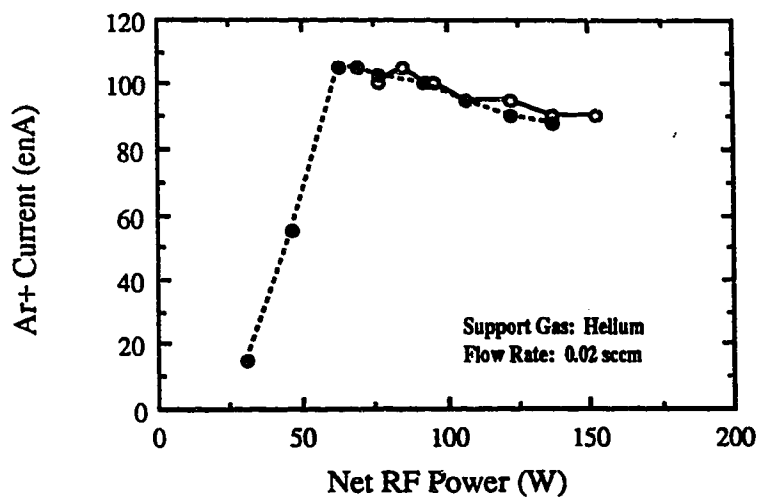
Fig. 6-22 The effect on the Argon current of the net RF power for helium support gas. (○) indicates observations made while increasing the RF power, (●) indicates observations made while decreasing the RF power.
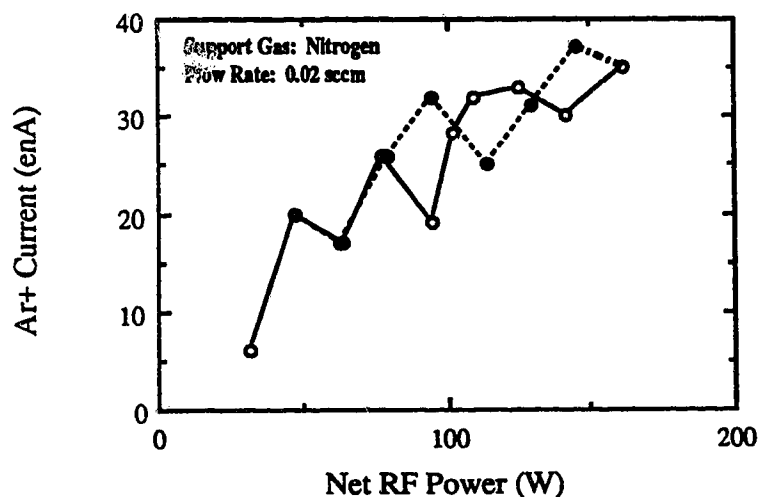
Fig. 6-23 The effect on the Argon current of the net RF power for nitrogen support gas. (○) indicates observations made while increasing the RF power, (●) indicates observations made while decreasing the RF power.

The question of the effect of the support gas on the ion current produced will now be examined. In this case there will be data on nitrogen as well since the goal here is merely to see which support gas gives the best results. The data for Argon are found in fig. 6-24. This graph shows that the maximum current is obtained by running with both the argon and nitrogen leak open. The next best results are obtained without the addition of a support gas. The other support gases follow the order determined before but it is interesting to note that the current increases with lower support gas flow.
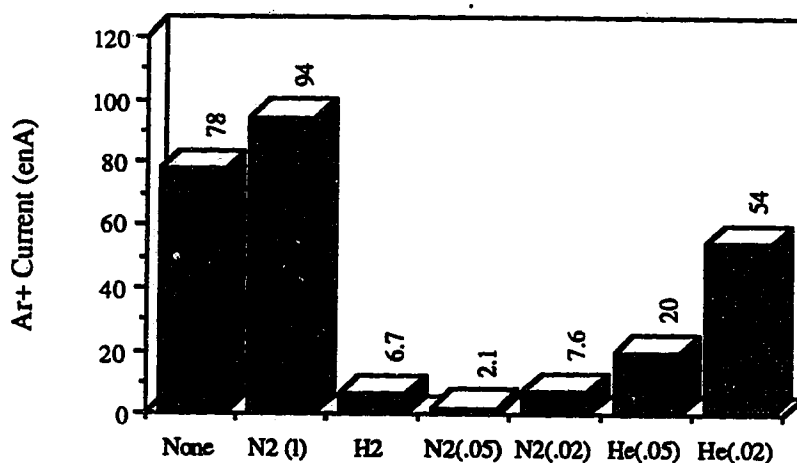
Fig. 6-24 The effect of support gas type on Argon current. Number in brackets indicates flow rate in sccm, 1 indicates calibrated leak.

The data for neon is shown in fig. 6-25. The results for neon are similar to those obtained for argon although the observed current is much lower.
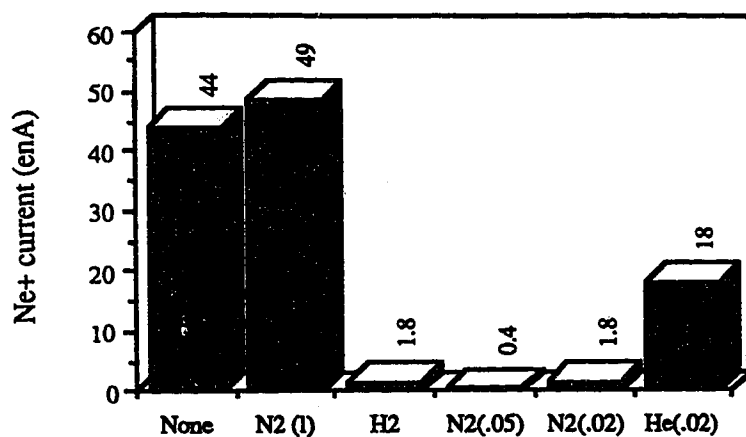
Fig. 6-25 The effect of support gas type on Neon current. Number in brackets indicates flow rate in sccm, 1 indicates calibrated leak.

The real surprise is the data obtained for nitrogen shown in fig. 6-26. There we see that the results for no support gas are the lowest. The other important observations to note are that nitrogen seems to like a high gas flow and that helium gives the worst results. This is a complete reversal of the results for neon and argon.
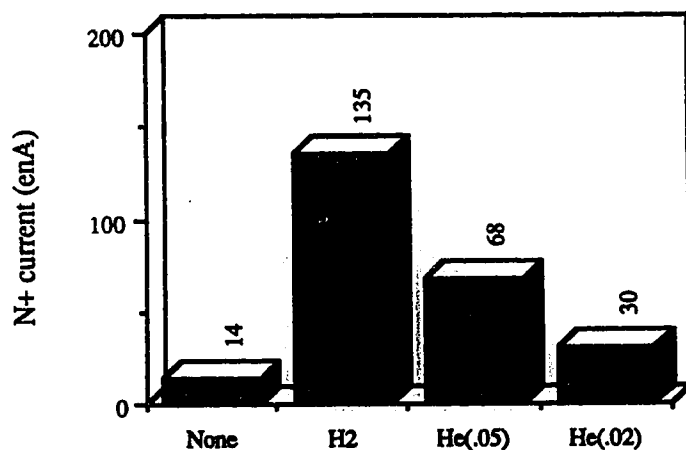
Fig. 6-26 The effect of support gas type on Nitrogen current. Number in brackets indicates flow rate in sccm.

The results for neon and argon are easily comprehensible. It is generally accepted that an ECRIS should be operated at the lowest possible pressure to reduce the negative effects of charge exchange. Of course high-efficiency ECRIS operate at much higher pressures than do high-charge-state ECRIS so low pressure is purely relative but source pressure should be in the 10^{-4} Torr region. Since a low gas flow means a lower pressure in the source it is not surprising that a lower gas flow results in a higher current.

The reason helium seems better than either nitrogen or hydrogen could be the fact that helium has a significantly higher first ionization energy (25 eV) than either nitrogen (15 eV) or hydrogen (12 eV). The high ionization potential means that only rarely will a collision between helium and the leak gas result in the argon or neon atom gaining an electron from the helium. In fact, ionized helium is far more likely to remove an electron from the leak gas to fill its own electron vacancy. The reason why hydrogen is the best support for nitrogen may also be explained in a similar manner. It is relatively easy for the source to ionize hydrogen and as there is little difference in the ionization potential between hydrogen and nitrogen it would be very easy during a collision between a neutral nitrogen atom and a hydrogen ion for an electron to be exchanged. Unfortunately, this does not explain why nitrogen should like high gas flow rates unless for higher flow rates the rate of ionizing charge exchange collisions is increased. There could be simpler explanations for this result as well. For example, there might be leaks in the hydrogen carrier gas lines which allow additional nitrogen into the source thus simulating an increased current.

Although the main interest was in the production of +1 ions a post accelerator would be less expensive if a higher charge state (say +2 or +3) could be used. In order to see what the higher charge state production of the source was like a number of runs

with no support gas or with a mixture of a leak gas and the nitrogen leak gas were done. It had been found that the addition of a carrier gas completely swamped the production of high charge state ions reducing the +2 current to ~10% of the +1 and the +3 current to ~1% of the +1 if present at all. Scaling laws (see section 2.4) would indicate that the addition of a small amount of nitrogen should improve the higher argon charge states; it should have little effect on the neon. The results for argon and neon are shown in figs. 6-27 and 6-28 respectively. The results show the expected distribution given the $n_e\tau_i$ product (see section 2.3.5) assumed for a high efficiency source. Most of the ions are in the first three charge states; in both cases, the anomalous peak at $Z = +5$ is due to contamination from oxygen, nitrogen, and carbon ions. Note the expected enhancement due to nitrogen for argon. It also evidently helped neon as well but not as strongly as for argon which is what would be expected.
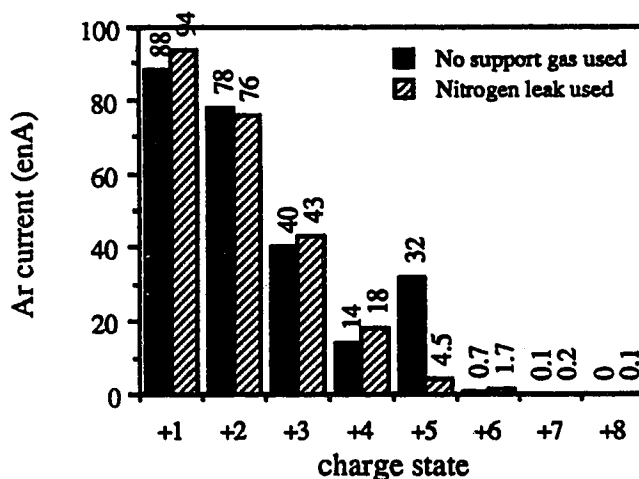
Fig. 6-27 The effect of the nitrogen calibrated leak on Argon charge state distribution.
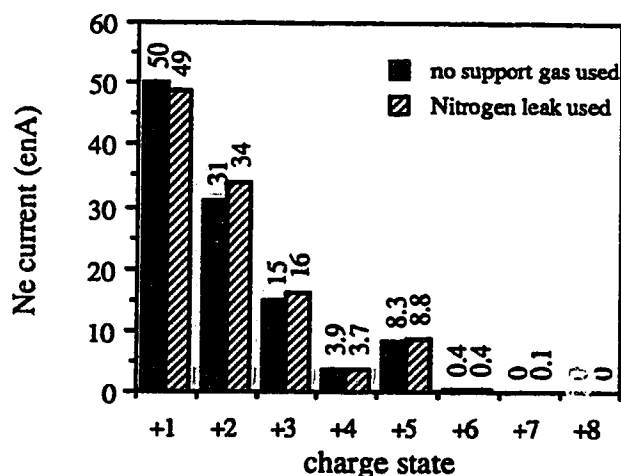
Fig. 6-28 The effect of the nitrogen calibrated leak on Neon charge state distribution.

6.4 Results with the Needle Valve

As the results of the previous section indicated that the source preferred to operate with a low gas flow, and since the electronic controller was at its limit, a Phillips needle valve was added (see section 4.4 for more details). In this section two topics will be covered. The first is the effect of the needle valve on the total current observed at F/C #1. The second will cover how the needle valve effected the specific ion currents obtained from the source.

6.4.1 Total Current Measurements

In this section the data for a series of measurements carried out for argon and neon in combination with the various support gas candidates will be presented. Each graph shows the total current for a specific gas mixture versus needle valve number for two different RF powers.

The results for argon (figs. 6-29 and 6-30) show no real differences for support gas

type, with the main effect due to RF power. Unfortunately, insufficient data was

collected to really see the effect of the needle valve.
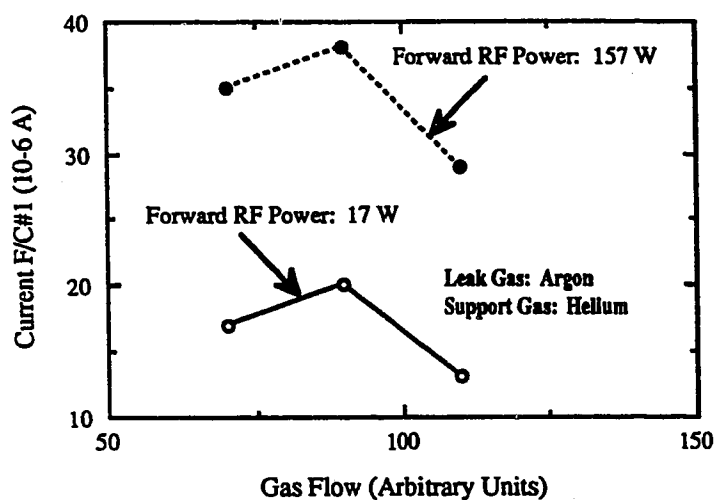
Fig. 6-29 The effect on the current at F/C #1 for helium support gas flow rate at two different RF power levels.
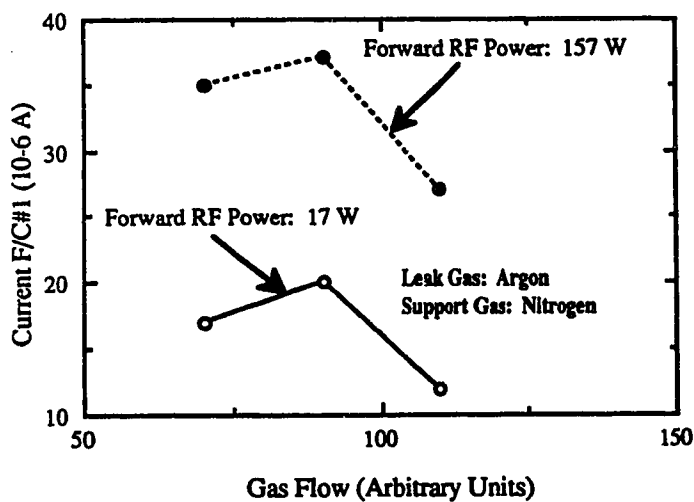
Fig. 6-30 The effect on the current at F/C #1 for nitrogen support gas flow rate at two different RF power levels.

The results for neon (figs. 6-31, 6-32, 6-33) are far more interesting. Here again there is little difference due to the support gas used and again the higher RF power provides for a higher current. The effect of the support gas flow is obvious, there is a general trend towards a higher flow rate providing a lower current. This effect is most dramatic at the higher power levels where the current which is initially ~2x the current of the lower power level, drops to essentially the same value.
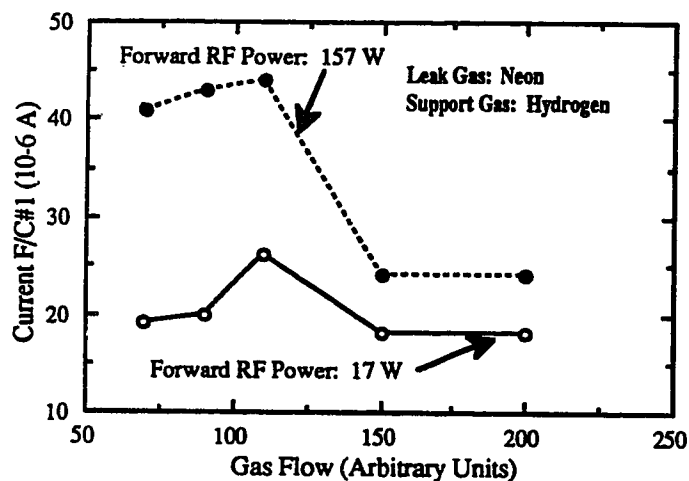
Fig. 6-31 The effect on the current at F/C #1 for hydrogen support gas flow rate at two different RF power levels.
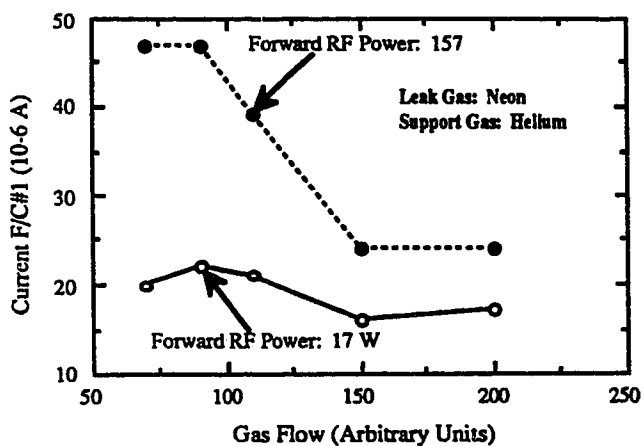
Fig. 6-32 The effect on the current at F/C #1 for hydrogen support gas flow rate at two different RF power levels.
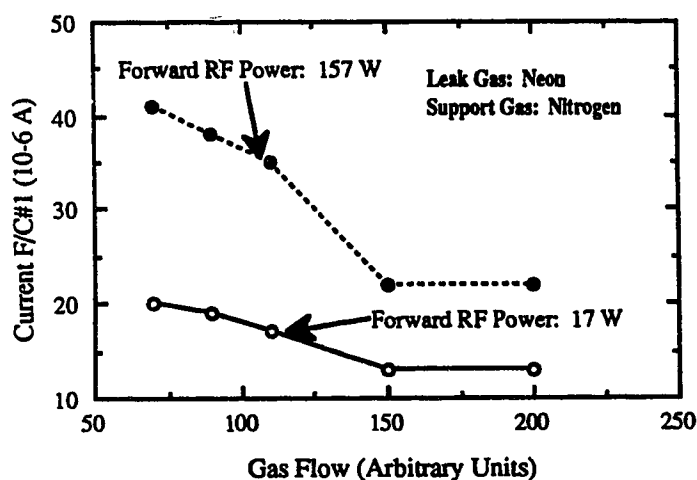
Fig. 6-33 The effect on the current at F/C #1 for hydrogen support gas flow rate at two different RF power levels.

6.4.2 Ion Current Measurements

These measurements basically repeat the measurements done in section 6.3 to

determine the effect of further decreasing the support gas flow rate. Examining the data for neon first (see figs. 6-34, 6-35, 6-36) a number of conclusions can be drawn. The first is that the data seems to fall into three bands. The results for low flow rates (70, 90) show little evidence for any effect due to the type of support gas used and show a saturation of current with the RF power. The exact same results are apparent for high flow rates (150, 200). This indicates that these are probably inappropriate operating regimes to determine the effect of the carrier gas. The low flow rate gives the highest currents but this again is the same as when just operating with the leak alone and no support gas. Now, the intermediate region (flow rate 110) yields the most information. Here there is a definite effect due to carrier gas with hydrogen giving the best results, helium the next best, and nitrogen the worst. In this case hydrogen and helium have been switched in position from the results with the electronic flow controller. Although the current increases with increasing RF it appears to be leveling off in all three cases showing the before mentioned saturation effect.
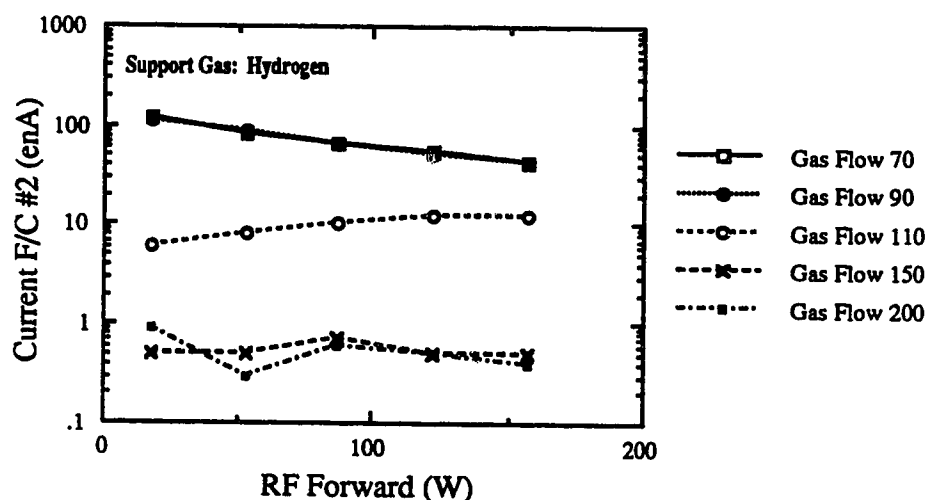
Fig. 6-34 The effect on the Neon current of forward RF power for different hydrogen support gas flow rates.
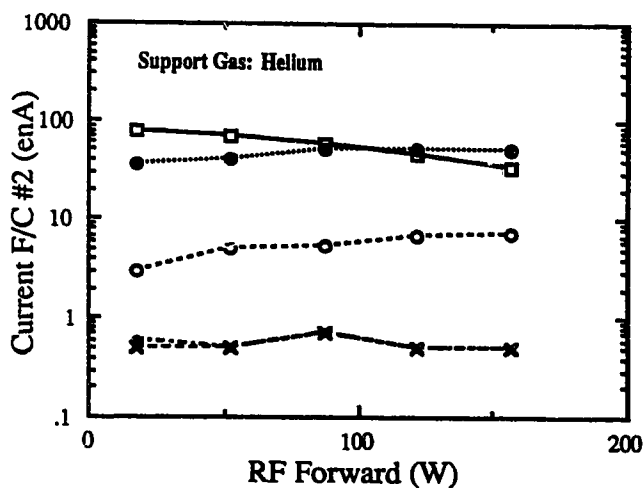
Fig. 6-35 The effect on the Neon current of forward RF power for different helium support gas flow rates. The flow rate key is the same as in fig. 6-34.
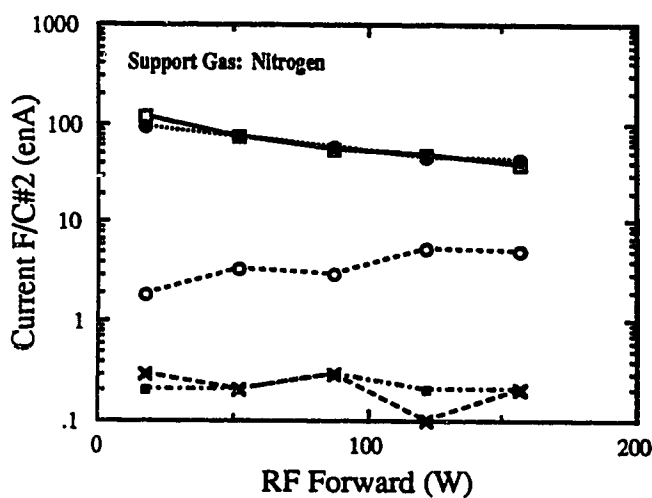
Fig. 6-36 The effect on the Neon current of forward RF power for different nitrogen support gas flow rates. The flow rate key is the same as in fig. 6-34.

The results for argon (see figs. 6-37, 6-38) are not as extensive but they indicate almost no effect for the type of support gas used. There is no evidence that increasing the RF power will have a dramatic effect on the current.

Ar + He Gas Flow
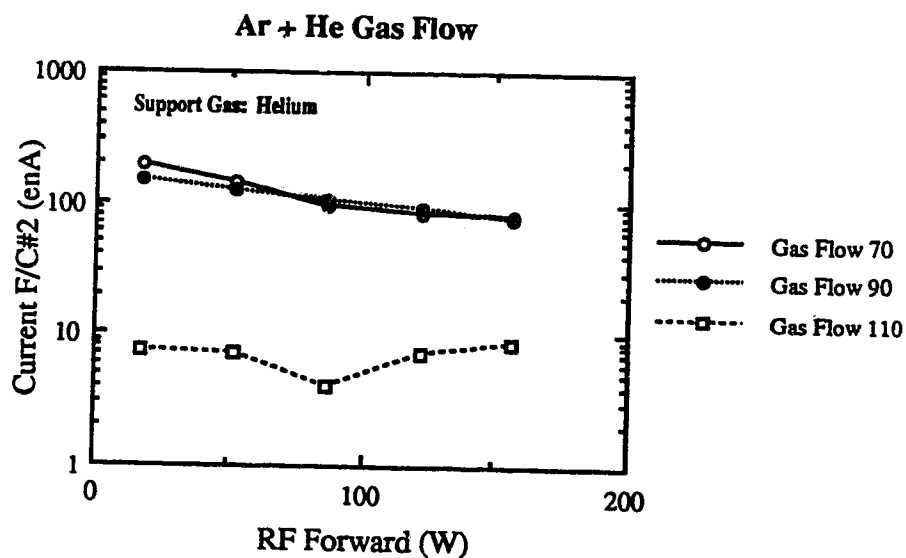
Fig. 6-37 The effect on the Argon current of forward RF power for different helium
support gas flow rates.
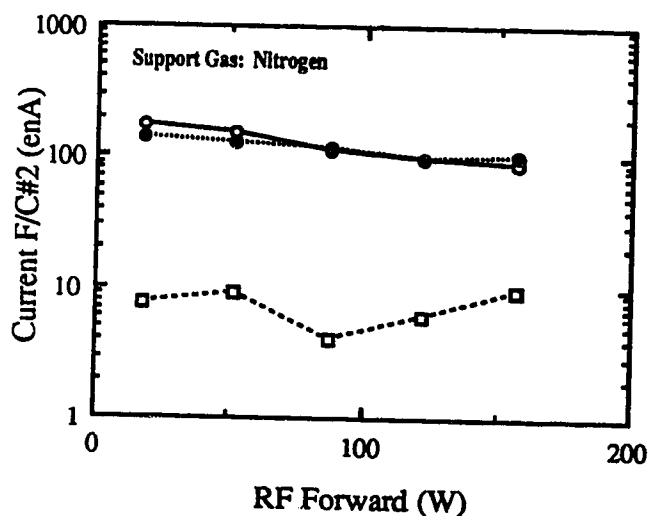
⁚ The effect on the Argon current of forward RF power for different nitrogen
support gas flow rates. The flow rate key is the same as in fig. 6-37.

6.5 Efficiency Measurements

The measurement of the source's ionization efficiency was the primary goal of this project. The task is not straightforward unfortunately. The major difficulty was due to the fact that the transmission of the system was very low (~1%). This meant that if one applies the standard efficiency formula:

$$E_{ff} = \frac{I^+_{(ion)}}{I_{(leak)}} \times \frac{1}{T} \times 100 \% \qquad (6\text{-}2)$$

where: $I^+_{(ion)}$ is the observed ion current,
$I_{(leak)}$ is the expected current for 100% ionization, and
T is the transmission,

there is the possibility of introducing a large error into the efficiency measurement. The transmission was calculated from:

$$T = \frac{\sum I^+_{F/C\#2}}{I^+_{F/C\#1}} \qquad (6\text{-}3)$$

There is, unfortunately, no other way to calculate the efficiency for the support gases. Although, this method could have large errors it should still give an upper limit to the ionization efficiency. The data collected for this method is compiled in table 6-3. These results show that the highest ionization efficiencies occur at the lowest gas flow rates (or the lowest source pressure). The stability of the source also becomes apparent when the consistency of the data for any gas is examined. With only one exception [He (0.05)] all the data has only small variations between observations.

Table 6-3: The ionization efficiency data as determined using eq. 6-2 for various gases.

Species[1]	mean adjusted current[2] (μA)	number of observations	transmission range (%)	ionization efficiency[3] (%)
H	35.8	1	1.2	1
He (0.02)	73.8±4.2	2	1.4-1.9	5±0
He (0.05)	49.8±36.0	3	1.1-1.4	1.5±1.1
N (0.02)	17.8±2.2	3	0.9-1.5	0.6±0.1
N (0.05)	26.0±1.5	2	1.0-1.1	0.4±0.1
Ne	3.0	1	1.2	27
Ne+He (0.02)	2.32±0.13	2	1.2-1.5	21±2
Ne+He (0.05)	0.15±0.00	2	1.1-1.3	1±0
Ar	8.4	1	1.2	41
Ar+He (0.02)	3.46±0.11	2	1.5-1.6	16±1
Ar+He (0.05)	2.16±0.01	2	0.7-1.2	10±0
Ar+N2 (0.02)	0.86	1	0.9	4
Ar+N2 (0.05)	0.19±0.02	2	1.0-1.1	0.9±0.1

[1]the number in brackets is the flow rate in standard cc/minute.

[2]this current has been adjusted for transmission

[3]the error quoted is statistical only. ±0 indicates that both values were identical.

To check these results a second method of determining the ionization efficiency was developed. This method uses the difference in total currents measured for the situation with leak open and the leak closed. To keep the background to a minimum these tests could only be performed in the mornings using the initial plasma that was formed by the leak gas whose efficiency was to be measured. Multiple measurements of the total current for the leak open/closed are recorded after giving the source ~10 minutes to adjust before measuring. This time was deemed sufficient since it had been observed that the leak gas current would dwindle to almost zero in less than 30 seconds after the valve was closed. Another factor which had to be taken into account was the

fact that the addition of the leak gas would affect the background plasma and so a mass scan was done for both the leak open and the leak closed situations.

There are a number of assumptions used in this method. The first is that there is a one-to-one correspondence between the relative amounts of a specific ion species in the beam and in the plasma. The second is that changes in the beam current indicate changes in the plasma. The third is that even though an individual ion species current may increase or decrease due to the presence or absence of the leak gas, it is possible to sum the effect on all species (either a net increase or net decrease) and deal with only that net difference. The fourth is that there is the same relative abundances of ion species in the mass spectrum as in the total ion beam extracted from the source.

Although, the procedure is the same for both argon and neon, due to different conditions of the ECR plasma, the details vary so each will be described in individual detail. Table 6-4 contains the argon data which is required for the calculations.

Table 6-4: the data used to calculate the ionization efficiency of argon.

Mean observed current difference (ΔJ): 15.5±0.7 eμA

Observed total argon current at F/C #2: leak open (Ar_o^A): 224.9 enA

leak closed (Ar_c^A): 4.2 enA

Σ background currents leak open (B_o^A): 299.4 enA

Σ background currents leak closed (B_c^A): 280.3 enA

Ratio of Ar^+ current to total argon current: 0.44

Expected ion current for 100% ionization (J_{exp}): 20.7±10% eμA

To calculate the ionization efficiency we define the following ion beam currents:

$$J_o = B_o + Ar_o \tag{6-4}$$

$$J_c = B_c + Ar_c \tag{6-5}$$

where B is the background current, Ar is the argon current, and o and c refer to leak open and leak closed, respectively. The difference ΔJ is then determined

$$\Delta J = J_o - J_c = \left(B_o - B_c\right) + \left(Ar_o - Ar_c\right). \qquad (6\text{-}6)$$

We then assume that: $B_o \propto B_o^A$, $B_c \propto B_c^A$, $Ar_o \propto Ar_o^A$, and $Ar_c \propto Ar_c^A$. Using this we can write:

$$\Delta B = B_o - B_c \quad \propto B_o^A - B_c^A = \Delta B^A \qquad (6\text{-}7)$$

Now $\Delta B^A = 19.1$ enA or expressed in terms of Ar_o^A: $\Delta B^A = 0.08\ Ar_o^A$

$$\therefore \qquad \Delta B^A \propto 0.08\ Ar_o^A \implies \Delta B = 0.08\ Ar_o \qquad (6\text{-}8)$$

For the argon current:

$$\Delta Ar = Ar_o - Ar_c \quad \propto Ar_o^A - Ar_c^A = \Delta Ar^A \qquad (6\text{-}9)$$

$\Delta Ar^A = 220.7$ enA or expressed in terms of Ar_o^A: $\Delta Ar^A = 0.98\ Ar_o^A$

$$\therefore \qquad \Delta Ar^A \propto 0.98\ Ar_o^A \implies \Delta Ar = 0.98\ Ar_o \qquad (6\text{-}10)$$

Combining these equations gives:

$$\Delta J = 0.08\ Ar_o + 0.98\ Ar_o \qquad (6\text{-}11)$$

$$\Delta J = 1.06\ Ar_o \qquad (6\text{-}12)$$

$$\therefore Ar_o = \frac{\Delta J}{1.06} \qquad (6\text{-}13)$$

Now to find out the amount that is in the +1 charge state multiply Ar_o by the percentage of the analysed beam in the +1 charge state which is 44 % for argon. Now using the formula for the efficiency:

$$E_{ff} = \frac{Ar_o \cdot 0.44}{J_{exp}} \times 100\% \qquad (6\text{-}14)$$

substitution of the values for Ar_o and J_{exp} gives and ionization efficiency of 31%.

For the case of neon the required data is given in table 6-5. The procedure to be followed is similar but in the case of neon the background gas behaved in a different

more complicated manner (see fig. 6-39).

Table 6-5: the data required to calculate the ionization efficiency for neon.

Total Current F/C #1 leak open: 40.0 ± 1.1 eμA

Observed total neon current at F/C #2: leak open (Ne_o^A): 83.6 enA

leak closed (Ne_c^A): 2.6 enA

Σ background currents leak open (B_o^A): 417.3 enA

Σ background currents leak closed (B_c^A): 517.3 enA

Ratio of Ne^+ current to total argon current: 0.45

Expected ion current for 100% ionization (J_{exp}): $11.3\pm10\%$ eμA

To calculate the ionization efficiency begin by defining the following ion beam

currents:

$$J_o = Ne_o + B_o \qquad (6\text{-}15)$$

$$J_c = B_c + Ne_c \qquad (6\text{-}16)$$

Then find the difference.

$$\Delta J = J_o - J_c = \left(B_o - B_c \right) + \left(Ne_o - Ne_c \right) \qquad (6\text{-}17)$$

Now assume that: $B_o \propto B_o^A$, $B_c = J_c$, $Ne_o \propto Ne_o^A$, and $Ne_c = Ne_c^A$. Using this we can

write:

$$J_o = B_o + \left(Ne_o - Ne_c \right) \qquad (6\text{-}18)$$

$B_o^A = 417.3$ enA or expressed in terms of Ne_o^A: $B_o^A = 4.99\ Ne_o^A$

$\therefore \qquad B_o^A \propto 4.99\ Ne_o^A \Rightarrow B_o = 4.99\ Ne_o \qquad (6\text{-}19)$

Turning now to the neon current:

$$\Delta Ne = Ne_o - Ne_c \propto Ne_o^A - Ne_c^A = \Delta Ne^A \qquad (6\text{-}20)$$

$\Delta Ne^A = 81.0$ enA or expressed in terms of Ne_o^A: $\Delta Ne^A = 0.97\ Ne_o^A$.

$$\therefore \quad \Delta Ne^A \alpha\, 0.97\, Ne_o^A \Rightarrow \Delta Ne = 0.97\, Ne_o \quad (6\text{-}21)$$

Combining these equations gives:

$$J_o = 4.99\, Ne_o + 0.97\, Ne_o \quad (6\text{-}22)$$

$$J_o = 5.96\, Ne_o \quad (6\text{-}23)$$

$$\therefore Ne_o = \frac{\Delta J}{5.96} \quad (6\text{-}24)$$

Now to find out the amount that is in the +1 charge state multiply Ne_o by the percentage of the analysed beam i n the +1 charge state which is 45 % for neon. Now using the formula for the efficiency:

$$E_{ff} = \frac{Ne_o \bullet 0.45}{J_{exp}} \times 100\% \quad (6\text{-}25)$$

substitution of the values for Ne_o and J_{exp} gives and ionization efficiency of 28 %.
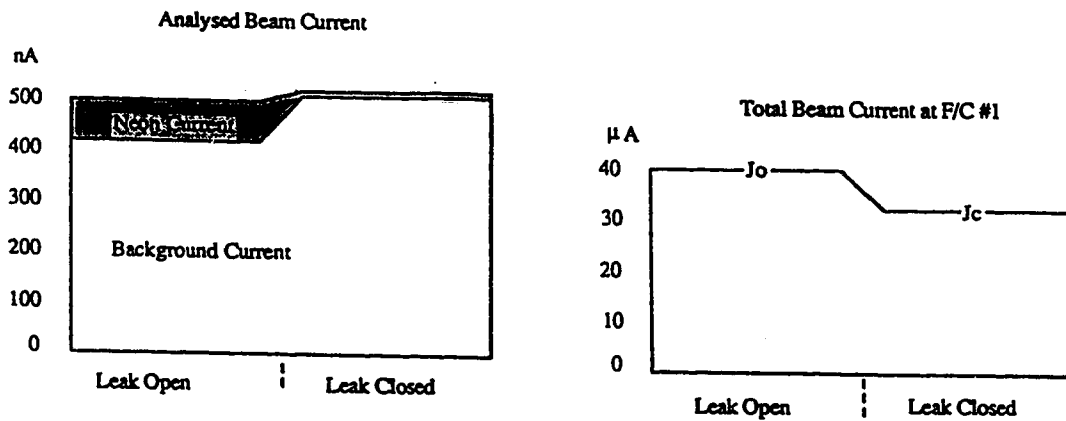
Fig. 6-39: The variation of the analysed and total currents for the neon leak open and closed. These graphs illustrate why the exact procedure followed for argon cannot be used for neon since the analysed total current increased while the total current at F/C #1 decreased this rendered some of the assumptions used invalid.

These numbers are different from the numbers shown in table 6-3. At this time there is no real way to determine which is more indicative of the actual efficiency. Both methods include procedures which could allow errors into the final calculated results. As a way of checking the validity of each method let us examine the errors associated with each method.

So far little has been said about errors for the simple reason that when measuring the current for a particular ion species at F/C #2 or measuring the total current at F/C #1 there was very little error associated with the measurement as the Keithley electrometer. The accuracy was, in general ± 0.5 eμA for F/C #1 and ± 0.05 of the quoted current for F/C #2. For a current of 10^{-7} eA the error would be ± 5 enA. In addition the calibrated leaks were accurate to within ± 10 %. These two considerations would indicate in general a good accuracy but in each ionization efficiency calculation a sum of all observed currents was calculated. To get some idea of the magnitude of these errors let us use as an example the ionization efficiency for argon as calculated by the transmission method and by the total current method.

For the transmission method the maximum error in the current at F/C #2 would be ± 15.8 enA calculated from:

$$\delta\ F/C\ \#2 = a \cdot 5\ enA + b \cdot 0.5\ enA + c \cdot 0.05\ enA \quad (6\text{-}26)$$

where: a = the # of current readings with a magnitude of 10^{-7}
      b = the # of current readings with a magnitude of 10^{-8}
      c = the # of current readings with a magnitude of 10^{-9}

The error for the current at F/C #1 would be 0.5 eμA. These two errors give an adjusted current range of 8.4 ± 0.2 eμA. Folding this in with the 10% error in the calibrated leak gives an ionization efficiency of 41 ± 4%.

Turning now to examine the errors involved in the difference of total currents method we find that the errors for the various elements used in the calculation are

somewhat more complicated. The errors in the various currents are calculated using

equation 6-26 and are given in table 6-6. The errors for ΔAr^A and ΔB^A are also given

in table 6-6 and are calculated from the formula: $\delta \Delta x = \delta x1 + \delta x2$ which gives the

maximum possible error. Now the error ΔAr in terms of the ratio to the current gives

$\Delta Ar = (0.98 \pm 0.04)$ Ar_0 where the error was determined in quadrature. A similar

method for ΔB yields $\Delta B = (0.08 \pm 0.08)$ Ar_0. Now ΔJ is calculated using the difference

in quadrature and yields the result $\Delta J = (1.06 \pm 0.09)$ Ar_0. Calculating the error in Ar_0

by using the quadrature formula gives the value for Ar_0 in table 6-6. Now adjusting

both values for the abundance of the +1 species gives the error in Ar_0^{+1} found in table 6-

6. Finally the efficiency is given by the division of Ar_0^{+1} by J_{exp} which yields a final

error value in the efficiency of $\pm 21\%$ for argon or a value of $31 \pm 6\%$ for the ionization

efficiency. This value is approximately twice the error calculated for the transmission

method.

Table 6-6: Calculated values used to determine the ionization efficiency error for
argon when the total current method is used to calculate the ionization
efficiency.

$$\delta Ar_0^A = 6.6 \text{ enA}$$

$$\delta Ar_c^A = \pm 0.6 \text{ enA}$$

$$\delta B_0^A = \pm 8.9 \text{ enA}$$

$$\delta B_c^A = \pm 10.2 \text{ enA}$$

$$\delta \Delta Ar^A = \pm 7.2 \text{ enA}$$

$$\delta \Delta B^A = \pm 19.1 \text{ enA}$$

$$Ar_0 = 14.6 \pm 1.6 \text{ e}\mu A$$

$$Ar_0^{+1} = 6.4 \pm 0.7 \text{ e}\mu A$$

6.6 Summary and Comparison to Other Groups

The performance of the source by the end of the initial off-line testing can be summarized in table 6-7 which gives the standard operating conditions of the source. A quick summary or the analysed current data for each species of interest (Ar, Ne, N) is also provided in table 6-8. Note that these tables do not include the needle valve data and they include both the data in table 6-3 and other data which was not used.

Table 6-7: a summary of the standard source parameters.

Peak Magnetic Field: ~4000 G
Mirror Ratio: 1.33
Extraction Voltage: 5 kV
RF Frequency: 10 GHz
ECR Field: 3572 G
Max RF Power Available: 200 W
Standard RF Power: 100 W
RF coupling to source: 85 % of incident power
Extraction Hole Diameter: 2 mm
Puller Hole Diameter: 3 mm
Electrode Separation: 0-30 mm
Extraction Current Density: 2.2 mA/cm^2

Table 6-8: Summary of the data collected on the source for the ion species Ar, Ne, and N. The errors quoted are statistical in nature only; in the cases where no error is quoted only one observation was made. The values in [] indicate the results after maximization for transmission. The column for maximum current shows the results when optimizing the source for a specific ion species.

Species	Support Gas (sccm)	Charge State	Current F/C #2 (enA)	Maximum Current (A)
N	none	N^+	14±2	---
		N^{2+}	4.4±1.0	---
		N^{3+}	0.9±0.6	---
		N_2^+	52±34	---
N	H_2	N^+	135±59	---
		N^{2+}	1	---
		N^{3+}	---	---
		N_2^+	333±295	---
N	He (0.05)	N^+	68±2	---
		N^{2+}	1.6±0.1	---
		N_2^+	55±3	---
N	He (0.02)	N^+	30±4	---
		N^{2+}	3.5±0.3	---
		N_2^+	25±1	---
Ne	none	Ne^+	44±7	---
		Ne^{2+}	20±11	---
		Ne^{3+}	8±7	---
Ne	N_2 leak	Ne^+	49	---
		Ne^{2+}	34	---
		Ne^{3+}	16	---
Ne	H_2	Ne^+	1.8±1.7	---
		Ne^{2+}	---	---
		Ne^{3+}	---	---
Ne	N_2 (0.02)	Ne^+	0.4±0.2 [0.6]	1.2×10^{-9}
		Ne^{2+}	---	@ 0.34 cm
		Ne^{3+}	---	@150 W

Ne	He (0.05)	Ne$^+$	1.8±0.1 [2.7±0]	---
		Ne^{2+}	---	---

Table 6-8: Continued.

Species	Support Gas (sccm)	Charge State	Current F/C #2 (enA)	Maximum Current (A)
Ne	N$_2$ (0.02)	Ne^{3+}	---	---
Ne	He (0.02)	Ne$^+$	18±1	7.7×10^{-8}
		Ne^{2+}	2.0±0.5	@ 0.88 cm
		Ne^{3+}	---	@ 138 W
Ar	none	Ar$^+$	78±8	---
		Ar^{2+}	61±12	---
		Ar^{3+}	24±11	---
Ar	N$_2$ leak	Ar$^+$	94	---
		Ar^{2+}	76	---
		Ar^{3+}	43	---
Ar	H$_2$	Ar$^+$	6.7±1.9	---
		Ar^{2+}	---	---
		Ar^{3+}	---	---
Ar	N$_2$ (0.05)	Ar$^+$	2.1±0.2	---
		Ar^{2+}	---	---
		Ar^{3+}	1.8 (?)	---
Ar	N$_2$ (0.02)	Ar$^+$	7.6 [12]	2.3×10^{-8}
		Ar^{2+}	0.2	@ 0.64 cm
		Ar^{3+}	---	@ 95 W
Ar	He (0.05)	Ar$^+$	20±4 [37+1]	---
		Ar^{2+}	1.0±0.2	---
		Ar^{3+}	---	---
Ar	He (0.02)	Ar$^+$	54±1	1.3×10^{-7}
		Ar^{2+}	12±2	@ 1.06 cm
		Ar^{3+}	0.8±0.0	@ 62 W

There are currently five high efficiency ECRIS in the world: the UA/TRIUMF source, the PSI source (Hof 88), the Karlsruhe source (Buc 86), the Louvain-la-neuve

source (Van 89), and the SARA source (Gim 89). Unfortunately there is no published efficiency data for the SARA source. In table 6-9 the ionization efficiencies for the various sources are compared and fig. 6-39 shows the ionization efficiency as a function of species mass for the different sources.

Table 6-9: A comparison of the ionization efficiencies for singly charged ionic species of the different sources. The first set of numbers is for gases used as support gases while the second is for gases from a calibrated leak.

Ionization Efficiency (%)

Species	UA	PSI	KFK	LLN
H+	1	4.5[1]	---[2]	1[2]
He+	5	5.3	---	2
N+	0.6	10.2	---	6
C+	---	1.5[4]	---	---
Xe+	---	---	---	65
C+	---	---	15[5]	2
N+	*	---	26	0.5[3]
N2+	*	---	---	35
O+	---	---	54	4
Ne+	27 or 28	5.8	34	52
Ar+	41 or 31	28.4	---	---
Kr+	---	56.7	---	---
Xe+	---	40.7	58	---

*unable to determine efficiency
[1]errors for carrier gas +20% of the value; errors for leak gas +10% of the value
[2]errors unknown
[3]for N^{13} (radioactive)
[4]out of CH_4
[5]out of CO

This table shows good agreement between the various sources for some ion species while for others the agreement is very poor. There are a number of possible reasons for

the different ionization efficiencies. The most likely has to do with the mean energy of the electrons or how many high energy electrons are available to ionize the more difficult to ionize species. Another factor is the source pressure which is related to both the size of the plasma volume and the pumping available; a source with a lower operating pressure should have a higher ionization efficiency.
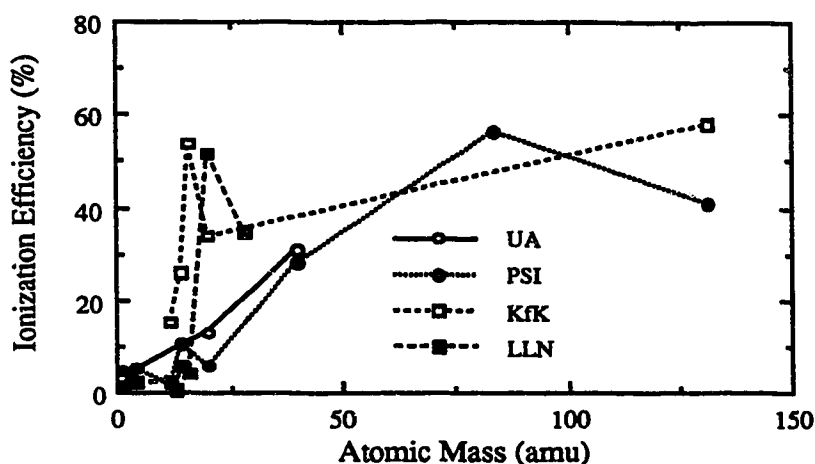
Fig. 6-40 This graph shows the ionization efficiency versus the species mass for the four sources mentioned in table 6-9.

Next, there is the consideration of both the RF power available and the power coupling to the source. There is no clear evidence (except the Karlsruhe results) which indicate high RF powers are required, but to efficiently ionize nitrogen or neon RF power in excess of 100 W seems necessary due to the bond strength/first ionization potential of these species. Also, there might be an effect due to the diameter of the plasma electrode hole. Finally, the sources might have different ion confinement times yielding differing $n_e \tau_i$ values which would affect their ion production rates and hence their efficiency.

The low efficiencies reported for the support gases also agree with the other
groups. Although the results for nitrogen are quite low, this is probably due to
insufficient RF power to break up the nitrogen molecule since it was observed that a
sizable percentage of the total nitrogen current was in the N_2^+ state.

Based on the data gathered up to this point, the decision was made to modify the
source and then re-study it on the testbench before putting it on-line. The modifications
made and the data collected will be presented in chapter 7.

Chapter 7 Final Off-line Test Results

7.1 Introduction

This chapter will be split into three main sections. The first section will include the modifications made to the source in preparation for on-line installation. It will also contain the data collected on the source during the final test bench evaluation which was carried out to see what effect these changes had on the source operation. This section will conclude the off-line efficiency measurements carried out on the source.

The second section will deal exclusively with the emittance measurements done on the source after all other tests were complete. The section will be comprised of two sub-sections. The first will be on the total extracted ion beam emittance measurements. The second will examine the emittance for argon and neon under a variety of source parameters. The final section will be on the on-line facility itself.

7.2.1.1 High Voltage Tests

This topic is included since a number of modifications mentioned in the next section (7.2.1.2) will be based on the observations made here. In the data in section 6.2 it is obvious that the source could not hold more than 10 kV. The specifications (see table 3-1) indicate that the source should operate at least at 20 kV which means that it should operate quietly at 25 kV.

The tests were carried out under a wide variety of source configurations since it was important to find all causes of the arcing. This involved a certain amount of ingenuity since some of the configurations had the coils split apart which meant that a vacuum seal had to be fitted over the upstream delrin flange and the inner quartz tube gas feed. Seven arc causing situations were found and corrected.

114

The first was between the stainless screws which mounted the delrin flanges and the source body. The problem was corrected by replacing the stainless screws with nylon screws. The second cause of arcing was the sharp edge of the ridge on the aluminum *can* which defines the RF cavity. The arc was between here and the edge of the coil compression flange which although shown in the drawings (fig 4-4) as having a sharp edge actually had a radius. This was corrected by smoothing out the ridge on the *can* until it looked something like a beer barrel. In addition, to reduce the effect of a corona field build up, two layers of Kapton foil insulator were wrapped around the RF cavity. This insulator was also wrapped around the waveguide but it should be noted that there was no evidence of arcing between the waveguide and the source body. The third arcing problem is still something of a mystery. It occurred when the magnetic field was on and is thought to be caused by the magnetic field picking up small metal chips and creating a conducting bridge. The inside of the source was wiped clean and this cleared up the problem. However, there was no direct evidence that the problem was, in fact, caused in the manner described above.

The next four problems were not caused by the source itself but by the supporting vacuum system. Two of these problems occurred in the extraction (downstream) system region, and two occurred in the gas inlet (upstream) region. The first problem in the extraction region was due to the the Delrin insulation being able to see the beam and having secondary electrons strike it. The Delrin was deeply pitted and worn away in two or three areas due to this phenomenon. This was cured by putting a copper ring in to cover the exposed insulator. The ring was also in contact with the source body and hence at high tension. The second extraction problem had to do with the vacuum quality in the extraction region. Since the area being pumped through was cluttered with the Einzel Lens/Extraction Electrode assembly the pumping speed was fairly slow allowing a

Penning-type discharge to occur. This could be cured by redesigning the extraction electrode to allow more pumping in the extraction region.

On the gas inlet side the first problem was arcing between the source body and the aluminum end flange. This was cured in two ways. The first was to replace the aluminum flange by a shielded plastic flange, which incidentally had the added bonus of allowing the plasma discharge to be viewed directly. The second was by pumping on the volume with, initially, a 2" diffusion pump, and finally by the addition of a vacuum bypass to box 1. The final arcing problem was a discharge from the source to the gas manifold through the connecting transfer line. This was cured by floating the manifold up to the same high voltage as the source.

7.2.1.2 Source and Off-Line Beamline Modifications

In order to prepare the source for on-line operation a number of modifications were carried out. All of the modifications were to the extraction region. The plasma electrode was redesigned so that it also had a Pierce geometry and it was sealed to the quartz tube. The electrode was made of copper and there was no shielding quartz disk between the copper and the plasma. The extraction hole size was reduced to 1 mm in diameter. The first source modification was to move the extraction aperture back ~0.7 cm to the peak of the magnetic mirror field. The second modification was to chamfer both the new inner quartz tube support insert and the plasma electrode so the tube was now automatically centered with respect to the source as it was pushed forward. The next modification was to the extraction electrode which was changed to reduce its diameter to smaller than the entrance aperture of the insert holding the plasma electrode. This change had the effect of allowing the Einzel Lens/Extraction Electrode to actually come into contact with the plasma electrode or to enable the operator to run the source at very small extraction gaps.

Initially, the extraction electrode hole diameter was reduced to 1 mm but this proved very

hard to align and there were large amounts of the beam striking it so the hole was

increased in diameter to 3 mm. A final modification was to reduce the diameter of the

Einzel lens to concentrate the electric field. The above changes (except for the Einzel

lens change) can be seen by comparing fig. 7-25 to fig. 4-4.

The main changes to the off-line beam line were the removal of the focusing

solenoid and box 2 with its turbo pump (see fig.7-1). This had the effect of dramatically

reducing the total length of the beamline. The x-steering plates were switched to y-

steering since it had been observed that the einzel lens tended to cause the beam to move

upward as the voltage was increased.
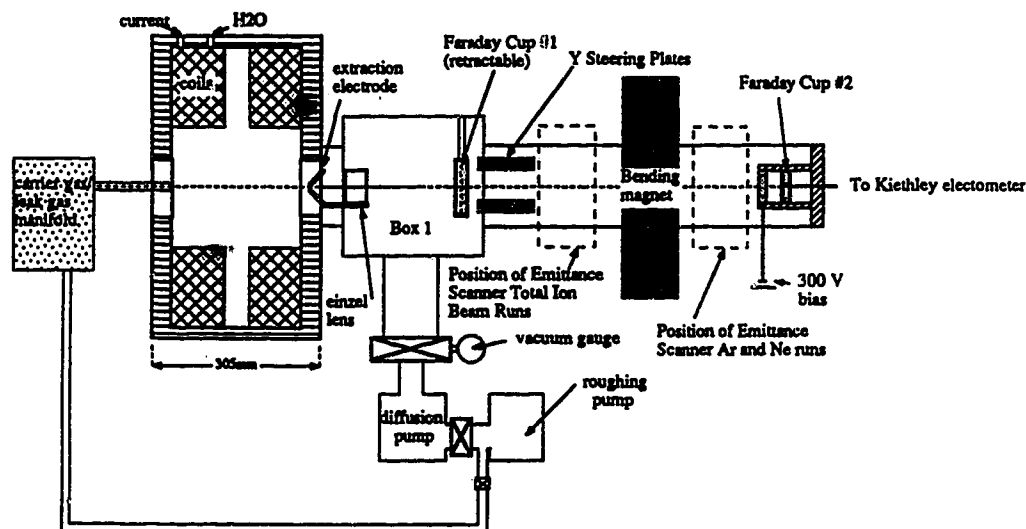
Fig. 7-1 A schematic showing the new off-line beamline. Not shown is a roughing
pump which was connected to box 1 to rough out the vacuum system before
opening the gate valve to the diffusion pump.

Faraday cup #2 was redesigned with two main changes. The first was to mount it in

a standard 4" beam pipe since it had been suspected that some of the beam was being lost

to scraping on the old 1.5" pipe. The second was to redeign the cup bias plate so that the aperture was a slot 10 mm x 30 mm. These two changes resulted in a dramatic increase of the transmission to ~95%.

7.2.2 Ion Current Data

This section will be divided into two main topics. The first will cover the data on the total current extracted from the source. The second will deal with argon and neon currents and how source parameters affected them. Most of this data was collected by T. Pinnington as part of his work as a summer student at TRIUMF.

7.2.2.1 Total Current Extracted from the Source

The total current extracted from the source as a function of extraction electrode voltage was examined first and (see fig. 7-2) showed a clear indication that the source was operating in the plasma current limited region.
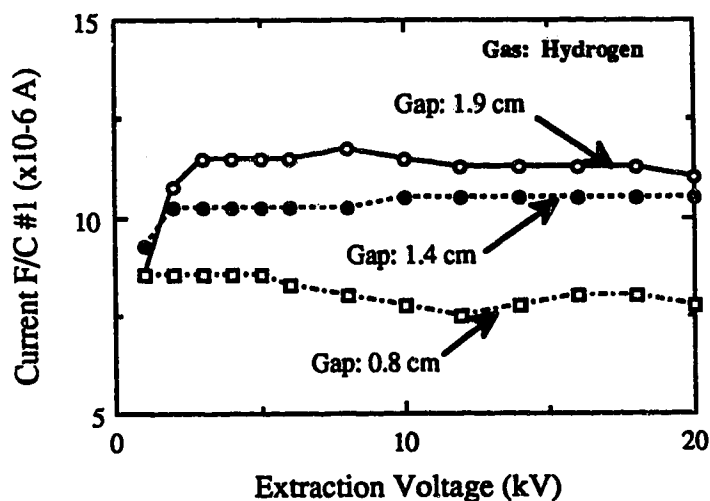
Fig. 7-2 The effect of the extraction voltage and electrode gap on the current at F/C #1.

It is also clear that operating at a small gap separation does not increase the current. This is probably due to excessive current striking the puller electrode.

In another example (see fig. 7-3) the evidence is not quite so clear cut but the levelling off of the current is still clearly visible. This is an obvious change from previous source behavior.
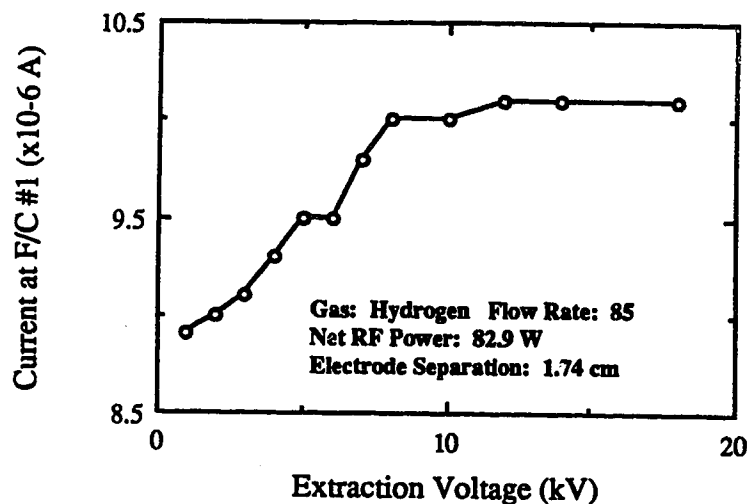
Fig. 7-3 This graph shows the effect of extraction voltage on current at F/C #1.

The effect of the flow controller for two different RF powers is shown in fig. 7-4. Both curves show the same behavior of an increase just before the current drops off. For the higher level this effect occurs at a lower flow rate. This would indicate that the absorption of the RF power is coupled to the source pressure. At higher RF powers the source is therefore more sensitive to changes in flow rate which may mean that operating at a lower RF power is preferable to eliminate the necessity of carefully fine tuning the source.
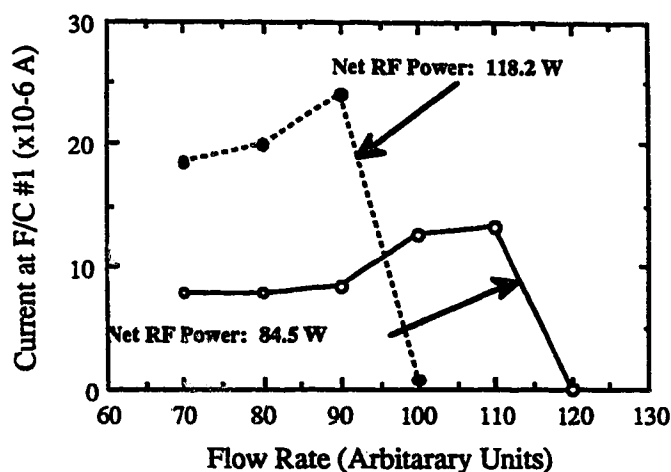
Fig. 7-4 This graph shows the effect of the hydrogen gas flow rate on the current at F/C #1 for two different net RF power levels at 5 kV extraction voltage.

The effect of the RF power alone on the source is shown in fig. 7-5. This graph is similar to the graphs of chapter 6 (see for example 6-10, 6-11). It indicates that although the current increases with increasing RF power it is tending to level off at high levels of RF power. It was noticed that there had been a dramatic increase in the amount of RF power reflected from what was measured in chapter six.
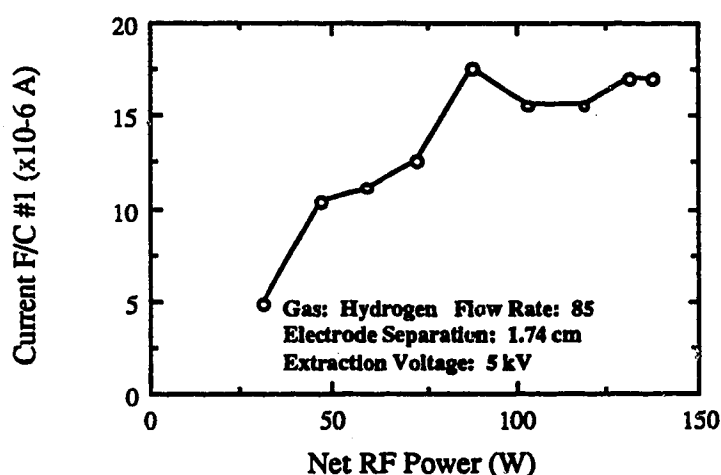
Fig. 7-5 This graph show the effect of the net RF power on the current at F/C #1.

7.2.2.2 Analysed Ion Current Data

The current measured after the analysing magnet at F/C #2 is used to determine the effect on the ion current of the source parameters. Data was only collected for argon and neon.

The data with neon was taken with hydrogen support gas being used so the first data examined will be the effect of support gas flow on neon currents (see fig. 7-6). This graph is very similar to the total current results with the level plateau followed by a drop off. In this case there is no peak before the drop off. The next two graphs were taken with a gas flow of 75.
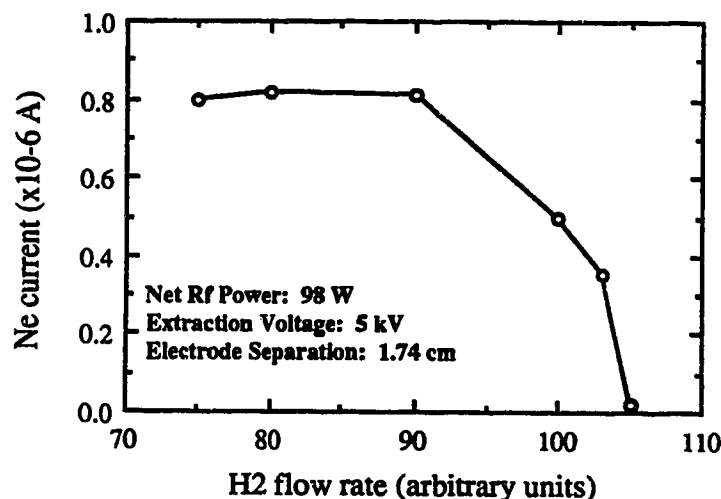
Fig. 7-6 This graph show the effect of the support gas flow rate on the neon current.

The data for the effect of the position of the Einzel Lens/Extraction Electrode (see fig. 7-7) shows a near linear increase in current with increasing gap size. This is similar to the results obtained in chapter 6 but lacks the pronounced peaks that were found there.
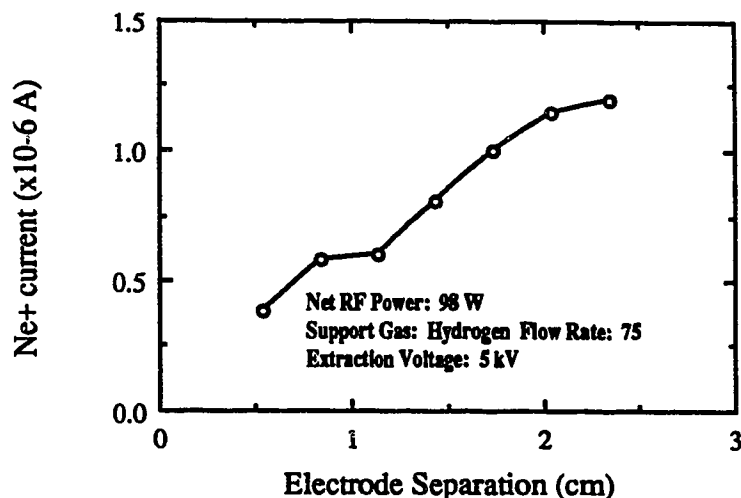
Fig. 7-7 This graph show the effect of the electrode separation on the neon current.

The graph for the effect of the RF power on the current (see fig. 7-8) also resembles the results from chapter six. There is an increase with increasing power but the high power saturation effect in still present.

The first two argon graphs that will be shown will show the results for the argon leak alone with no support gas. The first data to be examined will be the effect of the Einzel Lens/Extraction Electrode position on the observed current (see fig. 7-9) which shows a result similar to that for neon. There is in this case another difference between these results and the results seen in chapter 6. There is again no obvious peak but in addition there is an obvious hysteresis between the increasing and decreasing data.
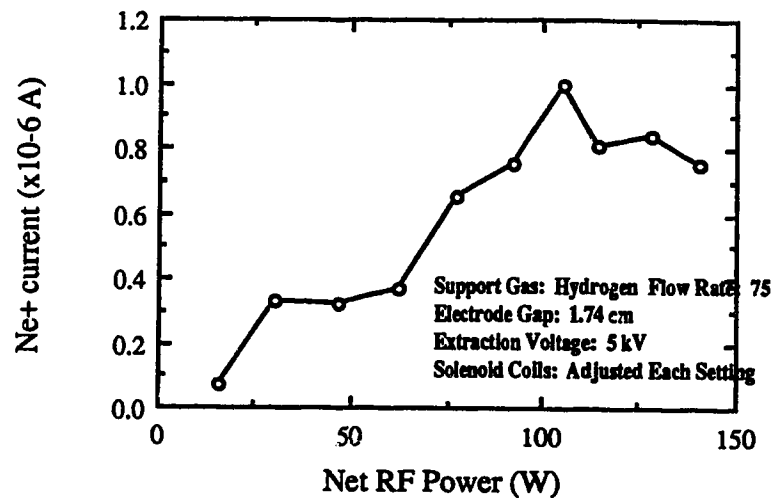
Fig. 7-8 The effect of the net RF power on the neon current.
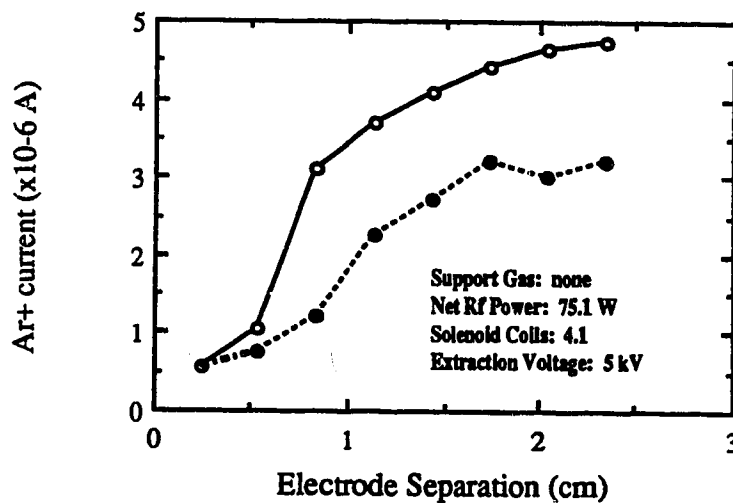
Fig. 7-9 The effect of the electrode separation on the Argon current. (o) indicates data collected while the gap was increased, (•) while the gap decreased.

In fig. 7-10 the data on the effect of the RF power in presented. Shown in this graph is the Ar current and the coil setting which gives that current versus the RF power. It shows a clear peak of the magnetic field at lower RF powers.
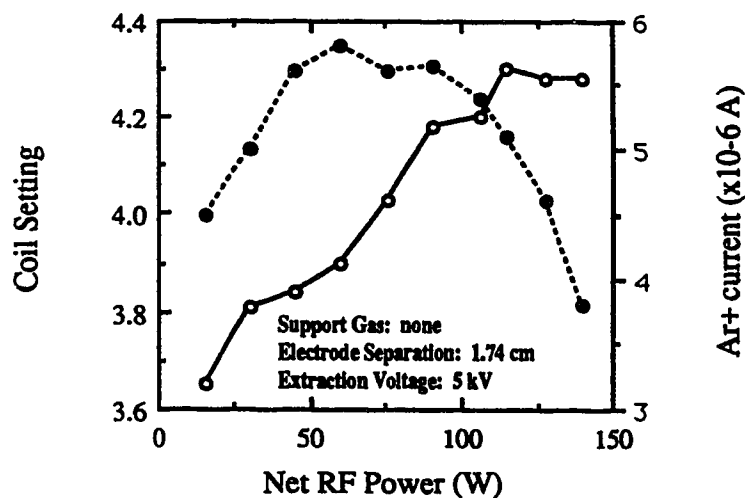
Fig. 7-10 The argon current(●) and the solenoid current (○) versus the net RF power.

The effect of helium carrier gas can be seen in fig. 7-11. The results shown here are similar again to those observed for the total current and neon except that in this case there is a peak before the drop off which is different from the neon results.
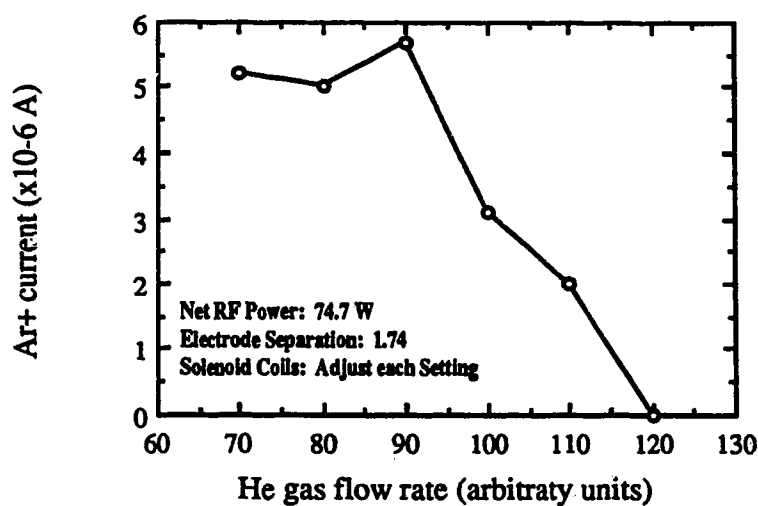
Fig. 7-11 The effect of the support gas flow rate on the Argon current.

After these tests had been completed and the emittance measurements completed (see section 7.3) the hole in the plasma electrode was increased from 1 mm to 2 mm in diameter. Tests on the total current, the specific ion species current and the emittance (see section 7.3) were carried out to evaluate the effect this change had on the source. Unfortunately, to meet the on-line installation schedule there was very little time to do these tests. The only data available for the ion currents is on argon as the source was loaded with gas from having the gas valve left open over night before the day scheduled for the neon run. Data for the emittance, however; was collected for both species.

For the argon leak with no carrier gas the effect of the magnetic field strength on both the total current and the amount of reflected RF power was measured (see fig. 7-12). There is an obvious effect here that indicates under normal operating conditions the magnetic field strength must be adjusted for the source parameters to ensure maximum output from the source.
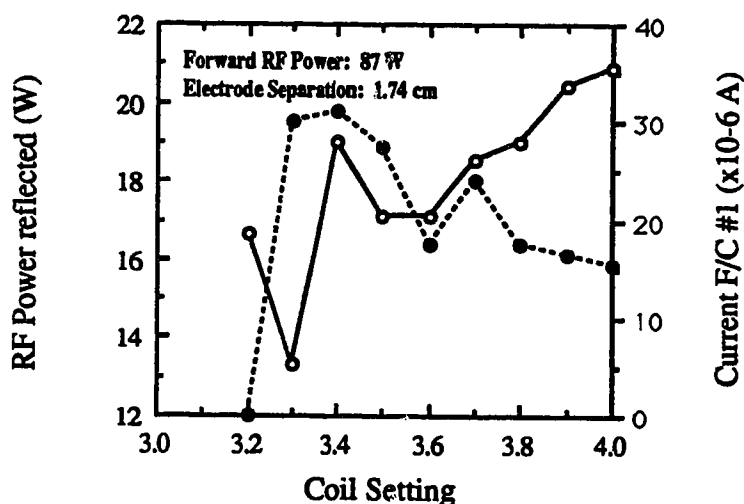
Fig. 7-12 The effect of the solenoid current on both the amount of RF power reflected(o) and the current at F/C #1(●).

The results for the effects of the EE position are shown in fig. 7-13 for both the argon

current and the total current at F/C #1. The total current exhibits a definite peak which does not follow the expected relationship from the Child-Langmuir Law. The argon current also shows a curve which is similar to the results obtained before.

Support Gas: none
Net RF Power: 76 W
Plasma Aperture: 2 mm Dia.

Electrode Separation (cm)
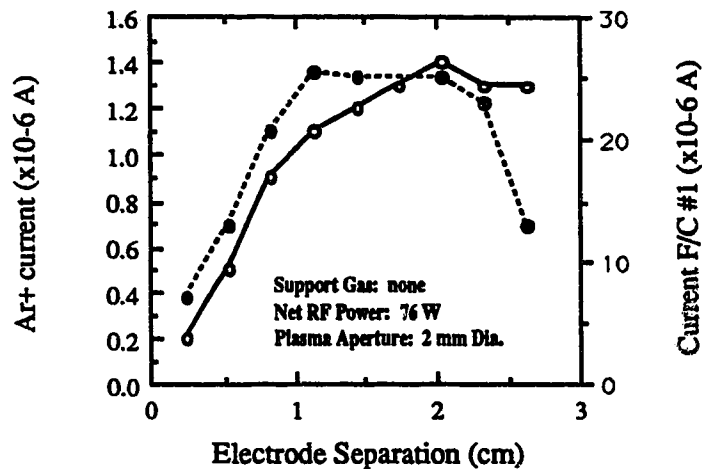
Fig. 7-13 The variation of both the Argon current (o) and the current at F/C #1 (●) with the electrode separation.

The data for the effect of the RF power on both the argon current and the total current is shown in fig. 7-14.

Electrode Separation: 1.74 cm
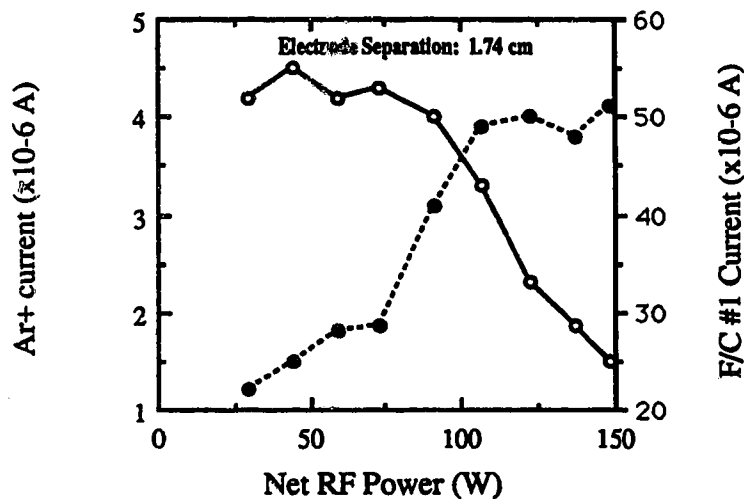
Net RF Power (W)

Fig. 7-14 The variation of the argon current (o) and the current at F/C #1 (●) with the net RF power for a 2 mm plasma electrode aperture.

The argon current differs from that obtained in fig. 7-10; here the current shows no peak but an initial plateau which drops off with increasing RF power. The total current results are very similar to the results obtained with hydrogen (see fig. 7-5) showing an increased current with increasing RF power.

The final data is for the effect of the hydrogen carrier gas flow on the measured argon current (see fig. 7-15). This graph shows the same results as previously found (fig. 7-6, 7-11). It shows a plateau and then a sharp drop off. In this case the result resembles the data for neon more than it does the argon data with Helium support gas. In all three cases the beginning of the curve is at approximately 90.
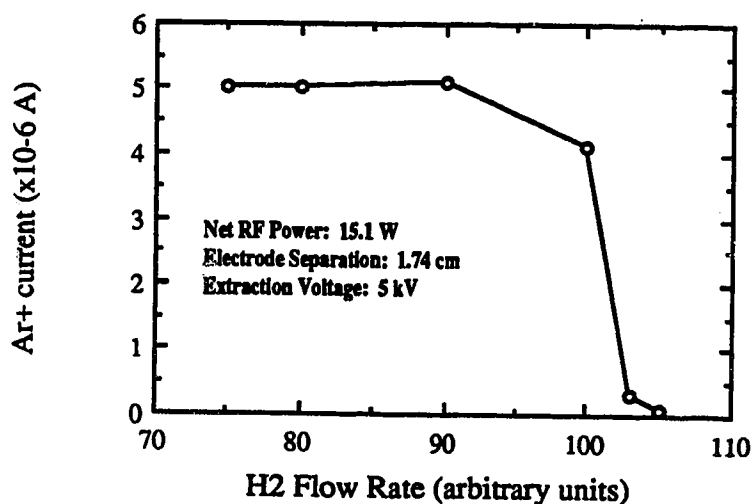
Fig. 7-15 This graph show the variation of the argon current with the support gas flow rate.

7.2.3 Efficiency Measurements

There was no concerted effort to remeasure the ionization efficiency of the source. Due to the increase in transmission caused by the changes to the source /beam line the

possible large errors involved in the standard method of determining ionization efficiency (see section 6.5) no longer apply. However, since the transmission does effect the result data collected during a mass scan is the best. Unfortunately such data is rare mainly due to time constraints: a mass scan was a time consuming operation.

The data collected can be found in table 7-1. The results shown here give ionization efficiencies more in line with the efficiencies given by the total current method rather than the transmission method when compared to the results of chapter 6.

Table 7-1: The data used to calculate the ionization efficiency, and the efficiencies as calculated by eq. 6-2 for neon and argon.

Species	Current	Number of Observations	Transmission	Ionization Efficiency
	(μA)		(%)	(%)
Ne	1.3±0.0	3	57-95	13±0
Ar	4.4±1.8	2	74-97	22±11

7.3 Emittance Measurements

This section will detail the measurements of the source emittance. The emittance of the source is important for this number tells how well the beam will be transmitted by the on-line system. There will be three parts to this section. The first will describe the emittance measuring probe. The second will cover the data collected for measurements made on the total ion beam. The final will deal with the measurements made on the argon and neon currents after the analysing magnet.

7.3.1 The Emittance Scanner

The scanner used in these measurements was supplied by the ISIS group and was based on a scanner developed in Los Alamos National Laboratory, USA. A drawing of

the scanner can be found in fig. 7-16. The scanner operated on the principle of electrostatic bending of a collimated beamlet. The beamlet was produced from the main ion beam by a slit. The current of the deflected beamlet was measured in a Faraday cup located behind a second slit. The scanner was stepped through the main ion beam and at each step was then scanned through a voltage range from -V to V where V is the voltage selected by the operator. Table 7-2 contains the physical parameters of the analysing part of the scanner. The current was read by a Keithley electrometer and written to computer by a DAC.

Table 7-2: Emittance Scanner parameters.

front slit width: 0.3 mm
bend plate separation: 2.8 mm
bend plate length: 38 mm
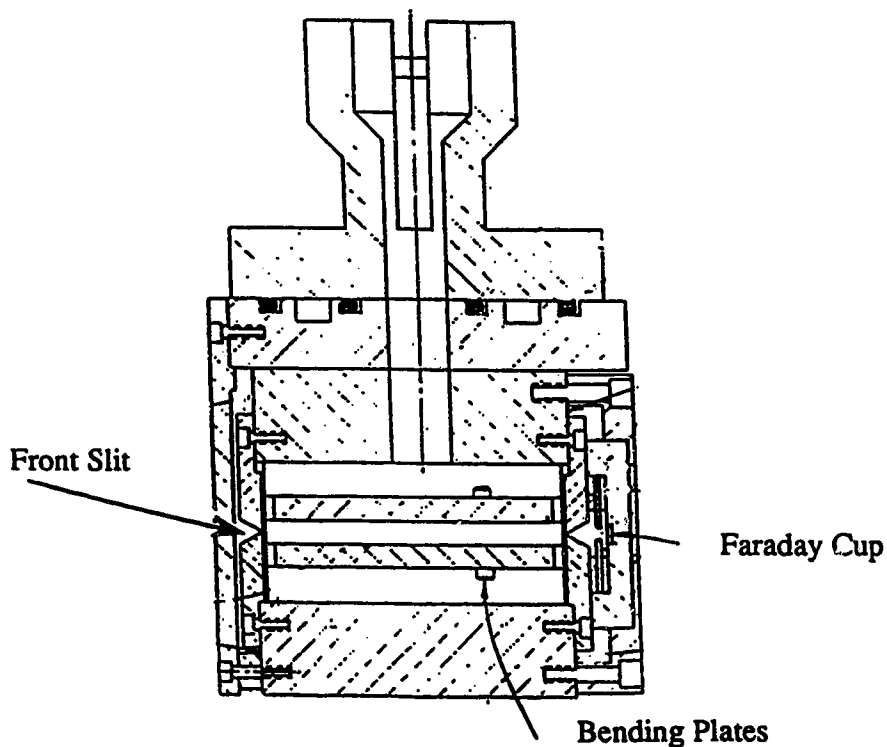
Fig. 7-16 This is a top view of the emittance scanner showing the slits and bend plate.

The scanner was controlled by a Starburst, while the acquired data was collected by the cyclotron Vax computer. The data was then copied to a file and analysed by a program written by Dr. R. Yuan and later modified by T. Pinnington. The program removed the noise contributions, and produced a plot of the emittance contours, a plot of emittance versus the percentage of the beam with that emittance and a beam profile.

There were some problems with using the scanner for this test. The primary one was that the scanner was intended to measure milliampere currents not microampere currents so to get a reasonably good signal to noise ratio the slit had to be opened up from 0.06 mm to 0.3 mm. This meant that the minimum step size was 0.33 mm to prevent double counting. This limited the accuracy of the plots especially when examining the specific ion beam currents after the analysing magnet as the beams were only a few mm across meaning that only 6 or 7 steps would be gathering data. Another problem was that even with the slit increase the signal to noise ratio was not good, especially for the analysed beam currents.

The emittance tests were done in two different positions. The first, which measured the total ion beam from the source, had the box containing the emittance scanner immediately after box one (see fig. 7-1); the analysing magnet was no longer part of the system and the ion beam merely impacted into the end wall of the box. In the second position the emittance scanner replaced F/C #2 although it was positioned closer to the exit of the magnetic vacuum chamber than F/C #2 was. This position allowed the emittance of a specific ion beam to be measured.

7.3.2 Emittance Tests on the Total Ion Beam Extracted from the Source

These initial runs reveal some information on the ion beam from the source. These tests extended over three days. The first day data on a helium plasma was collected. The

final two days were devoted to runs with a nitrogen plasma. For these runs the plasma was formed exclusively by the carrier gas being leaked in. In table 7-3 the quantities which were not varied or only varied slightly from run to run can be found.

Table 7-3: Source parameters which were not varied for the emittance tests.

Species	Gas Flow (arb. units)	Gap of EE (cm)	Net RF (W)	Coil Current (A)
He	90	1.74^1	76 ± 2	367
N2	90	1.74	109 ± 4	360 ± 4

[1]The 5 kV run was done at a gap of 1.44 cm.

The data collected in the runs are shown in table 7-4. An example of the emittance contour plot generated for each of the species are shown in figs. 7-17, and 7-18.

Table 7-4: The data collected during emittance runs on the total ion beams.

Gas	Extraction Voltage (kV)	Einzel Lens Voltage (-kV)	Emittance (π-mm-mrad) 90%	86%	63%	FWHM[1] (mm)
He	5	3.5	153	130	69	33
	10	3.5	135	121	63	24
	10	2.5	186	157	81	24
	10	0	205	171	86	23
N_2	5	3.5	100	90	51	17
	5	5	96	86	50	21
	10	2.5	146	129	72	23
	10	5	125	111	60	19
	10	7.5	102	90	49	16
	15	5	142	128	73	29
	20	5	137	122	67	22

[1]As measured from the profile provided by the program.
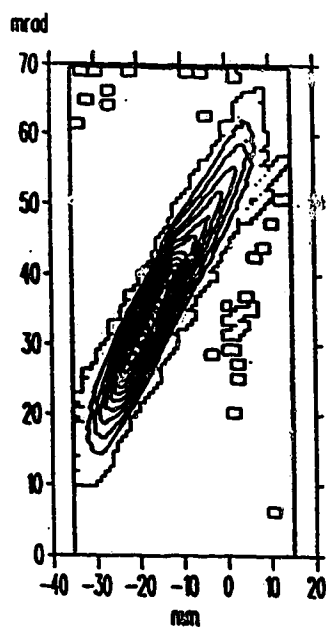
Fig. 7-17   The emittance contours for a beam extracted from a nitrogen plasma at 10 kV extraction energy, for an electrode separation of 1.74 cm, and an Einzel lens voltage of - 5 kV.
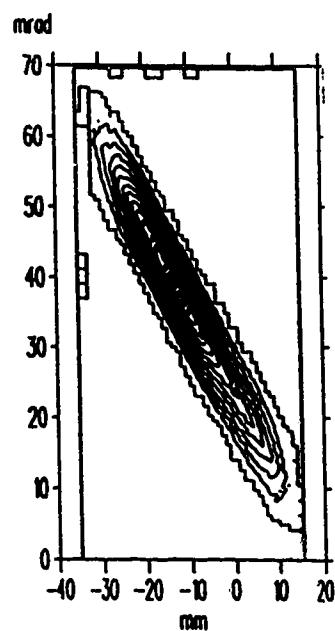
Fig. 7-18   Te emittance contours for a beam extracted from a helium plasma at 10 kV extraction energy, for an electrode separation of 1.74 cm, and an Einzel lens voltage of - 3.5 kV.

Since calculating the expected emittance is complicated the variation of the observed emittance with voltage and mass will be examined instead. A theoretical treatment of emittance can be found in section 2.3.6 but for this section some simple scaling rules (Sch 89) are sufficient. These rules give that basicaly the emittance ratio $R_{x,y}^{w,z}$ should scale as:

$$R_{x,y}^{w,z} = \frac{\varepsilon_x^w}{\varepsilon_y^z} = \sqrt{\frac{V_y}{V_x}} \cdot \sqrt{\frac{M_z}{M_w}} \cdot \left(\frac{FWHM_x}{FWHM_y}\right)^2 \qquad (7\text{-}1)$$

where: ε_a^b is the emittance for a voltage and b mass, V is the extraction voltage in kV, M is the atomic mass for the species, and $FWHM_a$ is the full width at half maximum of ion beam a.

In table 7-5 the experimental results are compared to the value obtained by eq. 7-1.

Table 7-5: A comparison of experimental data to eq. 7-1 to determine the effect of ion species and extraction voltage on the emittance.

Gas	Ratio	Observed Emittance Ratio		Result from
		90%	63%	eq. 7-1
He	$R_{10,5}$	0.88	0.98	0.37
N2	$R_{10,5}$	1.30	1.20	0.58
	$R_{15,5}$	1.48	1.46	1.10
	$R_{20,5}$	1.42	1.34	0.51
	$R_{15,10}$	1.14	1.22	1.90
	$R_{20,10}$	1.10	1.12	0.94
	$R_{20,15}$	0.96	0.92	0.50
---	$R_{5,5}^{He,N_2}$	1.59	1.38	1.87
---	$R_{10,10}^{He,N_2}$	1.08	1.13	1.87

There is obviously poor agreement between the experimental data and the theory. There are a number of explanations for this. The primary one is that this was not a mono ionic-beam. The beam consisted of a large number of species and charge states hence the deflection of the bending plates will not be uniform. Since the program assumed it was looking at hydrogen, only the results are bound to be somewhat in error. Another problem was that it was nearly impossible to optimize the source with respect to anything except the current at F/C #1. Therefore as many parameters as possible were left the same as the extraction voltage was changed. Although this allows for easy comparison between extraction voltages it may also mean that the best emittance could be found elsewhere which would throw the ratio off. Also since the signal to noise ratio was not always very high the program may be including noise in the emittance calculations which would result in an apparent emittance increase.

There is also a problem in that the emittance values themselves are very large. Data from the emittance of the LBL source (Cla 87) and the Pre-ISIS source (Kra 86) show that the emittance is considerably higher than it should be even after adjusting for the differences in plasma electrode hole diameter. This is harder to justify but it is very likely that the same arguments used before would also serve here.

There is also the equally puzzling effect that the Einzel lens effects the source emittance. It is reasonable to assume that the lens should effect the slope of the emittance plot or even introduce aberrations but it should not effect the size of the emittance itself. An explanation for this might be that the scanner was located before the focal point of the lens and what is being seen is the lens operating.

7.3.3 Emittance Tests on Analysed Ion Beams

This section will present the data gathered on analysed ion beams of argon and neon.

The first concern was that instead of determining the emittance of the ion beam only the acceptance of the analysing magnet would be measured. However, if the FWHM of the total ion beam is examined (see table 7-4) it becomes apparent that most of the beam is smaller than the 38 mm aperture of the magnet which means that the emittance is indeed being measured.

The results for argon will be described first. In fig. 7-19 the effect of the Einzel lens on the emittance can be seen. This graph shows a clear decline with increasing Einzel lens voltage. This result was unexpected. The increasing voltage should have merely rotated the emittance plot clockwise or counter-clockwise depending on whether the beam was caused to converge or diverge. Also, visible in the emittance contour plots (see fig. 7-20 for a good example) were very clear lens aberration effects.
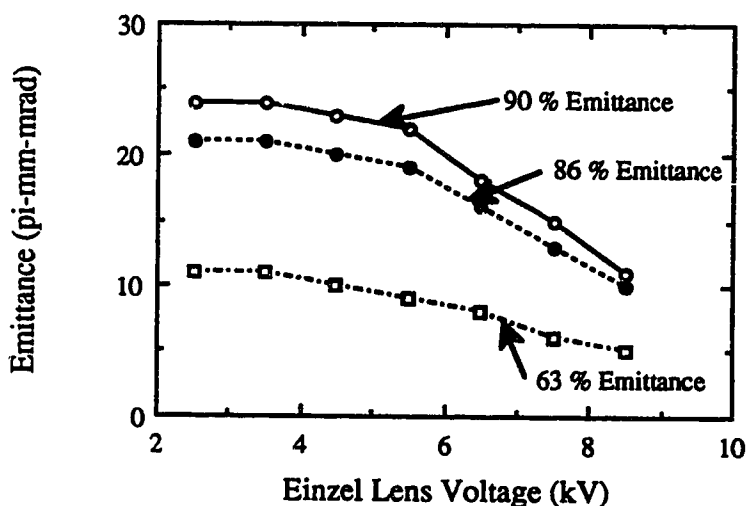
Fig. 7-19 This graph shows the emittance for Argon with an electrode separation of 1.7 cm as a function of einzel lens voltage.

mrad
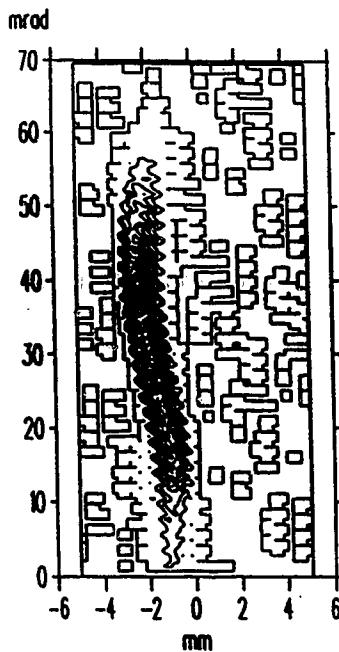
Fig. 7-20 The emittance contour plot for an Argon ion beam at 5 kV extraction voltage, electrode separation of 1.74 cm and Einzel lens voltage of -5 kV.

For the effect of the position of the extraction electrode on the emittance see fig. 7-21. There are two groups of data here. The first was collected with a 1 mm diameter aperture in the plasma electrode while the second was collected after the diameter was opened up to 2 mm. The data for the 1 mm diameter aperture is lower than that for the 2 mm diameter which is what would be expected but not by the factor of four that would be expected from theory. In the case of the 2 mm aperture the emittance decreased with increasing gap this was not the case with the 1 mm aperture.
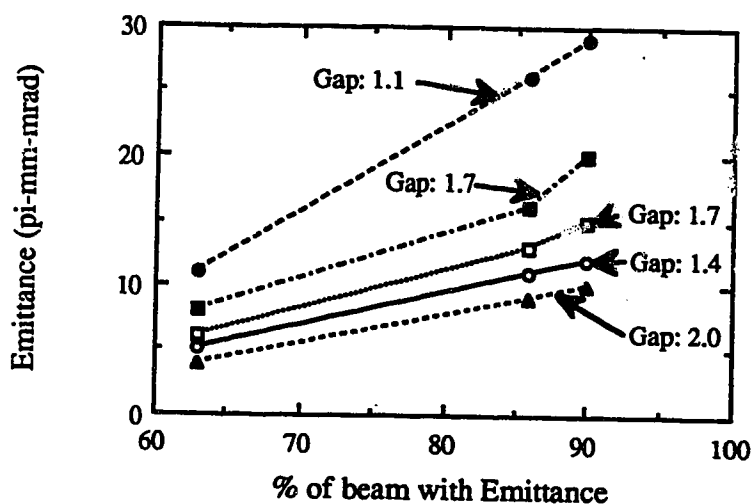
Fig. 7-21 The effect of both the electrode separation (gap) and the plasma electrode aperture size on the emittance of the Argon beam. The solid symbols are for a 2 mm diameter plasma aperture, the open symbols for a 1 mm.

The effect of the RF power on the emittance was also measured. The data can be seen in fig. 7-22. This graph also shows the effect of the support gas as the data for the 1 mm aperture was taken with hydrogen support gas being added to the plasma. The support gas seems to both reduce the emittance and minimize the effect of different RF power levels. For situations with no support gas it seems that increasing the RF power increases the emittance which seems reasonable as increasing RF power implies a more energetic plasma which would effect the ion temperature and hence the emittance.
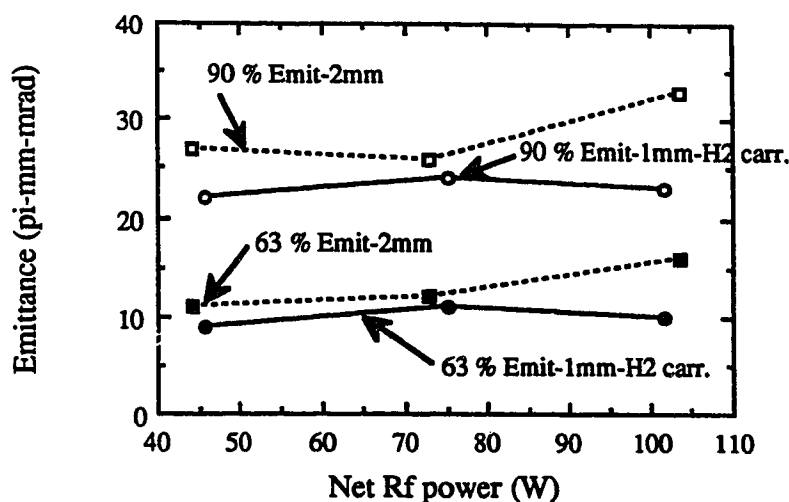
Fig. 7-22 The emittance for Argon with an electrode separation of 1.7 cm as a function of net RF power. The size of the plasma electrode aperture and the carrier gas used if any is also shown.

The data for neon is less extensive then that for argon mainly because the neon beam was much less intense which meant that the emittance profiles were much more effected by scanner considerations mentioned in section 7.3.1. In fig. 7-23 the effect of the gap size on the emittance is shown. This graph shows even less of an effect for the aperture diameter than in the argon case. The emittance is also larger than in the case of argon which is also what is expected. Note that the data for a 1 mm aperture and a 1.4 cm gap coincide exactly with that for a 2 mm aperture and a 1.7 cm gap.
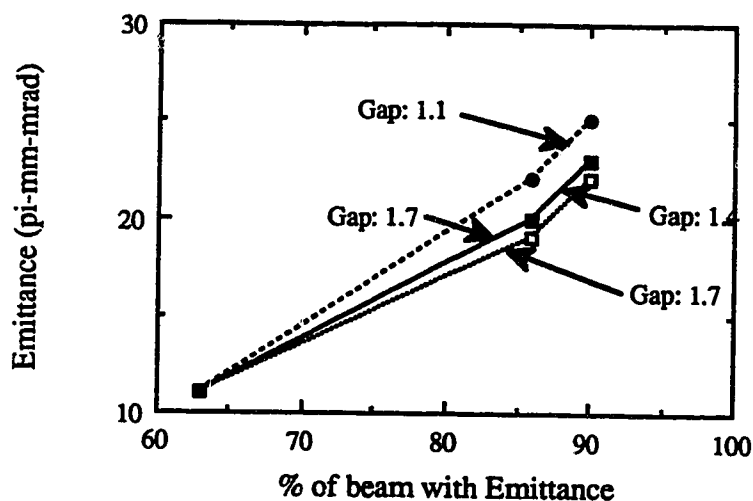
Fig. 7-23 The effect of both the electrode separation (gap) and the plasma electrode aperture size on the emittance of the Neon beam. The solid symbols are for a 2 mm diameter plasma aperture, the open symbols for a 1 mm.

For neon it was also possible to increase the extraction voltage to 10 kV and still be able to bend the beam in the analysing magnet. The data for these runs and for 5 kV comparison runs is shown in table 7-6. The results do not show reasonable agreement between the experimental and theoretical (determined by eq. 7-1) ratios.

Table 7-6 A comparison between the emittance determined for neon at 5 and 10 kV extraction voltage for the following source parameters: plasma aperture 2 mm, and 1.7 cm plasma-puller electrode gap.

Extraction Voltage (kV)	Einzel Lens Voltage (kV)	FWHM (mm)	Emittance (π-mm-mrad)		$\varepsilon_{10}/\varepsilon_5$		R_{7-1}
			90%	63%	90%	63%	
5	2.5	1.8	28	15	0.78	0.60	0.26
10	2.5	1.1	22	9			
5	5	1.3	23	11	0.83	0.73	0.34

Table 7-6: Continued.

Extraction Voltage (kV)	Einzel Lens Voltage (kV)	FWHM (mm)	Emittance (π-mm-mrad) 90%	63%	ε10/ε5 90%	63%	R7-1
10	5	0.9	19	8			
5	7.5	1.6	17	8	1.12	1.00	0.14
10	7.5	0.7	19	8			

There was sufficient data collected for both neon and argon to do a good comparison between the results to see if they follow the mass dependance given in eq. 7-1. In table 7-7 the comparisons are tabulated. In general the agreement is poor but not as bad as found in tables 7-5, 7-6.

Table 7-7: A comparison between the argon and neon emittance data comparing the experimental ratio to that of eq. 7-1.

Species	Extraction Aperture (mm)	Separation (cm)	Einzel Lens Voltage (kV)	FWHM (mm)	Emittance (π-mm-mrad) 90%	63%	εAr/εNe (exp) 90%	63%	Ratio from eq. 7-1
Ar	1	2.0	7.5	1.2	10	4	0.66	0.66	0.65
Ne	1	2.0	7.5	1.25	15	6			
Ar	1	1.4	7.5	1.1	12	5	0.63	0.62	0.86
Ne	1	1.4	7.5	1.0	19	8			
Ar	2	1.7	7.5	1.3	20	8	1.18	1.0	0.47
Ne	2	1.7	7.5	1.6	17	8			
Ar	2	1.7	5.0	1.4	27	12	1.17	1.09	0.82
Ne	2	1.7	5.0	1.3	23	11			
Ar	2	1.1	5.0	1.2	33	12	1.32	1.09	0.71
Ne	2	1.1	5.0	1.2	25	11			

In summary, it has been found that the emittance results do not fit the accepted theories very well. Whether the fault lies with the theory or the source is hard to determine. It was not easy to optimize the source for a scan since there was no faraday cup after the scanner to determine what effect the change in source parameters had on the ion beam. There could also be problems with the theory. As little is known about the actual plasma conditions and the exact effect of the magnetic field in the extraction region it is hard to predict what effects should be seen and what it means if they are not.

7.4 The On-line Facility

The final section of the chapter will deal in brief with the on-line system: the TISOL-ECR. This will be divided into two subsections. The first will outline the the the on-line facility itself while the second will describe the final source modifications.

7.4.1 The TISOL-ECR Facility

There were no changes made to the beamline above the bending magnet which is as it was described in section 1.5. The only changes were made to the ion beamline in the containment room.

7.4.1.1 The Ion Beam Line

The TISOL-ECR is basically a modification of the standard TISOL operating condition where the TIS (Target Ion Source) box is removed and the ECRIS and a new target box are installed. However, since the ECRIS and target box are longer than the TIS box, the old focusing quadrupoles were replaced by new quadrupoles. An additional steering (both in X and Y) magnet was added just before the "Rocky" 90° analysing magnet. The new ion beamline can be seen in fig. 7-24.
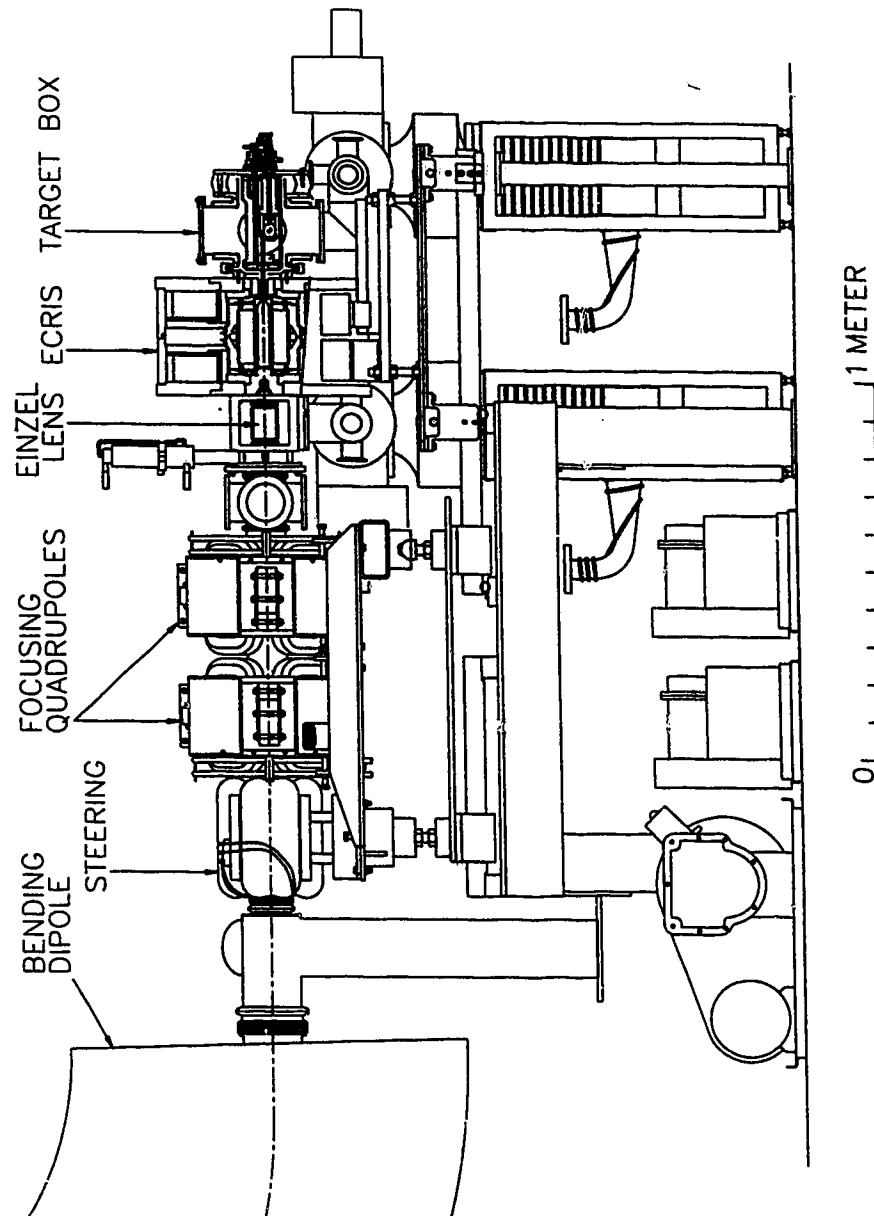
Fig. 7-24 The ion beamline as viewed from BL-4A.

The whole ECRIS/Target assembly (see fig. 7-25) is sealed by a gate valve so it can be removed as a complete unit to contain any radioactive contamination. The target box

also has windows in it so that it is also isolated from the proton beamline 4-B. The vacuum is provided by two 6" diffusion pumps. One pump is mounted to pump on the target box and the other to pump on the extraction region and the inner quartz tube.
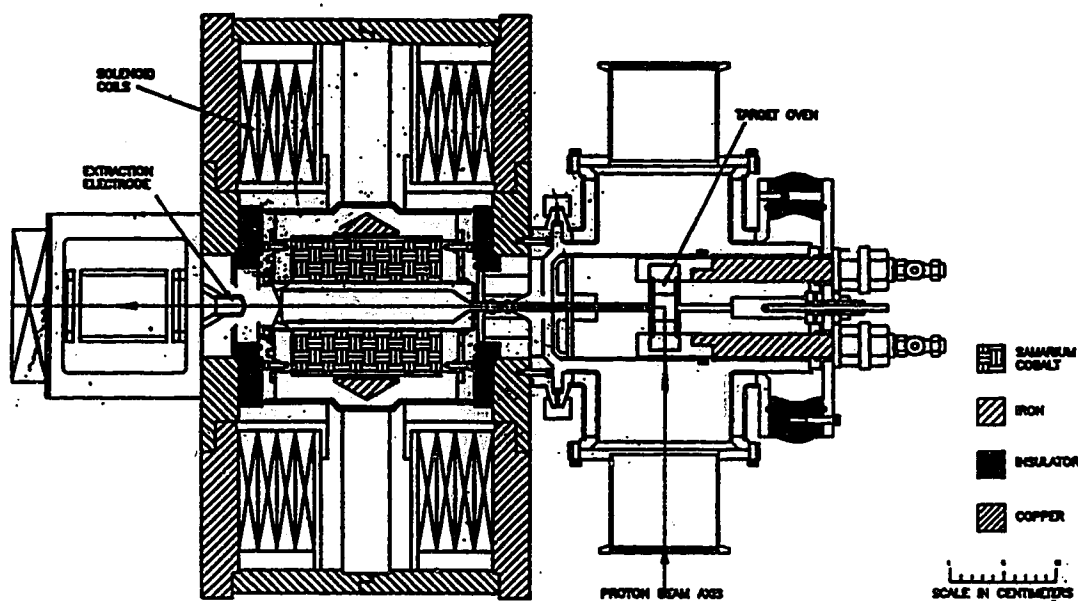
Fig. 7-25 This diagram shows a top view of the ECRIS/TIS assembly.

7.4.1.2 Other Changes to the Existing TISOL Facility

The microwave generator and amplifier used in the off-line work are still being used on-line with the main difference between that the on-line location of the microwave amplifier is above the shielding blocks some 15 m from the source. The other difference is that the wave guide used is for 6.4 GHz microwaves so that three horns are necessary; one to initially couple to the 10 GHz waveguide just after the crossguide coupler and one before and one after the choke stack. Also, there are now four bends in the waveguide path. M. McDonald measured an ~0.4 dB (~10%) loss in power to go through the bends.

The TISOL control system had to be modified to handle the different devices of the

ECRIS/Target assembly. A new computer program was created and the facility was rewired to accommodate the changes.

The gas handling system is virtually unchanged from the off-line system, in fact the same manifold is used except that above each calibrated leak is a solenoid valve for remote operation. There is only one carrier gas bottle and again its flow is controlled by a needle valve (different from the one used off-line). The source can be run in four different modes: on no gas input, on only the carrier gas, on only a leak gas, or on a mixture of the carrier and leak gases.

7.4.1.3 The Target Box

The Target box used by the ECRIS consisted of two major components: the target/oven assembly, and a double-walled water-cooled T-piece which provided mounting for the target/oven assembly, the beamline, and the vacuum connection to the diffusion pump.

The target/oven assembly contained all the connections for the high voltage, the oven heating, the water cooling for the target heat shield and oven electrodes, and for the carrier gas. The target oven itself was held in the proton beam by the electrodes but was a removable assembly to allow for easy change of the target crucible. Initially, it was intended to use a graphite oven but unforeseen mechanical stresses resulted in the breakage of the oven on assembly so instead a 0.002" thick tantalum foil oven was used. This oven worked much better than expected producing as high a temperature as graphite but with much less current. This change had another unexpected benefit: the cost of the oven was now so low it could be considered a disposable item after it was too badly contaminated.

The carrier gas line was connected to the oven via a tantalum chimney and then on to

the ECRIS by a tantalum transfer tube which coupled to the inner quartz tube at the new Delrin insulator. The entire target assembly was surrounded by a copper heat shield and the end of the heat shield facing the ECRIS was water cooled.

This design had benefited from the accumulated expertise of the TISOL group. It was simple to change either the oven or the target crucible even if one had to work in the glove box. The whole assembly was also easy to assemble with a minimum of screws. Installation of the assembly into the T-piece was not difficult even for only one person and required no complicated alignment procedure after it was initially installed.

7.4.2 The Modifications Made to the ECRIS

There were only two final modifications made to the ECRIS. The first was a change in the extraction electrode/ einzel lens assembly. The second was a modification of the upstream vacuum area.

The extraction electrode/einzel lens assembly was redesigned for remote operation. The major changes were as follows. A modification to the extraction electrode holder was made to increase the pumping speed in the extraction region. A much better mounting assembly was designed which allowed for easy adjustment in the X and Y directions of the extraction electrode to allow for accurate alignment with the source. Also included in the changes was the addition of a computer-controlled electric motor and a system of gears to move the extraction electrode/ einzel lens assembly along the Z axis. Finally, a stainless steel plasma electrode with a 1 mm aperture replaced the copper one used in the off-line tests.

The modifications to the upstream vacuum area consisted of remaking the center iron plug of the upstream field clamp to accommodate both the target box mount and a new position for the hexapole air cooling connections. As well the stem of the inner quartz

tube was shortened . Finally, a new Delrin insulating plug was fashioned (although shown in fig. 7-25, it is NOT shown crosshatched) which had two jobs. The first is to support the inner quartz tube and hold it in place against the alignment insert and to serve as a coupling between the transfer tube and the inner quartz tube. Its second function was to shield the field clamp completely from the high voltage of the RF cavity and thus prevent arcing. The plug was pierced to provide pumping between the two quartz tubes for thermal insulation.

Chapter 8 Conclusion

This project has accomplished the goals that it had set out. An ECRIS has been designed, built, and tested in an off-line mode. The ionization efficiencies for argon and neon have been measured but absolute values differ depending on the method used to calculate them (see sections 6.5 and 7.2.3). The ionization efficiency appeared to have a form of linear dependance on species mass, as was seen in the PSI source.

It has been determined that the amount of support gas leaked into the source has a far more important effect on source performance than the type of gas used. Helium seems to be the best candidate for an on-line support gas (see section 6.6) mainly due to the fact that it is relatively chemically inert especially as compared to hydrogen or nitrogen.

The effects of the RF power are puzzling showing for argon a marked preference for lower RF power levels, while it seems neon would prefer somewhat more power than is currently available. It seems reasonable to suspect that the same is true for nitrogen due to the strength of its triple molecular bond. There is also the saturation effect which has been observed in all operating sources although it occurs at much higher power for the Karlsruhe source (Bec 85) than any of the others.

The effect of the puller electrode separation yields results which indicate that a gap in excess of 1 cm provides the largest analysed ion current. It is quite likely that at smaller separations too much of the ion beam is striking the puller electrode. It has also been observed that extraction geometry is critical to achieving a good quality beam. Measurements of the beam emittance indicate that the source has a good emittance although the results do not fit the accepted scalings well.

The magnetic field of the solenoid coils was determined to be of primary importance to source operation and adjustment of any source parameter should be followed by

147

readjustment of the magnetic field to optimize source performance.

In fact, the stated goals of the project were exceeded as an initial on-line test was carried out (for the results see appendix A). This test, considering the running conditions, was an outstanding success. The results, which were by no means optimal, compare well with the ISOLDE results. The source has now begun its commissioning runs on TISOL.

References

[Ade 84] Adelberger, E. G., *et. al.*, Phys. Rev. C **30**, 456 (1984).

[Ant 87] Antaya, T.M., Z.Q. Xie, *International Workshop on ECR Ion Sources and their Applications*, ed. J. Parker, East Lansing, 420 (1987).

[Ant 89] Antaya, T.M., Journal de Physique **50**, C1-707 (1989).

[Bec 85] Bechtold, V., S.A. Shiekh, *Proceedings of the Accelerated Radioactive Beams Workshop*, eds. L. Buchmann, and J.M.D'Auria, Parksville, 110 (1985).

[Bec 86] Bechtold, V., H. Dohrmann, and S.A. Sheikh, *7th Workshop on ECR Ion Sources*, ed. H. Beusher, Julich, 110 (1986).

[Buc 86] Buchmann, L., *et. al.,7th Workshop on ECR Ion Sources*, ed. H. Beusher, Julich, 177 (1986).

[Cla 87] Clark, D.J., *International Workshop on ECR Ion Sources and their Applications*, ed. J. Parker, East Lansing, 433 (1987).

[Cra 84] *Proceedings of the TRIUMF ISOL Workshop*, eds. J., Crawford, and J.M. D'Auria, Mt. Gabriel, (1984) TRIUMF Report TRI-84-1.

[DAu 89] D'Auria, J.M., Private Communications, 1989.

[Del 88] *The "Radioactive Ion Beam" Project at Louvain-la-Neuve*, eds. Th. Delbar, *et. al.*, (1988) Belgian Inter-university Report RIB-1988-01.

[Gel 87] Geller, R., *et.al.,International Workshop on ECR Ion Sources and their Applications*, ed. J. Parker, East Lansing, 1 (1987).

[Gel 89a] Geller, R., *et. al.*, Journal de Physique **50**, C1-673 (1989).

[Gel 89b] Geller, R., *et. al.*, Journal de Physique **50**, C1-887 (1989).

[Gim 89] Gimond, J.L., *et. al.*, Journal de Physique **50**, C1-791 (1989).

[Has 89]   Haseroth, H., Journal de Physique 50, C1-659 (1989).

[Hof 88]   Hofer, M., Private Communications, 1988.

[Hof 89]   Hofer, M., Private Communications, 1989.

[Jon 84]   Jongen, Y., *Proceedings of the 10th Int. Conf. on Cyclotrons and their Applications*, East Lansing, 322 (1984).

[Kra 86]   Krauss-Vogt, W.,*7th Workshop on ECR Ion Sources*, ed. H. Beusher, Julich, 274 (1986).

[Lib 89]   Liberman, B. *et. al.*, Journal de Physique 50, C1-739 (1989).

[Lyn 86]   Lyneis, C.M.,*Proceedings of the IEEE Particle Accelerator Conference*, Washington, 254 (1987).

[Lyn 89]   Lyneis, C.M., Journal de Physique 50, C1-689 (1989).

[Mac 86]   Mack, M., *et. al.*, *7th Workshop on ECR Ion Sources*, ed. H. Beusher, Julich, 152 (1986).

[Mat 86]   Mattman, T., TRIUMF Internal Report, 1986.

[Par 86]   Pardo, R., and E. Minehara, *7th Workshop on ECR Ion Sources*, ed. H. Reusher, Julich, 236 (1986).

[Pet 87]   Petty, C.C., *et. al.*, *International Workshop on ECR Ion Sources and their Applications*, ed. J. Parker, East Lansing, 151 (1987).

[Pet 89]   Petty, C.C., *et. al.*, Journal de Physique 50, C1-783 (1989).

[Rav 84]   Ravn, H., *Proceedings of the Accelerated Radioactive Beams Workshop*, eds. L. Buchmann, and J.M.D'Auria, Parksville, 257 (1985).

[Rav 88]   Ravn, H., Private Communications, 1988.

[Sch 89] Schmor, P.W., Private Communications, 1989.

[TIS 85] *The TRIUMF-ISOL Proposal*, 1985, TRIUMF Report TRI-85-1.

[Van 89] Van Duppen, P., Private Communications, 1989.

Appendix A Initial On-Line Test Results

A.1 Operating Conditions

The source/ion beamline conditions for the July 18, 1989 run were far from ideal. The diffusion pump in the extraction area had developed a water leak and had to be shut off so the vacuum was in the low 10^{-5} Torr regime. As well due to arcing in the extraction region the maximum source voltage was limited to 12 kV for stable operation. There was a vacuum leak on the argon leak bottle connection to the manifold so that the bottle could not be used as a mass marker.

The production target consisted of a number of titanium foils with a combined target thickness of 5.45 gcm^{-2}. The initial proton beam current was 65 nA but as the test progressed it was increased to a maximum of 312 nA (see table A-1). The Target performed well. The heat shielding protected the rest of the source from the high temperature of the oven.

Another problem encountered during this run was particle identification since all previous TISOL runs had been done with 20 kV extraction voltage. This problem was further compounded since a number of ions came out as ionized hydrogen compounds (for example, HCl^+). A firm identification scale was fixed, however; by the observation of $^{43}Ar^{2+}$ with its distinctive m/q value of 21.5.

Transmission through the ion beamline and the electrostatic beamline was excellent.

A.2 Source Performance

Helium support gas was available to be used during this run but the absolute flow could not be determined since the flow controller is uncalibrated. The calibrated neon

leak was used to generate the initial plasma. There was no effort made to record source values since they changed with each species, however; some general comments on source performance can be made. The solenoid current (hence the magnetic field) was considerably lower than in the off-line tests. This is understandable when the pressure in the source is considered. Due to the bad vacuum conditions the pressure would be in the regime where charge exchange is a *very* serious consideration. So to allow for any ion extraction at all the ECR region (and the plasma boundary) would have to be very close to the extraction hole. This was the case with the lower field strength. If the field was too strong the ECR region moved away from the extraction area and any ions produced would be neutralized by charge exchange before they could be extracted.

Due to the arcing problems the puller electrode was kept at a substantial distance from the plasma electrode (15-20 mm).

The reflected RF power was also quite high, although this might be due to a miscalibration of the power meter which occurred during transport from the CRM. If the amount of RF power reflected did actually increase over the off-line test, then this can be explained by an increased plasma density resulting in less RF absorption by the plasma.

The current extracted from the source was the biggest surprise. The current observed at faraday cup 1 (see fig. 1-2) (ie. the total extracted ion current) was > 100 μA yielding a minimum current density of 40 mAcm^{-2}. As well, it was observed that the current was space charge limited since it varied with the extraction voltage. These two conditions are both dramatic changes from what was observed in chapter 7. This result is *very* puzzling and no reasonable explanation seems to fit both the on and off-line results.

A.3 Results

Faraday cup 4 (see fig. 1-2) was a foil used as a collector which was viewed by a γ

detector (although later a β detector was added). The data from the γ detector was collected and analysed by the PC based program GAMCAL. The run results, compared with both theoretical calculations, and ISOLDE yields (Rav 85) are shown in table A-1. Note that it is impossible to compare the ISOLDE results to the theoretical yields since the targets are different. The expected production rate at the target, I_γ^A, is given by:

$$I_\gamma^A = I_p\, N\, \sigma_A \qquad\qquad (A\text{-}1)$$

where: I_p is the proton current in protons/s/μA
N is the target thickness in atoms/cm^2
σ_A is the production cross section for isotope A in cm^2.

Table A-1: A comparison of the results observed on July 18, 1989 to both theoretical predictions and published ISOLDE results.

Isotope	$\tau_{1/2}$	TRIUMF Yield[3] (10^5 atoms/s/μA)	ISOLDE Yield (10^5 atoms/s/μA)	σ (mb)	I_p (nA)	Theoretical Yield[4] (10^5 atoms/s/μA)
^{23}Ne	37.2s	1.1	4.1	0.198	300	8.48×10^2
^{24}Ne	3.4m	2.7	2.0	0.064	300	2.74×10^2
^{34}Cl	32m	0.96[1]/0.27	0.32	0.120	190	5.14×10^2
^{35}Ar	1.8s	0.72	7.2	7.2×10^{-3}	190	3.08×10^1
^{38}Cl	37.2m	0.8	26	0.367	312	1.57×10^3
^{41}Ar	1.8h	45.0	300	6.39	132	2.74×10^4
^{43}Ar	5.4m	0.12[2]	13	26	133	1.11×10^5
^{44}Ar	11.9m	0.14	1.9	16.6	190	7.11×10^4

[1]as HCl$^+$
[2]as Ar^{2+}
[3]yield at the collector (F/C 4) above the shielding blocks (DAu 89)
[4]yield at the production target as calculated by eq. A-1